

XXXXX

Abstract

Contents

List of Figures	viii
List of Tables	x
1 Introduction	1
2 The Physics of Accretion	3
2.1 High-Mass and Low-Mass X-Ray Binaries	3
2.1.1 Black Hole LMXBs	3
2.1.2 Neutron Star LMXBs	3
2.2 The Shakura-Sunyaev Disk Model	3
2.3 GRS 1915+105 and IGR J17091-3624	3
2.3.1 A History of Models of GRS 1915-like Variability	3
2.4 Type II Burst Sources	7
3 Tools & Methods	9
3.1 Instrumentation	9
3.1.1 The <i>Rossi X-Ray Timing Experiment</i>	9
3.1.2 The <i>Neil Gehrels Swift Observatory</i>	10
3.1.3 <i>XMM-Newton</i>	10
3.1.4 <i>Chandra</i>	10
3.1.5 <i>Suzaku</i>	10
3.1.6 <i>NuStar</i>	10
3.1.7 <i>INTEGRAL</i>	10
3.2 Raw Data Extraction	10
3.3 Lightcurve Analysis	10
3.3.1 Flare-Finding Algorithm	10
3.4 Timing Analysis	12
3.5 Spectral Analysis	12
4 Variability in IGR J17091-3624: Classification	15
4.1 Introduction	15
4.2 Data and Data Analysis	19

4.2.1	<i>RXTE</i>	19
4.2.2	<i>Swift</i>	22
4.2.3	<i>INTEGRAL</i>	22
4.2.4	<i>XMM-Newton</i>	23
4.2.5	<i>Chandra</i>	23
4.2.6	<i>Suzaku</i>	24
4.3	Results	25
4.3.1	Outburst Evolution	25
4.3.2	<i>RXTE</i>	26
4.3.3	<i>Swift</i>	50
4.3.4	<i>INTEGRAL</i>	50
4.3.5	<i>Chandra</i>	52
4.3.6	<i>XMM-Newton</i>	53
4.3.7	<i>Suzaku</i>	53
4.4	Discussion	55
4.4.1	Variability Classes: IGR J17091 vs. GRS 1915	57
4.4.2	General Comparison with GRS 1915+105	62
4.4.3	Comparison with the Rapid Burster	63
4.4.4	Comparison with Altamirano <i>et al.</i> 2011	64
4.4.5	New Constraints on Accretion Rate, Mass & Distance	65
4.4.6	Implications for Models of ‘Heartbeat’ Variability	67
4.5	Conclusions	67
5	Burst Evolution in GRO J1744-28	69
6	GRO J1744-28: the Transitional Pulsar Link	71
6.1	Introduction	71
6.2	GRO J1744-28: The Bursting Pulsar	73
6.3	Comparison	74
6.4	Discussion	78
7	Conclusions	81
A	Model-Independent Classification of each Observation of IGR J17091-3624	108

List of Figures

- 3.1 From top-left: (i) An untouched data-set. (ii) The dataset with all $y < T_L$ removed. (iii) The dataset with all contiguous nonzero regions with $\max(y) < T_H$ removed. (iv) The peak x-values x_m . (v) The restored dataset with the peak x-values x_m highlighted. (vi) The boundaries between adjacent peaks. 11
- 3.2 The Heidke Skill score of a Class IV observation of IGR J17091-3624 for a selection of different values P_L and P_H 13
- 4.1 A schematic diagram illustrating the the process described by Neilsen et al. (2011) to describe the ρ variability class in GRS 1915+105. 1) The X-ray emission from the system originates from both the accretion disc truncated at an inner radius r_{in} (grey) and a cloud of non-thermal electrons (white ellipse). At some time t , an overdensity in the accretion disc (formed by the Lightman-Eardley Instability) propagates inwards towards r_{in} . 2) As the inner disc heats up, r_{in} begins to slowly increase due to an increase in photon pressure. This destabilises the disc. 3) At some critical density, the disc becomes too unstable and collapses inwards, greatly decreasing r_{in} and raising the inner disc temperature. 4) The sudden increase in emission exceeds the local Eddington limit at r_{in} , ejecting matter from the inner accretion disc in the form of extreme winds. 5) Having been excited by matter in the winds passing through it, the non-thermal electron cloud emits a hard Brehmsstrahlung ‘pulse’. . 18

4.2	<i>RXTE</i> (Panel a), <i>Swift/XRT</i> (Panel b), <i>Swift/BAT</i> (Panel b) and <i>INTEGRAL/IBIS</i> (Panel d) lightcurves of IGR J17091-3624 during its 2011-2013 outburst. Arrows mark times at which <i>XMM-Newton</i> (blue), <i>Chandra</i> (red) or <i>Suzaku</i> (magenta) observed IGR J17091-3624. The cyan line represents MJD 55963, the approximate time IGR J17091-3624 transitions from the soft to the hard state (Drave et al., 2012). <i>RXTE/PCA</i> (Jahoda et al., 1996) data are for the 2–16 keV energy band and taken from (Altamirano et al., 2011b), <i>Swift/BAT</i> (Barthelmy, 2000) data are for 15–50 keV, <i>Swift/XRT</i> (Burrows et al., 2003) data are for 0.3–10 keV and <i>INTEGRAL/ISGRI</i> (Ubertini et al., 2003) data are for 20-40 keV. Note that the data from <i>Swift/XRT</i> (Panel B) are shown with a logarithmic y-axis to better show the late time progression of the outburst. Data points are coloured according to the observing mode used. The <i>Swift/XRT</i> data from times later than MJD 56422 are shown to a different scale to better represent the post-outburst evolution of the source. All data are presented in 1 day bins, except for data from <i>Swift/BAT</i> which is presented in 4 day bins. See also Figure 4.3, in which data from <i>RXTE/PCA</i> is presented on a smaller scale. The Crab count rates used to normalise these data were $2300 \text{ cts s}^{-1} \text{ PCU}^{-1}$, 747.5 cts s^{-1} , 0.214 cts s^{-1} and 183.5 cts s^{-1} for <i>RXTE</i> , <i>Swift/XRT</i> , <i>Swift/BAT</i> and <i>INTEGRAL/ISGRI</i> respectively. <i>RXTE</i> data have not been corrected for the 25' offset to avoid contamination from GX 349+2, and for all instruments we implicitly assume that IGR J17091 presents a Crab-like spectrum.	20
4.3	Global 2–3.5 keV Lightcurves of IGR J17091-3524 during the 2011-2013 outburst, with each point corresponding to the mean Crab-normalised count rate of a single <i>RXTE</i> observation of the object (in turn corresponding to between 0.4 and 3.6 ks of data). In each lightcurve, every observation identified as belonging to a particular class (indicated on the plot) is highlighted. These are presented along with a characteristic lightcurve (inset) from an observation belonging to the relevant class. Each lightcurve is 250 s in length, and has a y-scale from 0 to $250 \text{ cts s}^{-1} \text{ PCU}^{-1}$. Data taken from Altamirano et al. 2011b.	28
4.4	A global colour-colour diagram (a), "soft" hardness-intensity diagram (b) and "hard" hardness-intensity diagram (c) of the 2011-2013 outburst of IGR J17091, using the colours H_{A1} and H_{A2} defined previously. Observations belonging to different classes have been highlighted in different colours. Data taken from Altamirano et al. 2011b.	29
4.5	Plots of the Class I observation 96420-01-01-00, orbit 0. <i>Top-left</i> : 1000 s lightcurve binned on 2 seconds to show lightcurve evolution. <i>Top-right</i> : Fourier Power Density Spectrum. <i>Bottom</i> : 500 s lightcurve binned on 2 seconds.	31

4.6	Plots of the Class II observation 96420-01-11-00, orbit 0. <i>Top-left</i> : 1000 s lightcurve binned on 2 seconds to show lightcurve evolution. <i>Top-right</i> : Fourier Power Density Spectrum. <i>Bottom</i> : Lightcurve binned on 2 seconds.	32
4.7	Plots of the Class III observation 96420-01-04-01, orbit 0. <i>Top-left</i> : 1000 s lightcurve binned on 2 seconds to show lightcurve evolution. <i>Top-right</i> : Fourier Power Density Spectrum. <i>Bottom</i> : Lightcurve binned on 2 seconds. Note that, to emphasise the behaviour of the lightcurve in this class, we have magnified the 500 s lightcurve y-scale by a factor of 2 compared with the lightcurves presented for other classes.	33
4.8	The Lomb-Scargle periodogram of observation 96420-19-01, orbit 0, with significance levels of 1, 2 and 3σ plotted. The peak at 0.31 Hz was used to define a QPO frequency when folding the data from this observation.	34
4.9	The hardness-intensity diagram (HID_1) of the Class III observation 96420-01-04-01, orbit 0. The data have been folded over a period of 79.61 s, corresponding to the peak frequency in the Lomb-Scargle spectrum of this observation. Inset is the folded lightcurve of the same data.	35
4.10	Plots of the Class IV observation 96420-01-05-00, orbit 0. <i>Top-left</i> : 1000 s lightcurve binned on 2 seconds to show lightcurve evolution. <i>Top-right</i> : Fourier Power Density Spectrum. <i>Bottom</i> : Lightcurve binned on 0.5 seconds.	36
4.11	<i>Top</i> : The hardness-intensity diagram (HID_1) of the Class IV observation 96420-01-05-00, orbit 0 showing an anticlockwise loop. The data have been folded over a variable period found with the algorithm described in Section 3.3.1. Inset is the folded lightcurve of the same data. <i>Bottom Left</i> : The hardness-intensity diagram of Class IV observations 96420-01-24-02 orbit 0, an example of a clockwise loop. <i>Bottom Right</i> : The hardness-intensity diagram of Class IV observation 96420-01-06-00 orbit 0, in which we were unable to ascertain the presence of a loop.	38
4.12	Plots of the Class V observation 96420-01-06-03, orbit 0. <i>Top-left</i> : 750 s lightcurve binned on 2 seconds to show lightcurve evolution. <i>Top-right</i> : Fourier Power Density Spectrum. <i>Bottom</i> : Lightcurve binned on 0.5 seconds.	39
4.13	A portion of the lightcurve of observation 96420-01-06-03, orbit 0, showing Type V_1 flares (highlighted in cyan) and Type V_2 flares (highlighted in red).	40
4.14	Every flare in all observations identified as Class V, plotted in a two-dimensional histogram of flare peak count rate against flare duration to show the two-population nature of these events.	41

4.15	<i>Top:</i> The hardness-intensity diagram (HID_1) of a type V_1 flaring region in Class V observation 96420-01-07-00, orbit 0 showing a clockwise loop. The data have been folded over a variable period found with the algorithm described in Section 3.3.1. Inset is the folded lightcurve of the same data. <i>Bottom Left:</i> The hardness-intensity diagram of Class V observation 96420-01-25-05 orbit 0, an example of an anticlockwise loop. <i>Bottom Right:</i> The hardness-intensity diagram of Class V observation 96420-01-25-06 orbit 0, in which we were unable to ascertain the presence of a loop.	42
4.16	Plots of the Class VI observation 96420-01-09-00, orbit 0. <i>Top-left:</i> 750 s lightcurve binned on 2 seconds to show lightcurve evolution. <i>Top-right:</i> Fourier Power Density Spectrum. <i>Bottom:</i> Lightcurve binned on 1 second. .	43
4.17	<i>Top:</i> The hardness-intensity diagram (HID_1) of the Class VI observation 96420-01-30-03, orbit 0 showing a clockwise loop. The data have been folded over a variable period found with the algorithm described in Section 3.3.1. Inset is the folded lightcurve of the same data. <i>Bottom Left:</i> The hardness-intensity diagram of Class VI observation 96420-01-30-04 orbit 0, an example of an anticlockwise loop. <i>Bottom Right:</i> The hardness-intensity diagram of Class VI observation 96420-01-09-03 orbit 0, in which we were unable to ascertain the presence of a loop.	45
4.18	Plots of the Class VII observation 96420-01-18-05, orbit 0. <i>Top-left:</i> 750 s lightcurve binned on 2 seconds to show lightcurve evolution. <i>Top-right:</i> Fourier Power Density Spectrum. <i>Bottom:</i> Lightcurve binned on 0.5 seconds.	46
4.19	A sliding window Lomb-Scargle spectrogram of Class VII observation 96420-01-18-05, showing power density spectra from an overlapping 32 s window moved 1 s at a time. The peak frequency of this low frequency QPO itself appears to oscillate with a frequency of ~ 5 mHz.	47
4.20	Plots of the Class VIII observation 96420-01-19-03, orbit 0. <i>Top-left:</i> 300 s lightcurve binned on 2 seconds to show lightcurve evolution. <i>Top-right:</i> Fourier Power Density Spectrum. <i>Bottom:</i> Lightcurve binned on 0.5 seconds. Inset is a zoom of the 25 s portion of the lightcurve highlighted in cyan, to show the second-scale structure in the lightcurve.	48
4.21	Plots of the Class IX observation 96420-01-35-02, orbit 1. <i>Top-left:</i> 1200 s lightcurve binned on 2 seconds to show lightcurve evolution. <i>Top-right:</i> Fourier Power Density Spectrum. <i>Bottom:</i> Lightcurve binned on 2 seconds.	49
4.22	<i>INTEGRAL/ISGRI</i> 150–300 keV significance map of a 2° region centred on the position of IGR J17091-3624, showing the first significant detection of this source above 150 keV. The detection significance is 7.6σ	51

4.23	1 ks segments of lightcurves taken from <i>Chandra</i> observations 12505, 12405 and 12406, showing Class I, Class VII and Class IX variability respectively. The lightcurve presented for observation 12505 is for the energy range 0.06-10 keV, while the other two lightcurves are for the energy range 0.5-10 keV. All three lightcurves are binned to 0.5 s.	52
4.24	Lightcurves of <i>XMM-Newton</i> observations 0677980201 and 0700381301, showing Class IV variability and the hard state respectively. Both lightcurves binned to 2 s. Data for observation 0677980201 is taken from <i>EPIC-MOS2</i> and data for observation 0700381301 is taken from <i>EPIC-pn</i>	54
4.25	$\nu P(\nu)$ -normalised co-added power density spectra of <i>XMM-Newton</i> observation 0700381301 and <i>Suzaku</i> observation 407037010. Both observations were taken simultaneously on September 29 2012 (MJD 56199). We sample observation 0700381301 up to a frequency of 10 Hz, while the 2 s time resolution of observation 407037010 results in a Nyquist frequency of 0.25 Hz.	55
4.26	A lightcurve of observation 96420-01-06-02, orbit 0, showing a transition in behaviour between Class IV (in cyan, see Section 4.3.2) and Class V (in red, see Section 4.3.2).	56
4.27	Every flare in all observations identified as Class III or Class IV, plotted in a two-dimensional histogram of flare peak count rate against flare duration to show the two-population nature of these events. Flares belonging to Class IV occupy the distribution at higher peak rate and lower duration, whereas flares belonging to Class III occupy the distribution at lower peak rate and higher duration.	59
4.28	Lightcurve from Class III observation 96420-01-10-01 of IGR J17091-3624, with pairs of primary and secondary count rate spikes highlighted in cyan and red respectively. The yellow region highlights a primary count rate spike that did not produce a secondary.	60
4.29	Mass of the compact object in IGR J17091-3624 plotted against its distance, for values of peak Eddington fractions of $F_{Edd} = 0.05, 0.1, 0.2$ and 0.33	66
6.1	Top: 2–15 keV <i>XMM</i> lightcurve from the TMSP PSR J1023+0038. Middle: 2–60 keV <i>RXTE</i> lightcurves from the Bursting Pulsar during its 1996 and 1997 outbursts, showing similar variability patterns to those seen in PSR J1023+0038. Bottom: 2–15 keV <i>XMM</i> lightcurve from the TMSP IGR J18245-2452. <i>XMM</i> lightcurves are shown from 2–15 keV so that they can be more directly compared with <i>RXTE</i>	75
6.2	Histograms of the 1 s binned count rates from all <i>RXTE</i> observations of Structured Bursting in the 1996 (left) and 1997(right) outbursts of the Bursting Pulsar. For the 1996 outburst, we fit the distribution with three Gaussians, while for the 1997 outburst we fit the distribution with 2 Gaussians. The individual Gaussians are plotted in solid lines, while the combined total is plotted in a dashed line.	76

6.3	A 7–60/2–7 keV hardness-intensity diagram for <i>RXTE</i> observation 10401-01-59-00; the lightcurve of this observation is shown in the inset. To correct for the high background of the region, we subtract the median count rate of <i>RXTE</i> observation 30075-01-24-00 from each band; at this time, GRO J1744-28 was in quiescence. We find a strong correlation between hardness and count rate, with a Spearman Rank Correlation Coefficient of 0.93. Data for the hardness-intensity diagram are binned to 10 s, while data for the lightcurve are binned to 5 s.	77
6.4	A plot of a number of objects ranging in scale from LMXBs and High-Mass X-ray Binaries (HMXBs) to Cataclysmic Variables (CVs) and Young Stellar Objects (YSOs) (blue diamonds). In each case, the object is plotted at the luminosity which defines its transition between propeller-mode accretion and free accretion. Campana et al., 2017 suggest that any object falling above the line of best fit accretes freely, whereas all objects below are inhibited by the propeller effect. The Bursting Pulsar (red circle) is consistent with approaching this line during periods of Structured Bursting. Errorbars on the Bursting pulsar represent the range of the reported magnetic fields (see Section 6.2) as well as a range of stellar radii between 10–20 km. The range in luminosity for the BP is calculated using 1.5-25 keV <i>RXTE</i> /PCA flux, assuming a distance of between 4–8 kpc (e.g. Kouveliotou et al., 1996; Gosling et al., 2007; Sanna et al., 2017c) and a bolometric correction factor of 1–3. Data on the other objects taken from Campana et al., 2017. L is the bolometric luminosity of the object in ergs s^{-1} , P is the period in s, R is the radius in cm and μ is the magnetic moment in Gauss cm^3	79

List of Tables

4.1	Chandra observations log covering the three observations considered in this paper. <i>I</i> refers to Imaging mode, <i>C</i> refers to CC33_Graded mode and <i>T</i> refers to Timed Exposure Faint mode. HETG refers to the High Energy Transmission Grating.	23
4.2	Lower and upper quartile count rates, fractional RMS and median colour averaged across all observations belonging to each class. Count rates and fractional RMS are taken from the full energy range of <i>RXTE/PCA</i> , and fractional RMS values are 2–60 keV taken from lightcurves binned to 0.5 s. Count rates are normalised for the number of PCUs active during each observation. All values are quoted as 1σ ranges.	30
4.3	A tally of the number of times we assigned each of our nine Variability Classes to an <i>RXTE</i> orbit. We have also calculated the amount of observation time corresponding to each class, and thus inferred the fraction of the time that IGR J17091 spent in each class. Note: the values in the Total Time column assume that each orbit only corresponds to a single variability Class.	30
4.4	Results from the IBIS/ISGRI analysis of the 2011–2013 Outburst of IGR J17091. The 20–40 keV flux is given in units of mCrab and (10^{-11} ergs s $^{-1}$ cm $^{-2}$). Conversion between counts and mCrab was obtained using an observation of the Crab taken during Revolution 1597 between MJD 57305.334 and 57305.894 and the conversion factors of Bird et al. (2016) and Bazzano et al. (2006).	50
4.5	The nine variability classes of IGR J17091-3624, showing the name of the closest corresponding variability class in GRS 1915+105. The names of GRS 1915+105 classes are taken from Belloni et al. (2000), where more detailed descriptions can be found. Eight additional classes of GRS 1915+105 have been described; we do not find analogies to these classes in IGR J17091-3624.	57
4.6	The six OBSIDs explicitly classified in Altamirano et al. (2011b). We also present the GRS 1915 class with which we implicitly label each OBSID in this paper.	64

A.1	Here is listed the Observation IDs for every <i>RXTE</i> observation that was used in this analysis, along with the variability class which has been assigned to it. <i>Orb.</i> is the orbit ID (starting at 0) of each observation segment, <i>Exp.</i> is the exposure time in seconds and X is the prefix 96420-01. This table is continued overleaf in Table A.2.	109
A.2	A continuation of Table A.1. <i>Orb.</i> is the orbit ID (starting at 0) of each observation segment, <i>Exp.</i> is the exposure time in seconds and X is the prefix 96420-01.	110

Dedication

To the memory of my brother Christopher, whose name will forever appear alongside my own.

Acknowledgements

This work was made possible by financial support from Science and Technology Facility Council (STFC) and the Royal Astronomical Society (RAS).

I would like to express sincere gratitude to my supervisor Dr. Diego Altamirano. Without his experience, incredible patience and willingness to push me to improve myself, this work would not have been possible.

I would like to thank Professor Tomaso Belloni, Professor Ranjeev Misra and Dr Andrea Sanna for hosting me at their respective institutes at various times in my studies. I also thank Professor Rudy Wijnands, Dr. Mayukh Pahari, Dr. Nathalie Degenaar and Professor Kazutaka Yamaoka for their contributions to our extensive collaborations.

I would like to thank my family for their unwavering support during this at-times arduous task. I also thank my friends and colleagues at the university of Southampton, in particular Mr. David Williams and Dr. Aarran Shaw, who have all in some way helped me to survive to the end of this process; whether they realise it or not.

Chapter 1

Introduction

Chapter 2

The Physics of Accretion

2.1 High-Mass and Low-Mass X-Ray Binaries

2.1.1 Black Hole LMXBs

2.1.2 Neutron Star LMXBs

2.2 The Shakura-Sunyaev Disk Model

XXXXX

2.3 GRS 1915+105 and IGR J17091-3624

XXXXX

2.3.1 A History of Models of GRS 1915-like Variability

One of the most best-studied classes of GRS 1915-like variability is Class ρ , also known as the ‘heartbeat’ class due to the resemblance of a Class ρ lightcurve to an electrocardiogram. It has been shown that hard X-ray photons lag soft X-ray photons in this class (e.g. Janiuk and Czerny, 2005; Massaro et al., 2010). All other classes in GRS 1915 which show quasi-periodic flaring behaviour also exhibit this phase lag.

Previous authors have established models to explain both the hard photon lag as well as the ‘heartbeat’-like flaring itself, generally based on the instability in a radiation-dominated disk first reported by Lightman and Eardley, 1974. Belloni et al., 1997a first proposed that the flaring is due to a rapid emptying of a portion of the inner accretion disk, followed by a slower refilling of these region over a viscous timescale. These authors divided data from a

given observation into equal-sized 2-Dimensional bins in count rate-colour space. A spectral model was then fit to each of these bins independently to perform ‘pseudo’-phase-resolved spectroscopy. They show that the quiescent time between flaring events correlates with the maximum inner disk radius during the flare; i.e., a correlation between the amount of the disk which is emptied and the time needed to refill it. They go on to suggest that their model is able to explain all flaring-type events seen in GRS 1915.

The scenario proposed by Belloni et al., 1997a was mathematically formalised by Nayakshin et al., 2000, who found that it was not consistent with a ‘slim’ accretion disk (Abramowicz et al., 1988) or with a disk in which viscosity α is constant with respect to radius. As such, their model consists of a ‘cold’ accretion disk with a modified viscosity law, a non-thermal electron corona and a transient ‘jet’ of discrete plasma emissions which are ejected when the bolometric luminosity approaches the Eddington Limit. In this model, Nayakshin et al., 2000 find that some formulations of $\alpha(r)$ result in the disk oscillating between two quasi-stable branches in viscosity-temperature space, over timescales consistent with those seen in the flaring of GRS 1915; they find that this occurs for accretion rates greater than 26% of the Eddington limit. They also find that by varying the functional form of $\alpha(r)$, their model gives rise to a number of lightcurve morphologies which generally match what is seen in data from GRS 1915. Janiuk et al., 2000 build on this model further by including the effect of the transient jet in cooling the disk; an effect not considered in the model by Nayakshin et al., 2000. In this formulation, Janiuk et al., 2000 find that GRS 1915-like variability can occur at luminosities as low as 16% of Eddington.

Belloni et al., 2000 found that variability in GRS 1915 can be described by transitions between three phenomenological states, which differ in luminosity and hardness ratio. This phenomenological scenario is at odds with the model of Nayakshin et al., 2000, which only results in two quasi-stable states.

Tagger et al., 2004 propose a magnetic explanation for the ejection of the inner accretion disk required by Nayakshin et al., 2000 and Janiuk et al., 2000. They suggest a limit cycle in which a poloidal magnetic field is advected towards the inner disk during the refilling of this region. This field is then destroyed in reconnection events, releasing energy which results in the expulsion of matter from the inner disk. They suggest that two of the three quasi-stable states proposed by Belloni et al., 2000 can be explained as states in the inner accretion disk with different values of plasma β . However, they are unable to simply account for a third quasi-stable state.

Janiuk and Czerny, 2005 attempt to explain the hard lag in the heartbeats of GRS 1915 more simply, by proposing that it is caused by the non-thermal corona smoothly adjusting to changes in luminosity from the disk. They base the variability of the disk on the model of Nayakshin et al., 2000, and show that the presence of a non-thermal corona which reacts to this variability naturally reproduces the lag behaviour seen in Class ρ in GRS 1915.

Merloni and Nayakshin, 2006 also propose a magnetic explanation for the reformulation of

$\alpha(r)$ required by the model of Nayakshin et al., 2000. Assuming that the viscosity in the accretion disk is dominated by turbulence due to magnetorotational instability, they find that allowing for a magnetically dominated corona naturally allows for the forms of $\alpha(r)$ required by Nayakshin et al., 2000.

Zheng et al., 2011 suggest that, when the effects of a magnetic field are included, the accretion rate threshold for GRS 1915-like variability should be $\sim 50\%$ of Eddington; significantly higher than the 16% or 26% reported by Janiuk et al., 2000 or Nayakshin et al., 2000. They go on to suggest that this sort of variability is only seen in GRS 1915 due to this source having the highest accretion rate of all permanently soft-state sources. As such, this scenario still relies on a high accretion rate to trigger GRS 1915-like variability. However, magnetohydrodynamic simulations of a radiation dominated inner disk performed by Hirose et al., 2009 suggest that the thermal instabilities required by models of heartbeat should not arise at any value of accretion rate.

Xue et al., 2011 derive a mathematical model of the evolution of a slim accretion disk around a Kerr black hole. They hypothesize that the spin of the black hole, not the accretion rate, may be the driving factor behind GRS 1915-variability. However, they find that the morphology of X-ray lightcurves from such a disk only has a weak dependence on the spin of the black hole, ruling this out as a possible explanation.

Neilsen et al., 2011 performed phase-resolved spectroscopy of the ρ class in GRS 1915. They find a hard ‘spike’ after each flare, which they associate with the hard lag in this class previously noted by e.g. Janiuk and Czerny, 2005. They propose a scenario in which high-velocity winds formed by the ejection of matter from the inner disk interact directly with the corona after a light travel time. The corona then re-releases this energy as a hard bremsstrahlung pulse, causing the hard count rate spike seen in phase-resolved spectra. They expand this scenario in Neilsen et al., 2012 to suggest that this mechanism can explain all classes in GRS 1915 which display ρ -like flaring. However, this scenario still relies on the model of Nayakshin et al., 2000 to generate the instability in the disk, and it implies that hard photons should always lag soft photons in heartbeat-like variability classes.

In their fitting, Neilsen et al., 2011 consider three spectral models:

1. An absorbed disk black body with a high energy cutoff, of which some fraction has been Compton upscattered
2. An absorbed disk black body with a high energy cutoff, plus a Compton component with a seed photon spectrum tied to the emission from the disk
3. An absorbed disk black body plus a Compton component with a seed photon spectrum tied to the emission from the disk and a bremsstrahlung component

They find that the first of these models (Model i) is the best fit to the data.

Mineo et al., 2012 also performed psuedo-phase-resolved spectroscopy of the ρ class in GRS 1915, using a number of different spectral models to Neilsen et al., 2011 but a

significantly lower phase resolution. In this work, the authors consider six models:

1. A multi-temperature disk black body plus a corona containing both thermal and non-thermal electrons (as formulated by Poutanen and Svensson, 1996)
2. A multi-temperature disk black body plus a multi-temperature disk black body plus a power law
3. A multi-temperature disk black body plus an independent Compton component
4. A multi-temperature disk black body plus a power law plus reflection from the outer disk
5. A model of Comptonization due to the bulk-motion of matter in the disk
6. A multi-temperature disk black body plus a power law plus a standard black body

With the exception of Models *i* and *vi*, the authors find that none of these models are able to satisfactorily fit the data in each of their phase bins independently. As there is no reasonable physical explanation behind Model *vi*, the authors only consider Model *i*. Their results suggest a large reduction of the corona luminosity during each heartbeat flare, which they interpret as the corona condensing onto the disk. They also find that their results are consistent with GRS 1915 having a slim disk, but inconsistent with the hard lag being caused by photon upscattering in the corona.

Massa et al., 2013 found that the magnitude of the lag between hard and soft photons in the ρ -class of GRS 1915 is not constant. They found that the lag varies between $\sim 3\text{--}10$ s, and correlates strongly with count rate. The magnitude of the lag, therefore, is too large to be simply due to a light travel time to the corona from the disk. The authors suggest that their results are instead consistent the thermal adjustment of the inner disk itself as part of the instability limit cycle invoked to explain the flares.

Massaro et al., 2014a constructed a set of differential equations to mathematically explain the behaviour of the oscillator underlying ρ -like flaring in GRS 1915. They find that a change between variability classes likely corresponds to a change in global accretion rate, but that the accretion rate within the ρ class is constant. This model reproduces the count rate-lag correlation reported by Massa et al., 2013, as well as a previously reported correlation between flare recurrence time and count rate (Massaro et al., 2010).

Mir et al., 2016 instead propose a model of variability in the outer disk propagating inwards to the hotter inner disk. They propose a model that explains both the hard lag of the fundamental frequency associated with the heartbeat flares, but also the hard lag of the first harmonic. In contrast to the findings of Massaro et al., 2014a, their scenario requires a sinusoidal variation in the global accretion rate as a function of time.

More recently, Zoghbi et al., 2016 found that the reflection spectrum from GRS 1915 does not match what would be expected from the inner disk behaviour assumed by e.g.

Nayakshin et al., 2000. They again perform phase-resolved spectroscopy and fit a number

of complex spectral models, finding that their data is best-described by the emergence of a bulge in the inner disk which propagates outwards during each flare.

2.4 Type II Burst Sources

XXXXX

Chapter 3

Tools & Methods

3.1 Instrumentation

3.1.1 The *Rossi X-Ray Timing Experiment*

The *Rossi X-Ray Timing Experiment*, more commonly known as *RXTE*, was a NASA-operated satellite launched from Cape Canaveral on December 30, 1995 (Bradt et al., 1993). *RXTE* was primarily an X-ray observatory, constructed specifically to study X-ray QPOs seen in X-ray Binaries (Bradt et al., 1990). The observatory operated until January 5, 2012, when it was decommissioned.

RXTE contained three instruments. The main instruments consisted of two X-ray telescopes: the Proportional Counter Array ('PCA', Jahoda et al., 1996) and the High Energy X-Ray Timing Experiment ('HEXTE' Gruber et al., 1996). The satellite also carried an X-ray All-Sky Monitor (ASM, Levine et al., 1996).

PCA consisted of 5 Proportional Counting Units (PCUs) which were sensitive between ~ 2 –60 keV. The instrument had an excellent time resolution approaching $1\ \mu\text{s}$, and an energy resolution of $\sim 18\%$ at 6 keV. X-rays were guided onto the detectors by a collimator, resulting in an instrument field of view with a full-width half-maximum of 1° . There was no angular resolution.

3.1.2 The Neil Gehrels Swift Observatory

3.1.3 XMM-Newton

3.1.4 Chandra

3.1.5 Suzaku

3.1.6 NuStar

3.1.7 INTEGRAL

3.2 Raw Data Extraction

3.3 Lightcurve Analysis

3.3.1 Flare-Finding Algorithm

The algorithm used to find flares is performed as such (see also Figure 3.1):

1. Choose some threshold values T_L and T_H . Set the value of all datapoints below T_L to zero.
2. Retrieve the x-co-ordinate of the highest value remaining in the dataset. Call this value x_m and store it in a list.
3. Set the value of point at x_m to zero.
4. Scan forwards from x_m . If the selected point has a nonzero value, set it to zero and move to the next point. If the selected point has a zero value, move to step (v).
5. Scan backwards from x_m . If the selected point has a nonzero value, set it to zero and move to the previous point. If the selected point has a zero value, move to step (vi).
6. Retrieve the y-co-ordinate of the highest value remaining in the dataset. Call this y_m .
7. If $y_m > T_H$, repeat steps (ii)–(vi). If $y_m < T_H$, proceed to step (viii).
8. Restore the original dataset.
9. Retrieve the list of x_m values found in step (ii). Sort them in order of size.
10. For each pair of adjacent x_m values, find the x-coordinate of the datapoint between them with the lowest y-value. Call these values x_c .
11. This list of x_c can now be used to demarcate the border between peaks.

The values T_L and T_H can also be procedurally generated for a given piece of data:

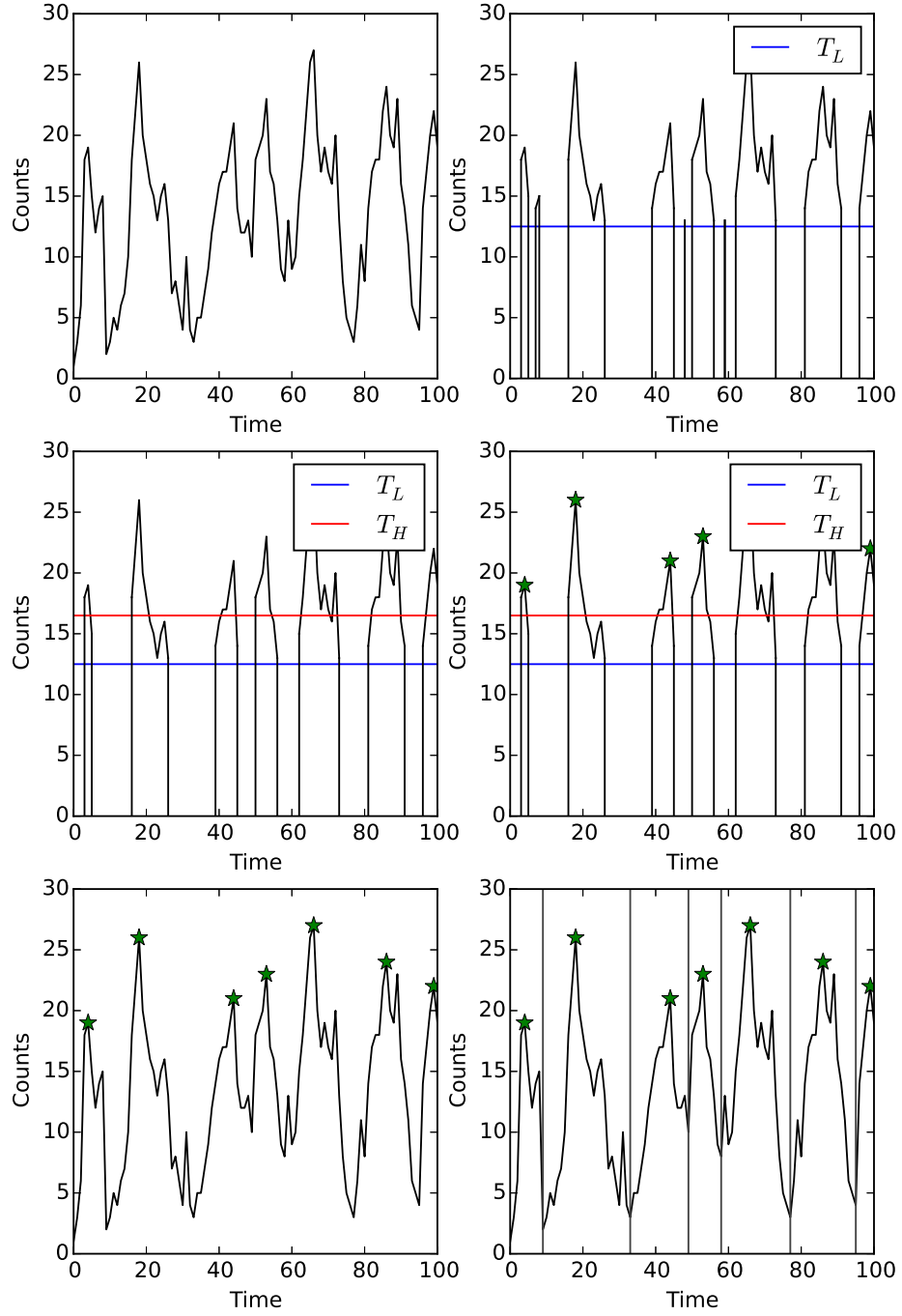


Figure 3.1: From top-left: (i) An untouched data-set. (ii) The dataset with all $y < T_L$ removed. (iii) The dataset with all contiguous nonzero regions with $\max(y) < T_H$ removed. (iv) The peak x-values x_m . (v) The restored dataset with the peak x-values x_m highlighted. (vi) The boundaries between adjacent peaks.

1. Select a small section of the dataset or a similar dataset (containing ~ 20 peaks by eye) and note the location x_e of all peaks found by eye.
2. Let P_L and P_H be two arbitrary values in the range $[0, 100]$.
3. Let T_L (T_H) be the P_L th (P_H th) percentile of the y -values of the subsection of dataset.
4. Run the flare-finding algorithm up to step (ix). Save the list of x_m .
5. Split the dataset into bins on the x -axis such as the bin width $b \ll p$, where p is the rough x -axis separation between peaks.
6. For each bin, note if you found any value in x_m falls in the bin and note if any value of x_e falls in the bin.
7. Using each bin as a trial, compute the Heidke Skill Score (Heidke, 1926) of the algorithm with the method of finding peaks by eye:

$$HSS = \frac{2(AD - BC)}{(A + B)(B + D) + (A + C)(C + D)} \quad (3.1)$$

Where A is the number of bins that contain both x_e and x_m , B (C) is the number of bins that contain only x_m (x_e) and D is the number of bins which contain neither (Kok, 2000).

8. Repeat steps (iii)–(vii) for all values of $P_H > P_L$ for P_L and P_H in $[1, 100]$. Use a sensible value for the resolution of P_L and P_H . Save the HSS for each pair of values
9. Locate the maximum value of HSS, and note the P_L and P_H values used to generate it. Use these values to generate your final T_L and T_H values.

We show an example of Heidke skill score grid for this algorithm, applied to a Class IV observation, in Figure 3.2.

3.4 Timing Analysis

3.5 Spectral Analysis

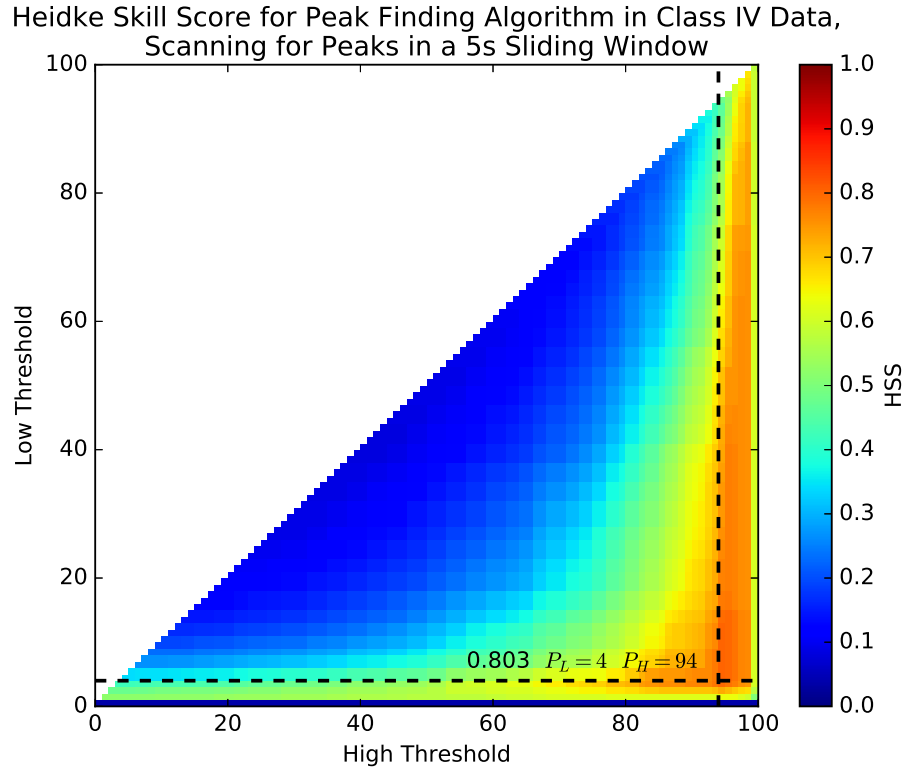


Figure 3.2: The Heidke Skill score of a Class IV observation of IGR J17091-3624 for a selection of different values P_L and P_H .

Chapter 4

Variability in IGR J17091-3624: Classification

4.1 Introduction

X-ray binaries are systems in which a black hole or neutron star accretes matter from a stellar companion, and they provide us with opportunities to test how accretion takes place in the most extreme physical regimes. Some X-ray Binaries are believed to be accreting at very close to the Eddington limit, the limit at which the radiation pressure on accreting material is equal to the force due to gravity. As such, these objects can also provide a laboratory with which to explore accretion in radiation pressure-dominated systems (White and Zhang, 1997).

Low Mass X-ray Binaries (hereafter LMXBs) are a subclass of X-ray binary in which the compact object accretes matter transferred to it due to a Roche-lobe overflow from the companion star (e.g. Paczynski, 1979). In general, accretion in LMXBs is a variable process, with variability seen on timescales from milliseconds to decades. On the shortest timescales the X-ray lightcurves of these objects can show band-limited noise and low-frequency quasi-periodic oscillations (QPOs) at frequencies from \sim mHz to \sim 200 Hz (e.g. van der Klis, 1989). Black hole binaries also show so-called ‘high frequency QPOs’ (e.g. Remillard et al., 1999a,b; Belloni et al., 2002; Belloni and Motta, 2016), thought to be caused by motion of matter in the innermost region of the accretion disk (e.g. Stefanov, 2014).

Three sources – GRS 1915+105, IGR J17091-3624 and the neutron star ‘Rapid Burster’ (MXB 1730-335) – also show a variety of exotic variability on timescales of seconds to minutes in addition to the kinds of variability seen in other LMXBs. This exotic variability consists of quasi-periodic flares, dips and other high-amplitude behaviours (e.g. Belloni et al., 2000; Altamirano et al., 2011b; Bagnoli and in’t Zand, 2015). The second-to-minute-scale lightcurve profiles of these sources change over timescales of days.

In GRS 1915+105 and IGR J17091-3624, this behaviour can be described as a set of ‘variability classes’. These classes themselves vary widely in terms of flux, structure, periodicity and spectral properties.

GRS 1915+105 (Castro-Tirado et al., 1992), hereafter GRS 1915, is a black hole LMXB which accretes at between a few tens and 100% of its Eddington Limit (e.g. Vilhu, 1999; Done et al., 2004; Fender and Belloni, 2004; Reid et al., 2014). Most LMXBs go through periods of low-intensity ‘quiescence’ and high-intensity ‘outbursts’, the latter consisting of black-body dominated ‘soft’ and power-law dominated ‘hard’ spectral states. However, GRS 1915 has been in outburst since its discovery in 1992 (Castro-Tirado et al., 1992). GRS 1915 is also notable for the incredible variety and complexity of variability classes it exhibits (e.g. Yadav et al., 2000; Belloni et al., 2000) in addition to the less exotic variability seen in other black hole binary systems. GRS 1915 additionally shows high-frequency and low frequency QPOs similar to those seen in other black hole LMXBs (Morgan et al., 1997). In total, 15 distinct variability classes have been observed (Belloni et al., 2000; Klein-Wolt et al., 2002; Hannikainen et al., 2007; Pahari and Pal, 2009). This remarkable range of behaviour is believed to be caused by instability in the inner accretion disc (e.g. Janiuk et al., 2000; Nayakshin et al., 2000), which is in turn caused by the existence of a radiation pressure dominated regime in the inner disc (e.g. Done et al., 2004). Accounting for this complexity could be key to our understanding of radiation-dominated accretion regimes.

One of the best-studied variability classes of GRS 1915 is the highly regular flaring ρ , or ‘heartbeat’, class, so named for the similarity of its lightcurve to an electrocardiogram. It has been shown that hard X-ray photons tend to lag soft ones in this class (e.g. Janiuk and Czerny, 2005; Massaro et al., 2010). Numerical models derived from Shakura and Sunyaev, 1973 which reproduce this lag can also reproduce other flaring classes seen in GRS 1915 (e.g. Nayakshin et al., 2000; Massaro et al., 2014b). These numerical models predict that GRS 1915-like variability should be seen in systems accreting with a global Eddington fraction of $\gtrsim 0.26$ (Nayakshin et al., 2000). However, other LMXBs (e.g. GX 17+2, Kuulkers et al., 2002, and V404 Cyg, Huppenkothen et al., 2016) have been observed to exceed this Eddington fraction without displaying GRS 1915-like variability.

Neilsen et al. (2011) proposed a physical scenario, based on the mathematical model proposed by Nayakshin et al. (2000), to explain the presence of the hard lag in the flaring classes of GRS 1915. This is outlined schematically in Figure 4.1. First, an overdensity of matter forms via the thermal-viscous Lightman-Eardley Instability (Lightman and Eardley, 1974) and propagates inwards through the accretion disc. This destabilises the disc, collapsing its inner radius and vastly increasing photon emission. If the local Eddington Limit in the inner accretion disc is then approached, extreme outflows are triggered that deplete the inner accretion disc and allow the cycle to begin again. As the matter ejected from the disc collides with the non-thermal ‘corona’ above the central object, a flash of hard Bremsstrahlung radiation is produced. This causes a hardening of the spectrum and an

apparent lag between soft and hard photons. Janiuk and Czerny (2005) instead propose that the lag is caused by the corona smoothly adjusting to the changing brightness of the disc after a light travel time.

The black hole candidate LMXB IGR J17091-3624 (hereafter J17091) was discovered in outburst by *INTEGRAL* in 2003 (Kuulkers et al., 2003). In 2011, it again went into outburst (Krimm and Kennea, 2011). GRS 1915-like variability was discovered in its lightcurve, as well as high-frequency QPOs which behave much like the QPOs seen in GRS 1915 (Altamirano et al., 2011b,a; Altamirano and Belloni, 2012). As IGR J17091 is around a factor of 20 fainter at 2–25 keV than GRS 1915, this object has either a lower black hole mass M , a lower accretion rate \dot{m} or lies at a larger distance D than GRS 1915. Assuming by analogy with GRS 1915 that IGR J17091 is accreting at its Eddington rate, the black hole must have a mass of $M \lesssim 3M_{\odot}$ or lie at a distance of $D \gtrsim 20$ kpc (Altamirano et al., 2011b). However, independent estimates based on empirical relationships between black hole mass and high-frequency QPOs have suggested values of M between ~ 8.7 and $15.6 M_{\odot}$ (Rebusco et al., 2012; Iyer et al., 2015b,a), while multi-wavelength observations of the hard-to-soft state transition have suggested values of D between ~ 11 and ~ 17 kpc (Rodríguez et al., 2011a). This implies that IGR J17091 may have an accretion rate \dot{m} that is significantly below its Eddington rate.

The suggestion that IGR J17091 accretes at significantly below the Eddington Limit raises several questions. Despite evidence of disc winds in IGR J17091 faster than $0.03c$ (King et al., 2012), the wind generation procedure described in Neilsen et al. (2011) cannot take place without near-Eddington-limited accretion. Additionally, it makes it increasingly unclear what differentiates IGR J17091 and GRS 1915 from the vast majority of LMXBs which do not display such complex behaviour, and what physical system properties are required for GRS 1915-like variability to be observed. This latter point was further complicated by the observation of GRS 1915-like variability in 2 out of 155 *RXTE* observations of the Rapid Burster (Bagnoli and in’t Zand, 2015). As thermonuclear (Type I) X-ray bursts are also seen in the Rapid Burster (Hoffman et al., 1978), it is known to contain a neutron star. As such, the presence of variability classes in this object rules out any black hole-specific effects as the cause of the complex variability. In addition to this, the persistent luminosity of the Rapid Burster during periods of GRS 1915-like variability is known to be no greater than $\sim 10\%$ of its Eddington limit (Bagnoli et al., 2015).

Accounting for GRS 1915-like variability is required for a complete understanding of the physics of accretion in LMXBs. As such, Belloni et al. (2000) performed a complete model-independent analysis of variability classes in GRS 1915. This work highlighted the breadth and diversity of variability in GRS 1915, and allowed these authors to search for features common to all variability classes. For example, Belloni et al. (2000) also found that every variability class can be expressed as a pattern of transitions between three quasi-stable phenomenological states.

Previous works have noted that some of the variability classes seen in IGR J17091-3624

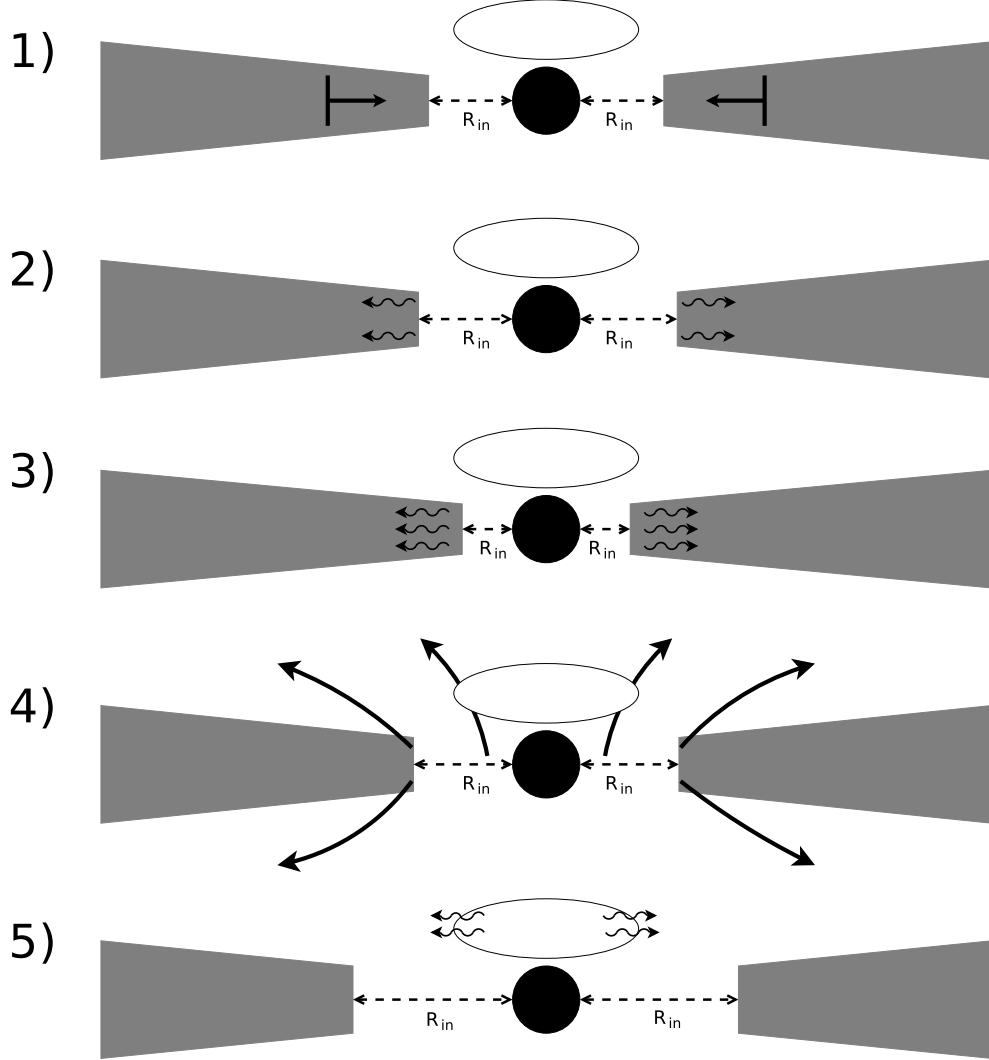


Figure 4.1: A schematic diagram illustrating the process described by Neilsen et al. (2011) to describe the ρ variability class in GRB 1915+105. 1) The X-ray emission from the system originates from both the accretion disc truncated at an inner radius r_{in} (grey) and a cloud of non-thermal electrons (white ellipse). At some time t , an overdensity in the accretion disc (formed by the Lightman-Eardley Instability) propagates inwards towards r_{in} . 2) As the inner disc heats up, r_{in} begins to slowly increase due to an increase in photon pressure. This destabilises the disc. 3) At some critical density, the disc becomes too unstable and collapses inwards, greatly decreasing r_{in} and raising the inner disc temperature. 4) The sudden increase in emission exceeds the local Eddington limit at r_{in} , ejecting matter from the inner accretion disc in the form of extreme winds. 5) Having been excited by matter in the winds passing through it, the non-thermal electron cloud emits a hard Brehmsstrahlung ‘pulse’.

appear very similar to those seen in GRS 1915 (e.g. Altamirano et al., 2011b; Zhang et al., 2014). However, although ρ -like classes in the two objects both show lags between hard and soft X-rays photons, these lags appear to possess different signs (Altamirano et al., 2011b). Additionally, at least two variability classes have been reported in IGR J17091 which have not yet been reported in GRS 1915 (Pahari et al., 2012). Previous works have described some of the behaviour seen in IGR J17091 in the context of the variability classes described by Belloni et al. 2000 for GRS 1915 (e.g. Altamirano et al., 2011b; Pahari et al., 2014). To further explore the comparison between GRS 1915 and IGR J17091, here we perform the first comprehensive model-independent analysis of variability classes in IGR J17091 using the complete set of *RXTE* (Bradt et al., 1993) data taken of the 2011-2013 outburst of the object. We also use data from all other X-ray missions that observed the source during this time to analyse the long-term evolution of the outburst.

4.2 Data and Data Analysis

In this paper, we report data from *RXTE*, *INTEGRAL*, *Swift*, *Chandra*, *XMM-Newton* and *Suzaku* covering the 2011-2013 outburst of IGR J17091. Unless stated otherwise, all errors are quoted at the 1σ level.

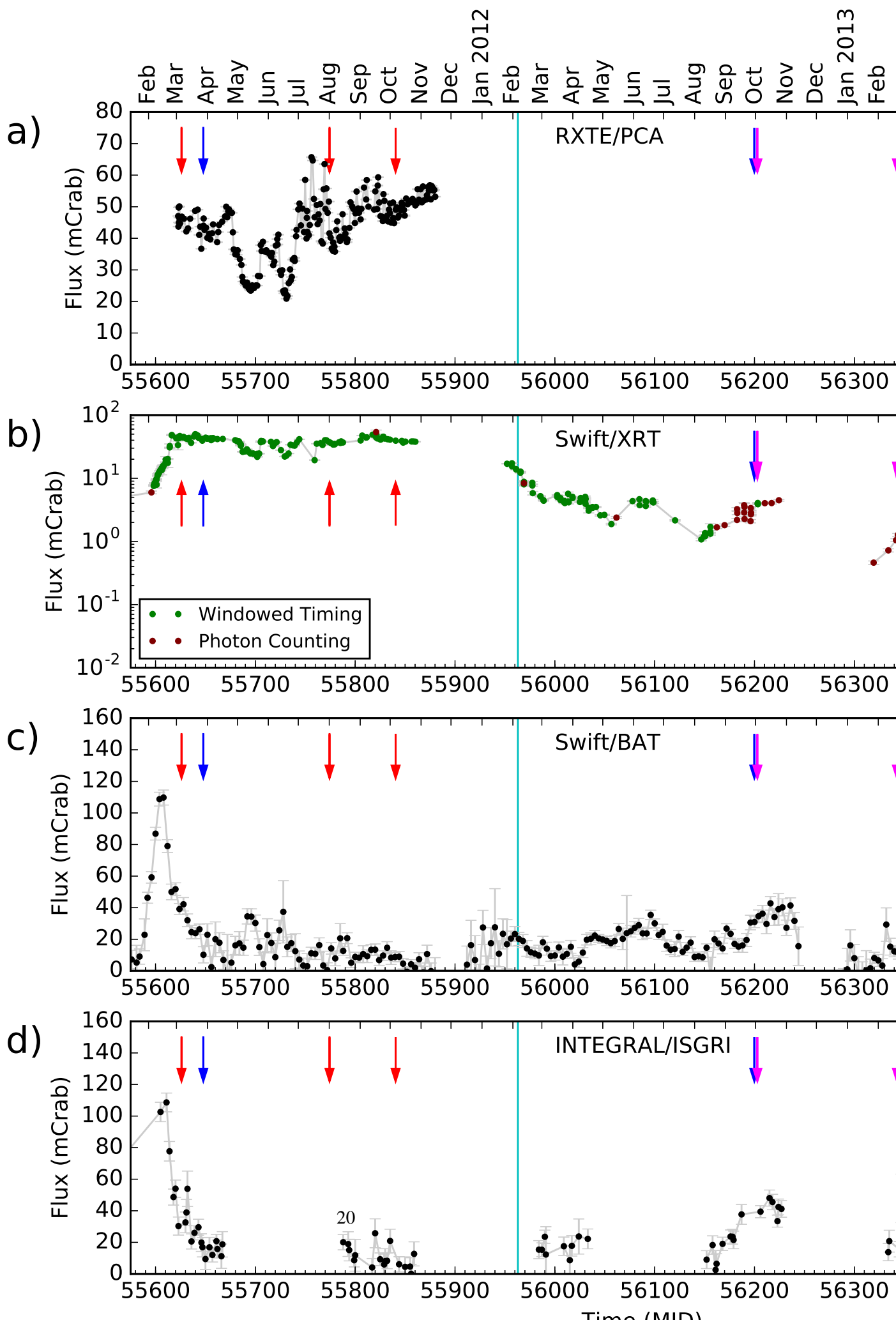
In Figure 4.2 we present long-term lightcurves from *RXTE*, *INTEGRAL* and *Swift* with one datapoint per observation, as well as indicating when during the outburst *Chandra*, *XMM-Newton* and *Suzaku* observations were made.

4.2.1 *RXTE*

For our variability study, we focus on the data from the Proportional Counter Array (*PCA*, Jahoda et al., 1996) aboard the Rossi X-Ray Timing Experiment (*RXTE*, Bradt et al., 1993). We analysed all 2011 *PCA* observations of IGR J17091, corresponding to OBSIDs 96065-03, 96103-01 and 96420-01. The observations taken for proposals 96065-03 and 96103-01 were contaminated by the nearby X-ray source GX 349+2 (Altamirano et al., 2011b; Rodriguez et al., 2011b). As such we only use observations performed for proposal 96420-01, corresponding to a total of 243 orbits from 215 separate observations. These were offset by 25' such that GX 349+2 was not in the 1° *PCA* field of view. *RXTE* was decommissioned during a period of Sun constraint centred on MJD 55907, and hence the last observation of IGR J17091 was taken on MJD 55879.

We extracted data from the native FITS format using our own software¹. To perform medium- to high-frequency (≥ 1 Hz) timing analysis, we merged files formatted in *PCA*'s 'Good Xenon' data mode and extracted their data at the maximum time resolution ($\sim 9.5 \times 10^{-7}$ s) without accounting for the background. We divided these data into 128 s

¹<https://github.com/jmcourt/pantheon>



segments as this allowed us to reach frequencies below ~ 0.015 Hz, partly sampling the high amplitude quasi-periodic flaring behaviour seen in many classes. Using the Fast Fourier Transform (FFT), we produced the power spectrum of each segment separately. We then averaged these spectra to create a one co-added Power Density Spectrum (PDS) for each observation.

For low-frequency (≤ 1 Hz) timing and correlated spectral/timing analysis, we rebinned the data to 0.5 s and normalised count rates by the number of proportional counters (PCUs) active in each observation. Our choice of 1 Hz allows us to analyse high amplitude ‘flaring’ behaviour (seen at frequencies $\lesssim 0.5$ Hz) separately from the lower-amplitude behaviour seen at $\gtrsim 5$ Hz.

We split the data into three energy bands: A (*PCA* channels 0–14, ~ 2 –6 keV), B (*PCA* channels 15–35, ~ 6 –16 keV) and C (*PCA* channels 36–255, ~ 16 –60 keV). We chose these energy bands to be consistent with the energy bands used by the model-independent classification of variability classes of GRS 1915 in Belloni et al. (2000). For each of the energy-filtered lightcurves produced we estimated background using `pcabackest` from the `FTOOLS` package (Blackburn, 1995) with the *PCA* faint source background model². In all observations, we found that counts in the C band were consistent with background. We then created Lightcurves L_A and L_B from background-subtracted photons counted in the A and B bands respectively. We used these lightcurves to define the full-band lightcurve ($L_T = L_A + L_B$) and the soft colour ($C_1 = L_B/L_A$) of each observation. To complement the Fourier spectra, we also constructed Generalised Lomb-Scargle Periodograms of L_T from each dataset, a modified version of the standard Lomb-Scargle periodogram (Lomb, 1976; Scargle, 1982) that takes into account errors in the dataset (Irwin et al., 1989). Using the Lomb-Scargle periodogram instead of the Fourier periodogram here allows us to sample the low-frequency behaviour of lightcurves with data gaps. This is important, for example, in lightcurves which show two populations of flares, as it allows each population to be studied independently by cropping the other from the lightcurve.

We also used data from Altamirano et al. 2011b to sample the long-term colour evolution of IGR J17091. We use 2 hardness ratios defined by Altamirano et al.: H_{A1} and H_{A2} , corresponding to the ratios of the 2–3.5 keV band against the 3.5–6 keV band and the 6–9.7 keV band against the 9.7–16 keV band respectively.

When possible, if low-frequency peaks were present in the Lomb-Scargle spectrum of an observation, we used the position of the highest peak to define a value for a period. This period was then used to rebin data by phase (or ‘fold’ the data) to search for recurrent hysteretic patterns in the hardness-Intensity diagram (hereafter HID_1 , a plot of L_T against C_1). We found that quasi-periodic oscillations in our observations tended to show significant frequency shifts on timescales shorter than the length of the observations. As such, we employed the variable-period folding algorithm outlined in Section 3.3.1 where appropriate.

²http://heasarc.gsfc.nasa.gov/FTP/xte/calib_data/pca_bkgd/Faint/pca_bkgd_cmfaint17_eMv20051128.mdl

For cases in which this algorithm was not appropriate, we considered small sections of each lightcurve, with a length equivalent to small number of periods, before performing folding.

Additionally, in observations which showed a pattern of high-amplitude X-ray flaring in L_T , we used our own algorithm to find individual flares (this algorithm is described in Section 3.3.1) and collect statistics on the amplitude, duration and profile of these events.

A list of all observations used in this study can be found in Appendix A.

4.2.2 *Swift*

In this paper, we consider data from the Burst Alert Telescope (*BAT*, Barthelmy 2000), and the X-ray Telescope (*XRT*, Burrows et al. 2003) aboard Swift Gamma-ray Burst Mission (Gehrels, 2004). IGR J17091-3624 was observed with *XRT* for a total of 172 pointed *XRT* observations between MJDs 55575 and 56600, corresponding to Target IDs 31921, 34543, 30967, 30973, 31920, 35096, 67137, 81917, 522245, 677582 and 677981. These observations were interrupted during sun constraints centred on MJDs 55907 and 56272. We created a long-term 0.3–10 keV *Swift/XRT* light curve, with one bin per pointed observation, using the online light-curve generator provided by the UK Swift Science Data Centre (UKSSDC; Evans et al., 2007). We have also created a long-term 15–50 keV lightcurve using the publicly available *Swift/BAT* daily-averaged light curve³. These are shown in Figure 4.2 Panels (b) and (c) respectively.

4.2.3 *INTEGRAL*

The INTErnational Gamma Ray Astrophysical Laboratory (*INTEGRAL*, Winkler et al., 2003) is a medium-sized ESA mission launched in 2002. Unique hard X-ray (15–1000 keV with the ISGRI detector plane) sensitivity and wide field of view make *INTEGRAL* ideally suited to surveying the hard X-ray sky (see Bird et al. (2016) and Krivonos et al. (2015) for recent surveys).

INTEGRAL observations are divided into short (~2 ks) pointings called Science Windows (ScWs). We analyse all available observations of IGR J17091 with *INTEGRAL/IBIS* (Ubertini et al., 2003) between MJD 55575–55625 where the source is less than 12 degrees from the centre of the field of view and where there is more the 1 ks of good ISGRI time per ScW. This corresponds to the spectrally hardest period of the 2011–2013 outburst. The filtering of observations results in a total of 188 Science Windows which were processed using the Offline Science Analysis (OSA) software version 10.2 following standard data reduction procedures⁴ in four energy bands (20–40, 40–100, 100–150, 150–300 keV). These bands were selected as they are standard energy bands used in the surveys of Bird et al. (2016) and Bazzano et al. (2006) and allow comparison to these previous works.

³<http://swift.gsfc.nasa.gov/results/transients/weak/IGRJ17091-3624/>

⁴<http://www.isdc.unige.ch/integral/analysis>

OBSID	Instrument	Grating	Exposure (ks)	Mode	MJD
12505	<i>HRC-I</i>	NONE	1.13	<i>I</i>	55626
12405	<i>ACIS-S</i>	HETG	31.21	<i>C</i>	55774
12406	<i>ACIS-S</i>	HETG	27.29	<i>T</i>	55840

Table 4.1: Chandra observations log covering the three observations considered in this paper. *I* refers to Imaging mode, *C* refers to CC33_Graded mode and *T* refers to Timed Exposure Faint mode. HETG refers to the High Energy Transmission Grating.

Images were created at the ScW level as well as a single mosaic of all Science Windows in each energy band.

4.2.4 *XMM-Newton*

In this paper we only consider data from the European Photon Imaging Camera (*EPIC* Bignami et al., 1990) aboard *XMM-Newton* (Jansen et al., 2001). *EPIC* consists of one telescope with a pn-type CCD (*EPIC-pn*, Strüder et al., 2001) and two telescopes with MOS CCDs (*EPIC-MOS1* and *-MOS2*, Turner et al., 2001).

XMM/Newton observed IGR J17091 thrice during the period from 2011–2013 (represented by the blue arrows in Figure 4.2). One of these (OBSID 0721200101) was made on 12 September 2013; we do not consider this observation further as IGR J17091 had returned to quiescence by this time (Altamirano et al., 2013). The remaining two observations, corresponding to OBSIDs 0677980201 and 0700381301 respectively, were taken on March 27 2011 (MJD 55647) and September 29 2012 (MJD 56199).

During observation 0677980201, *EPIC-pn* was operating in burst mode and *EPIC-MOS* was operating in timing mode. Given the low efficiency of burst mode, we only consider data from *EPIC-MOS* for this observation. During observation 0700381301, *EPIC-pn* was operating in timing mode, and thus we use data from *EPIC-pn* for this observation.

We used the *XMM-Newton* Science Analysis Software version 15.0.0 (SAS, see Ibarra et al., 2009) to extract calibrated event lists from *EPIC* in both observations. We used these to construct lightcurves to study the X-ray variability, following standard analysis threads⁵.

4.2.5 *Chandra*

In this paper we consider data from the Advanced CCD Imaging Camera (*ACIS*, Nousek et al., 1987) and the High Resolution Camera (*HRC*, Murray et al., 1987) aboard *Chandra* (Weisskopf, 1999). *Chandra* made 7 observations of IGR J17091 during the period 2011–2013. Four of these observations were taken after IGR J17091 returned to quiescence, and we do not consider these further in this paper. The Chandra observations log is reported in Table 4.1.

⁵<http://www.cosmos.esa.int/web/xmm-newton/sas-threads>

We analysed these data using CIAO version 4.8 (Fruscione et al., 2006), following the standard analysis threads. In order to apply the most recent calibration files (CALDB 4.7.0, Graessle et al., 2006), we reprocessed the data from the three observations using the `chandra_repro` script⁶, and used this to produce data products following standard procedures.

The first Chandra observation (OBSID 12505) of this source was made shortly after it went into outburst in February 2011. It was a 1 ks observation performed to refine the position of the X-Ray source, using the High-Resolution Camera in Imaging mode (HRC-I). We created the 0.06–10 keV light curve accounting for the Dead Time Factor (DTF) to correct the exposure time and count rate, due to the deviation of the detector from the standard detection efficiency, using the `dmextract` tool in the CIAO software.

Two additional observations (OBSIDs 12405 and 12406) were performed within 214 days of this first observation, using the High Energy Transmission Grating Spectrometer (HETGS) on board *Chandra*. The incident X-Ray flux was dispersed onto ACIS using a narrow strip array configuration (ACIS-S). Continuous Clocking and Time Exposure modes were used in each observation respectively (see King et al., 2012 for further details). We exclude any events below 0.4 keV, since the grating efficiency is essentially zero below this energy. In the case of the OBSID 12405 observations we also excluded the Flight Grade 66 events in the event file, as they were not appropriately graded. We extracted the 0.5–10 keV HEGTS light curves, excluding the zeroth-order flux, adopting standard procedures.

4.2.6 *Suzaku*

In this paper, we only consider data from the X-ray Imaging Spectrometer (XIS, Koyama et al., 2007) aboard *Suzaku* (Mitsuda et al., 2007). *Suzaku* observed IGR J17091 twice during the period 2011–2013; a 42.1 ks observation on October 2–3, 2012 (MJD 56202–56203, ObsID: 407037010) and an 81.9 ks observation on February 19–21, 2013 (MJD 56342–56344, ObsID: 407037020). XIS consists of four X-ray CCDs (XIS 0, 1, 2 and 3), and all them except for XIS 2 were operating in the 1/4 window mode which has a minimum time resolution of 2 seconds.

We analysed the *Suzaku* data using *HEASOFT* 6.19 in the following standard procedures after reprocessing the data with `aepipeline` and the latest calibration database (version 20160607). We extracted XIS light curves in the 0.7–10 keV range, and subtracted background individually for XIS 0, 1 and 3 and then summed these to obtain the total background. We created Power density spectra (PDS) using `powspec` in the *XRONOS* package.

⁶See e.g. http://xcx.harvard.edu/ciao/ahelp/chandra_repro.html

4.3 Results

4.3.1 Outburst Evolution

The 2011-2013 outburst of IGR J17091-3624 was first detected with *Swift*/XRT on MJD 55595 (3 Feb 2011) (Krimm and Kennea, 2011), and was observed by *RXTE*, *Swift*/XRT, *Swift*/BAT and *INTEGRAL*/ISGRI (see Figure 4.2, Panels a, b, c, d respectively). There were also pointed observations by *XMM-Newton*, *Chandra* and *Suzaku* during this time (denoted by coloured arrows in Figure 4.2).

RXTE data were taken within the first week of the outburst, but they were heavily contaminated by the nearby source GX 349+2 (Rodriguez et al., 2011b). Thus these data are not considered here.

The onset of the outburst can be seen in the *Swift*/BAT lightcurve (Figure 4.2 Panel c). In a 22 day period between MJDs 55584 and 55608, the 15–50 keV intensity from IGR J17091 rose from ~ 9 mCrab to a peak of ~ 110 mCrab. This onset rise in intensity can also be seen in 0.3–10 keV *Swift*/XRT data and 20–40 keV *INTEGRAL*/ISGRI data.

After peak intensity, the 15–50 keV flux (*Swift*/BAT) began to steadily decrease, until returning to a level of ~ 20 mCrab by MJD 55633. A similar decrease in flux can be seen in the data obtained by *INTEGRAL* at this time (Figure 4.2 Panel (d)). However, there was no corresponding fall in the flux at lower energies; both the long-term 2–16 keV *RXTE* data and *Swift*/XRT data (Panels a and b respectively) show relatively constant fluxes of 45 mCrab between MJDs 55608 and 55633.

The significant decrease in high-energy flux during this time corresponds to IGR J17091 transitioning from a hard state to a soft intermediate state (Pahari et al., 2014). This transition coincides with a radio flare reported by Rodriguez et al. (2011a) which was observed by the Australian Telescope Compact Array (ATCA).

Altamirano et al., 2011c first reported a 10 mHz QPO in *RXTE* data on MJD 55634, evolving into ‘Heartbeat-like’ flaring by MJD 55639 (Altamirano et al., 2011a). Between MJDs 55634 and 55879, the global *RXTE* lightcurve shows large fluctuations in intensity on timescales of days to weeks, ranging from a minimum of ~ 1 mCrab on MJD 55731 to a maximum of ~ 66 mCrab on MJD 55756. The *Swift*/XRT lightcurve shows fluctuations that mirror those seen by *RXTE* during this period, but the amplitude of the fluctuations is significantly reduced.

Swift/XRT was unable to observe again until MJD 55952. Between this date and MJD 55989, *Swift*/XRT observed a gradual decrease in intensity corresponding to a return to the low/hard state (Drave et al., 2012).

Between MJD 55989 and the end of the outburst on MJD 56445, we see secondary peaks in the *Swift*/XRT, *Swift*/BAT and *INTEGRAL*/ISGRI lightcurves that evolve over timescales of $\lesssim 100$ days. Similar humps have been seen before in lightcurves from other objects, for

example the black hole candidate XTE J1650-500 (Tomsick et al., 2003) and the neutron stars SAX J1808.4-3658 (Wijnands et al., 2001) and SAX J1750.8-2900 (Allen et al., 2015). These humps are referred to as ‘re-flares’ (also as ‘rebrightenings’, ‘echo-outbursts’, ‘mini-outbursts’ or a ‘flaring tail’, e.g. Patruno et al., 2016). We see a total of 3 apparent re-flares in the *Swift*/BAT data, centred approximately at MJDs 56100, 56220 and 56375.

The observation with *XMM-Newton*/EPIC-*pn* on MJD 56547 (12 September 2013) recorded a rate of 0.019 cts s⁻¹. An observation with EPIC-*pn* in 2007, while IGR J17091 was in quiescence (Wijnands et al., 2012), detected a similar count rate of 0.020 cts s⁻¹. Therefore we define MJD 56547 as the upper limit on the endpoint of the 2011-2013 outburst. As such the outburst, as defined here, lasted for $\lesssim 952$ days.

After the end of the 2011-2013 outburst, IGR J17091 remained in quiescence until the start of a new outburst around MJD 57444 (26 February 2016, Miller et al., 2016).

4.3.2 *RXTE*

Using the data products described in Section 4.2, we assigned a model-independent variability class to each of the 243 *RXTE*/PCA orbits. To avoid bias, this was done without reference to the classes defined by Belloni et al. (2000) to describe the behaviour of GRS 1915.

Classes were initially assigned based on analysis of lightcurve profiles, count rate, mean fractional RMS (Vaughan et al., 2003), Fourier and Lomb-scargle power spectra and hardness-intensity diagrams. For observations with significant quasi-periodic variability at a frequency lower than ~ 1 Hz, we also attempted to fold lightcurves to analyse count rate and colour as a function of phase. When flares were present in the lightcurve, we used our algorithm (described in Section 3.3.1) to sample the distribution of parameters such as peak flare count rate, flare rise time and flare fall time. All parameters were normalised per active PCU, and fractional RMS values were taken from 2–60 keV lightcurves binned to 0.5 s. We identify nine distinct classes, labelled I to IX; we describe these in the following sections.

Although the criteria for assigning each class to an observation was different, a number of criteria were given the most weight. In particular, the detection, q -value and peak frequency of a QPO in the range 2 Hz–10 Hz were used as criteria for all classes, as well as the presence or absence of high-amplitude quasi-periodic flaring with a frequency between 0.01–1 Hz. The folded profile of these flares, as well as the presence of associated harmonics, were also used as classification diagnostics in observations. Additionally, the presence or absence of low count-rate ‘dips’ in a lightcurve was used as a criterion for Classes VI, VIII and IX. Detailed criteria for each individual class are given below in Sections 4.3.2 to 4.3.2.

For hardness-intensity diagrams, we describe looping behaviour with the terms ‘clockwise’ and ‘anticlockwise’; in all cases, these terms refer to the direction of a loop plotted in a

hardness-intensity diagram with colour on the x -axis and intensity on the y -axis.

In Appendix A, we present a list of all orbits used in the study along with the variability classes we assigned to them.

In Figure 4.3, we show global 2–16 keV lightcurves of IGR J17091 during the 2011-2013 outburst. In each panel, all observations of a given class are highlighted in red. A characteristic lightcurve is also presented for each class. In Figure 4.4 panel (a), we show a plot of average hardness H_{A2} against H_{A1} for each observation, showing the long-term hysteresis of the object in colour-colour space. Again, observations belonging to each variability class are highlighted. In Figure 4.4 panels (b) and (c), we show global hardness-intensity diagrams for H_{A1} and H_{A2} respectively.

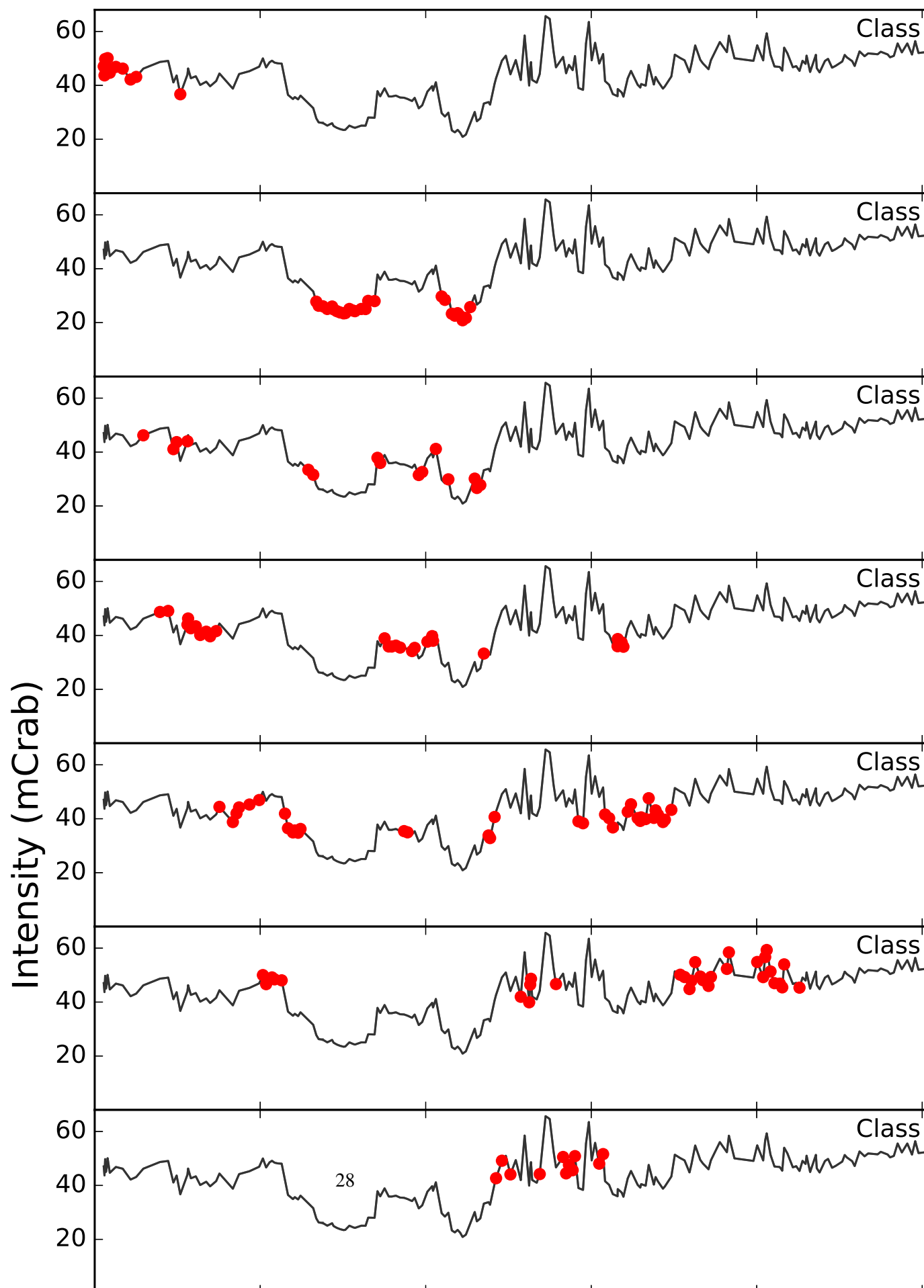
In Figure 4.4 Panel (a), we see that IGR J17091-3624 traces a two branched pattern in colour-colour space corresponding to a branch which is soft (~ 0.9) in H_{A1} and variable in H_{A2} and a branch which is soft (~ 0.5) in H_{A2} and variable in H_{A1} . The ‘soft’ HID shown in Figure 4.4 Panel (b) is dominated by a branch with a wide spread in H_{A1} and intensities between ~ 40 – 60 mCrab. A second branch exists at lower intensities, and shows an anticorrelation between intensity and H_{A1} . Finally, the ‘hard’ HID shown in Figure 4.4 Panel (c) shows an obvious anticorrelation between H_{A2} and intensity, but there is also a secondary branch between $H_{A2} \approx 0.7$ – 0.9 at a constant intensity of ~ 40 mCrab.

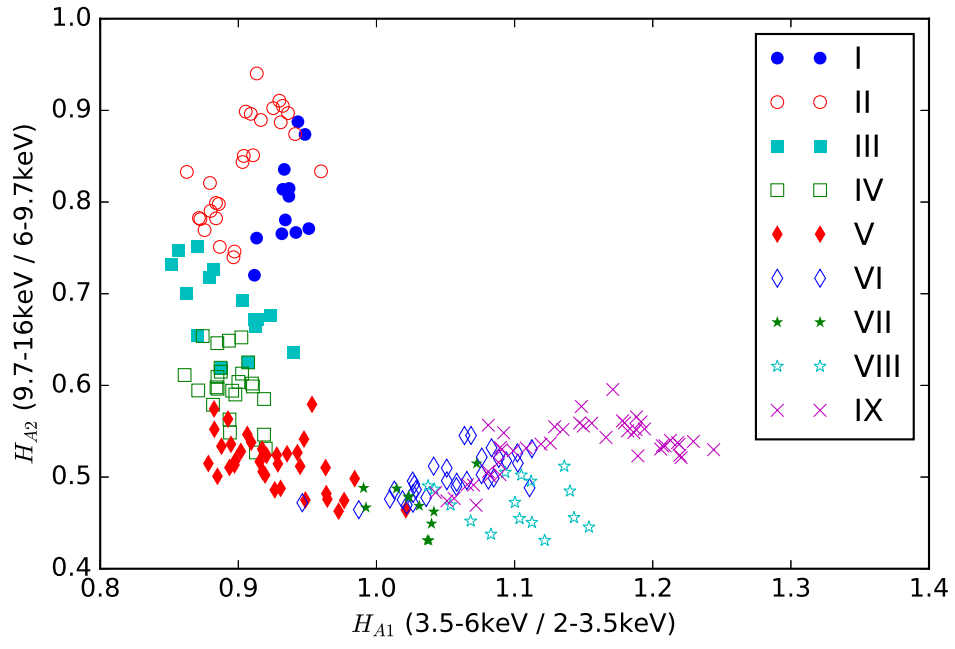
For characteristic count rates and colours in each class, we quote the upper and lower quartile values (Kenney, 1939) instead of the mean. This is due to the presence of high-amplitude but short-lived flares in many of the classes we describe. Using the upper and lower quartiles as our measure of average and distribution means that our values will be less susceptible to outlier values of count rate and colour present in these flares. All count rates have been background corrected (see Section 4.2.1).

We have obtained mean values for these count rate quartiles, as well as values for colour C_1 and fractional RMS, by calculating these values individually for each orbit. Histograms were then constructed from these datasets for each class, such that the mean and standard deviation of these values could be measured for each class. These values are presented in Table 4.2.

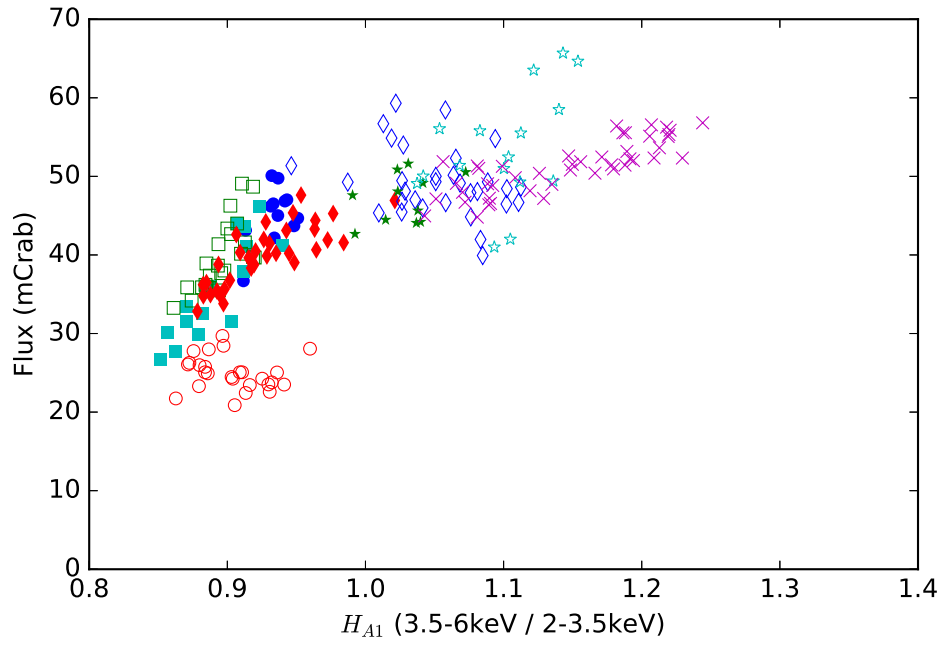
We describe QPOs in terms of their q -value; a measure of coherence defined by the ratio of peak frequency and full-width half-maximum of each QPO. We collected these values by fitting our power spectra with Lorentzians.

For each class, we present three standard data products; a 500 s lightcurve, a variable-length lightcurve where the length has been selected to best display the variability associated with the class and a Fourier PDS. Unless otherwise stated in the figure caption, the 500 s lightcurve and the Fourier PDS are presented at the same scale for all classes. In Table 4.3 we present a tally of the number of times we assigned each Variability Class to an *RXTE* orbit.

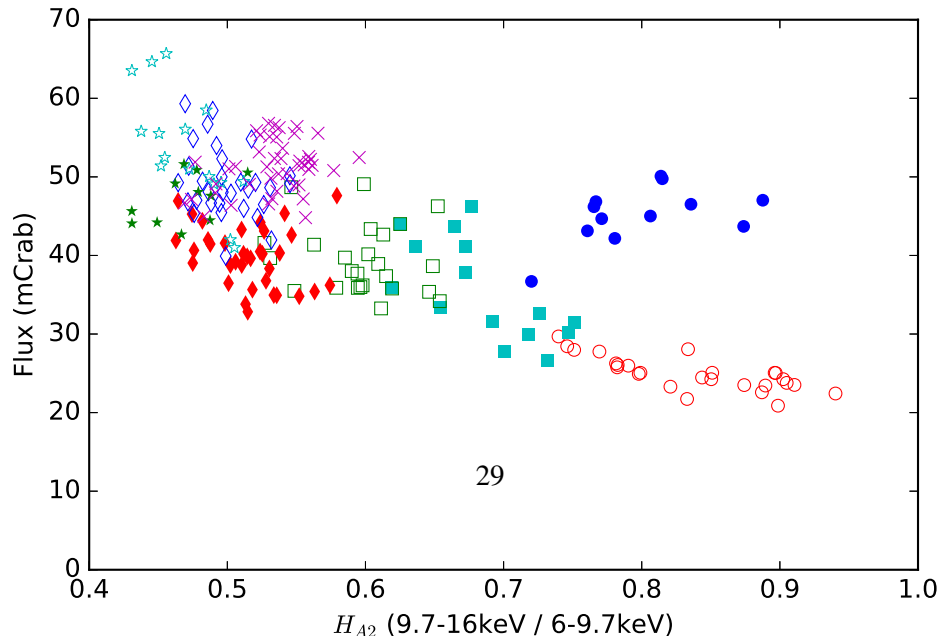




(a) Colour-Colour Diagram



(b) "Soft" (H_{A1}) Hardness-Intensity Diagram



Class	LQ Rate (cts s ⁻¹)	UQ Rate (cts s ⁻¹)	Frac. RMS	Median C ₁
I	84–108	106–132	0.13–0.19	0.4–0.68
II	43–57	59–71	0.15–0.23	0.4–0.68
III	64–84	80–110	0.17–0.23	0.35–0.45
IV	63–81	92–122	0.27–0.37	0.32–0.4
V	49–67	88–134	0.44–0.54	0.28–0.46
VI	64–98	111–155	0.29–0.47	0.33–0.61
VII	65–79	128–140	0.45–0.57	0.32–0.42
VIII	62–88	142–178	0.42–0.52	0.36–0.49
IX	87–111	114–144	0.16–0.24	0.42–0.6

Table 4.2: Lower and upper quartile count rates, fractional RMS and median colour averaged across all observations belonging to each class. Count rates and fractional RMS are taken from the full energy range of *RXTE/PCA*, and fractional RMS values are 2–60 keV taken from lightcurves binned to 0.5 s. Count rates are normalised for the number of PCUs active during each observation. All values are quoted as 1σ ranges.

Class	Orbits	Total Time (s)	Fraction
I	31	69569	14.8%
II	26	50875	10.8%
III	14	26228	5.6%
IV	31	69926	14.9%
V	35	72044	15.3%
VI	29	54171	11.5%
VII	11	19241	4.1%
VIII	16	26553	5.7%
IX	50	81037	17.3%

Table 4.3: A tally of the number of times we assigned each of our nine Variability Classes to an *RXTE* orbit. We have also calculated the amount of observation time corresponding to each class, and thus inferred the fraction of the time that IGR J17091 spent in each class. Note: the values in the Total Time column assume that each orbit only corresponds to a single variability Class.

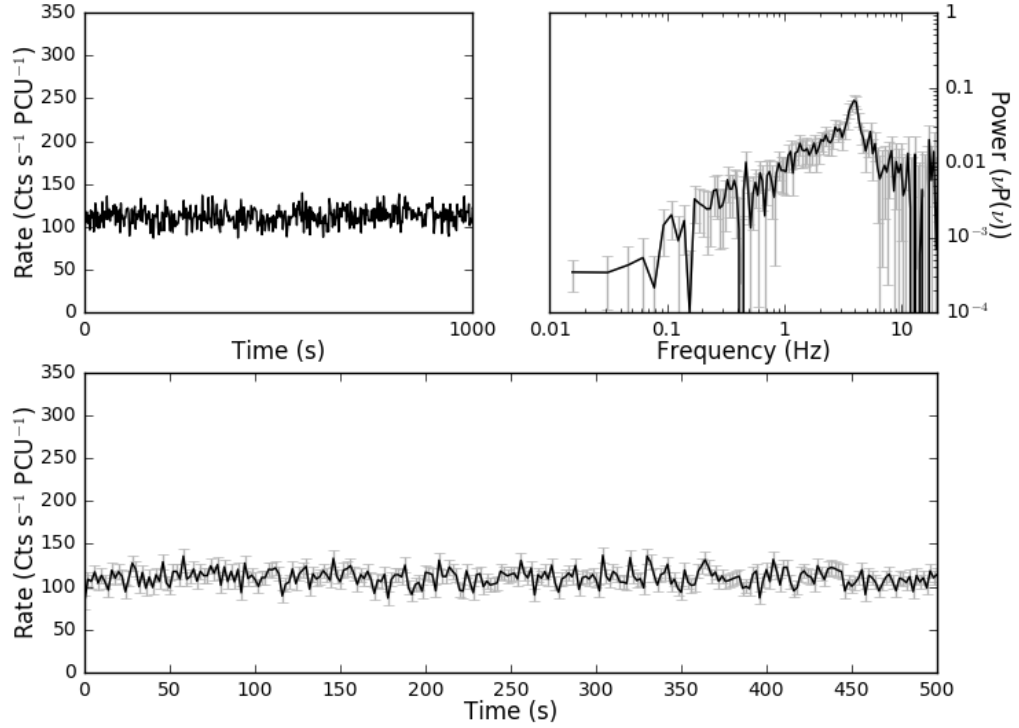


Figure 4.5: Plots of the Class I observation 96420-01-01-00, orbit 0. *Top-left:* 1000 s lightcurve binned on 2 seconds to show lightcurve evolution. *Top-right:* Fourier Power Density Spectrum. *Bottom:* 500 s lightcurve binned on 2 seconds.

Class I – Figure 4.5

In the 2 s binned lightcurve of a Class I observation, there is no structured second-to-minute scale variability. The Fourier PDS of all observations in this class shows broad band noise between ~ 1 –10 Hz, as well as a weak QPO (with a q -value of ~ 5) which peaks at around 5 Hz.

Class II – Figure 4.6

Class II observations are a factor of ~ 2 fainter in the L_T band than Class I observations. They also occupy a different branch in a plot of hardness H_{A2} against flux (see Figure 4.4c). The PDS shows no significant broad band noise above ~ 1 Hz unlike that which is seen in Class I. The ~ 5 Hz QPO seen in Class I is absent in Class II.

Class III – Figure 4.7

Unlike Classes I & II, Class III lightcurves show structured flaring, with a peak-to-peak recurrence time of 42–80 s. Most flares consist of a steady ~ 60 s rise in count rate and then

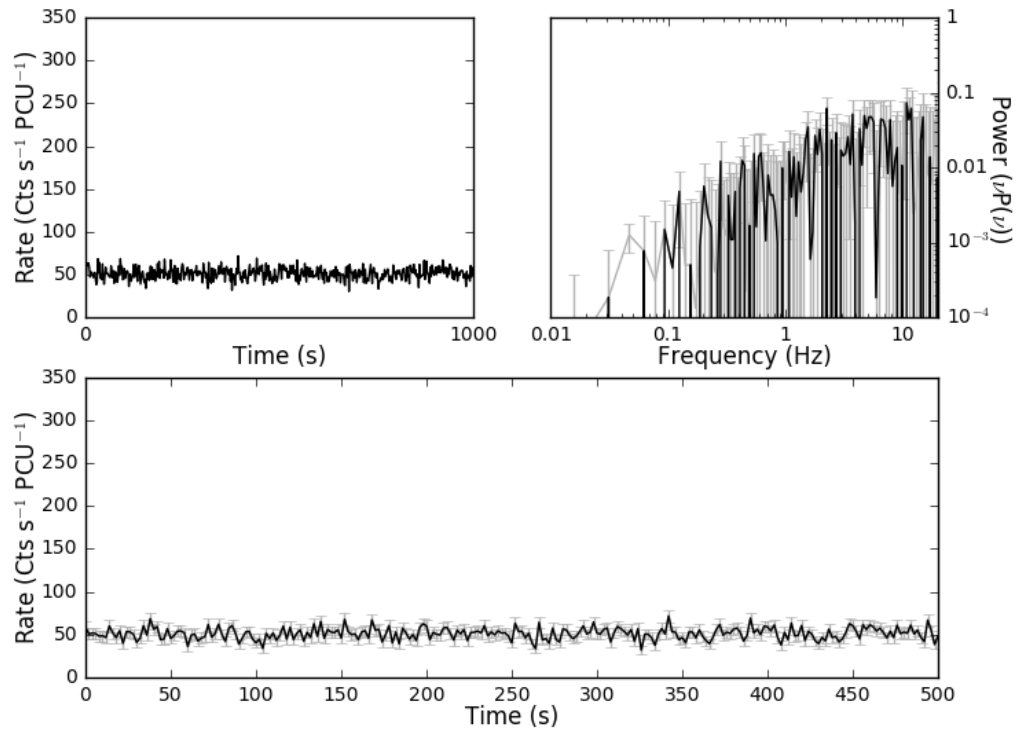


Figure 4.6: Plots of the Class II observation 96420-01-11-00, orbit 0. *Top-left:* 1000 s lightcurve binned on 2 seconds to show lightcurve evolution. *Top-right:* Fourier Power Density Spectrum. *Bottom:* Lightcurve binned on 2 seconds.

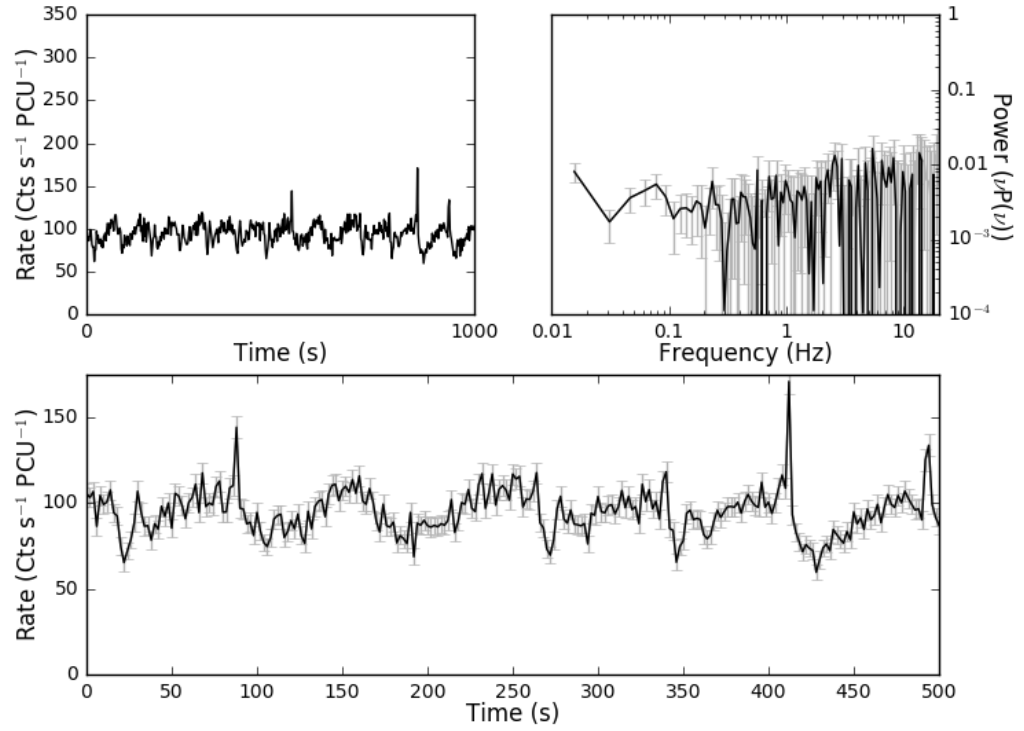


Figure 4.7: Plots of the Class III observation 96420-01-04-01, orbit 0. *Top-left:* 1000 s lightcurve binned on 2 seconds to show lightcurve evolution. *Top-right:* Fourier Power Density Spectrum. *Bottom:* Lightcurve binned on 2 seconds. Note that, to emphasise the behaviour of the lightcurve in this class, we have magnified the 500 s lightcurve y-scale by a factor of 2 compared with the lightcurves presented for other classes.

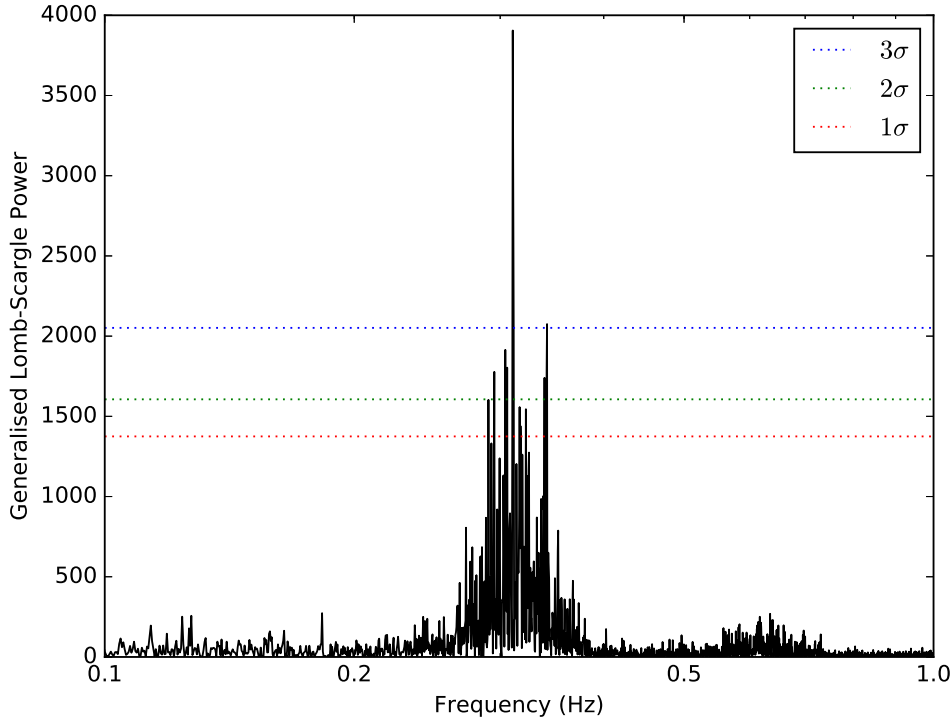


Figure 4.8: The Lomb-Scargle periodogram of observation 96420-19-01, orbit 0, with significance levels of 1, 2 and 3σ plotted. The peak at 0.31 Hz was used to define a QPO frequency when folding the data from this observation.

an additional and sudden rise to a peak count rate at $\gtrsim 200 \text{cts s}^{-1} \text{PCU}^{-1}$ which lasts for $\lesssim 0.5 \text{ s}$ before returning to continuum level (we have magnified the y-scaling in the lightcurve of Figure 4.7 to emphasise this behaviour). This sudden rise is not present in every flare; in some observations it is absent from every flare feature. No 5Hz QPO is present in the PDS and there is no significant variability in the range between $\sim 1\text{--}10\text{Hz}$.

As this class has a well-defined periodicity, we folded data in each observation to improve statistics using the best-fit period obtained from generalised Lomb-Scargle Periodogram Analysis; we show a representative Lomb-Scargle periodogram in Figure 4.8. We find an anticlockwise hysteric loop in the folded HID_1 of all 15 Class III orbits. In Figure 4.9 we show an example of one of these loops.

Class IV – Figure 4.10

The lightcurves in this class show regular variability with a peak-to-peak recurrence time of 25–39 s. We performed peak analysis (see Section 3.3.1) on observations belonging to this class, finding that each peak has a rise time with lower and upper quartile values of 19.5 and 33.5 s, a fall time with lower and upper quartile values of 4.6 and 13.5 s and a peak count rate of $159\text{--}241 \text{cts s}^{-1} \text{PCU}^{-1}$. There are no prominent significant QPOs in the Fourier

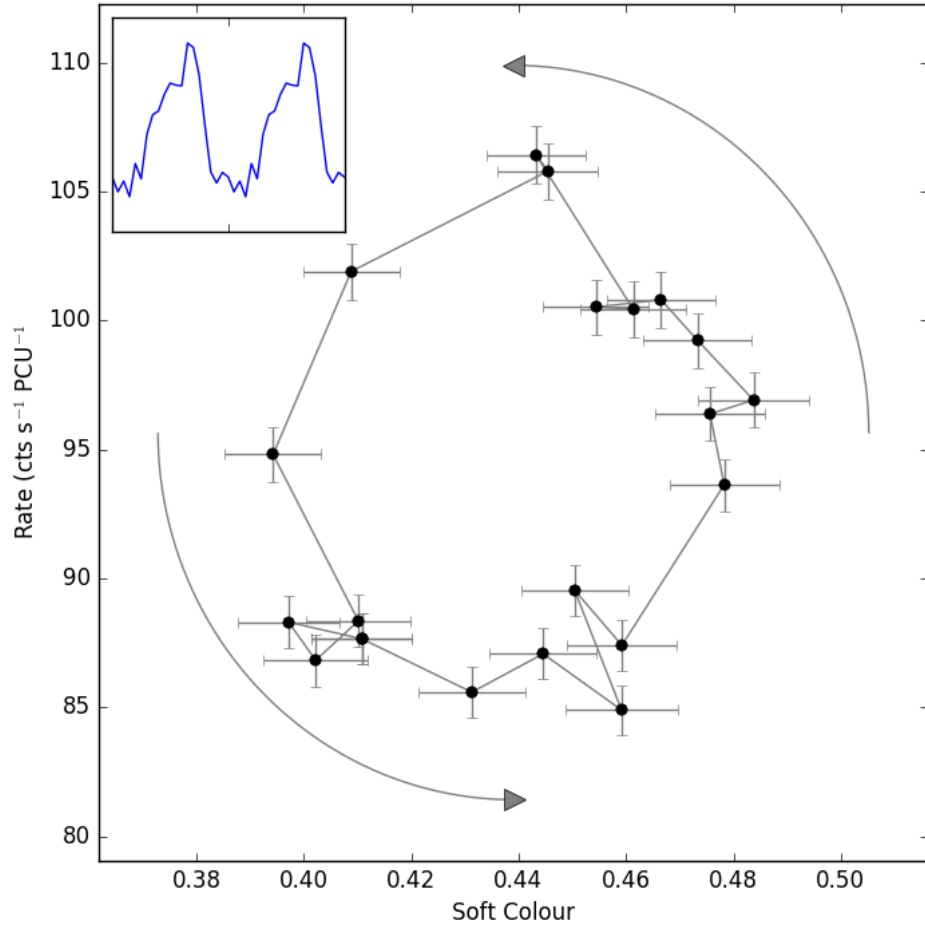


Figure 4.9: The hardness-intensity diagram (HID₁) of the Class III observation 96420-01-04-01, orbit 0. The data have been folded over a period of 79.61 s, corresponding to the peak frequency in the Lomb-Scargle spectrum of this observation. Inset is the folded lightcurve of the same data.

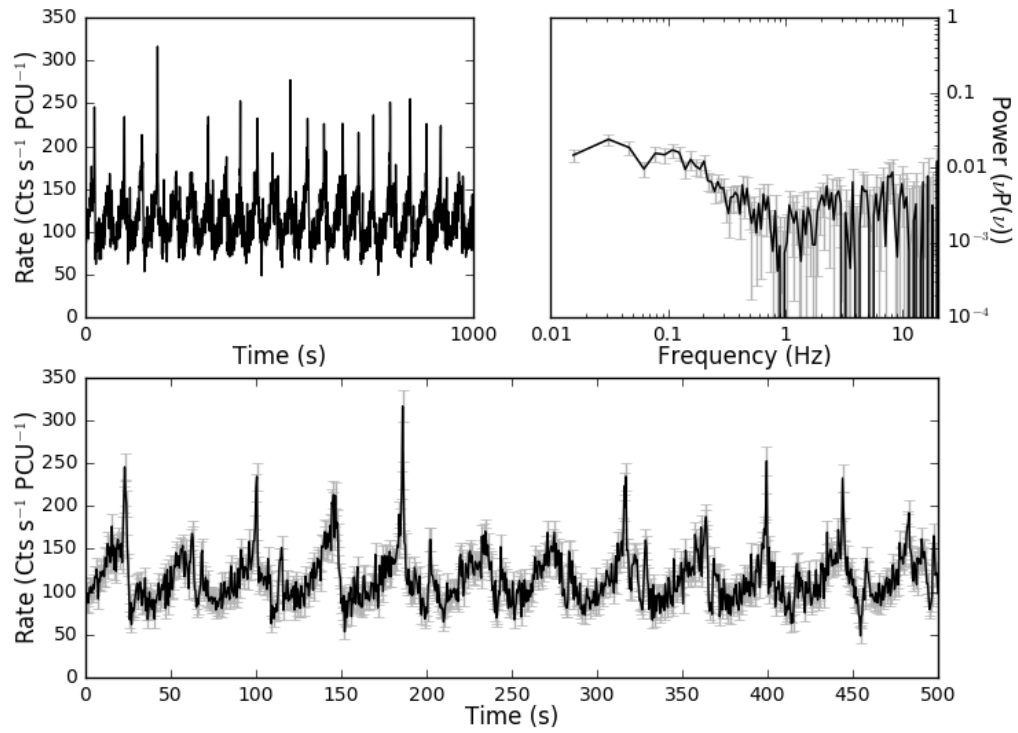


Figure 4.10: Plots of the Class IV observation 96420-01-05-00, orbit 0. *Top-left:* 1000 s lightcurve binned on 2 seconds to show lightcurve evolution. *Top-right:* Fourier Power Density Spectrum. *Bottom:* Lightcurve binned on 0.5 seconds.

PDS above $\sim 1\text{Hz}$.

We folded individual Class IV lightcurves and found anticlockwise hysteretic loops in the HID_1 of 14 out of 30 Class IV observations. In the top panel of Figure 4.11 we show an example of one of these loops. However, we also find clockwise hysteretic loops in 6 Class IV observations, and in 10 orbits the data did not allow us to ascertain the presence of a loop. We provide an example of both of these in the lower panels of Figure 4.11. We note that the structure of clockwise loops are more complex than anticlockwise loops in Class IV, consisting of several lobes⁷ rather than a single loop (Figure 4.11, bottom-left).

Compared with Class III, the oscillations in Class IV occur with a significantly lower period, with a mean peak-to-peak recurrence time of $\sim 30\text{ s}$ compared to $\sim 60\text{ s}$ in Class III.

In Figure 4.4 we show that Classes III and IV can also be distinguished by average hardness, as Class III tends to have a greater value of H_{A2} than Class IV.

Class V – Figure 4.12

The lightcurves in this class, like in Classes III and IV, show flaring behaviour, with flares separated by a few tens of seconds. At higher frequencies, the PDS shows a prominent QPO centred at $\sim 4\text{Hz}$ with a q -value of ~ 3 . There is also significant broad band noise between $\sim 0.1\text{--}1\text{Hz}$

In Figure 4.13 we show that the flaring in this class is more complex than that seen in Classes III and IV. Class V lightcurves consist of short strongly peaked symmetrical flares (hereafter Type V_1) and a longer more complex type of flare (hereafter Type V_2). The Type V_2 flare consists of a fast rise to a local maximum in count rate, followed by a $\sim 10\text{ s}$ period in which this count rate gradually reduces by $\sim 50\%$ and then a much faster peak with a maximum count rate between 1 and 2 times that of the initial peak. In both types of flare, we find that the increase in count rate corresponds with an increase in soft colour. The two-population nature of flares in Class V can also clearly be seen in Figure 4.14, where we show a two-dimensional histogram of flare peak count rate against flare duration.

We folded all individual Class V lightcurves, in each case cropping out regions of V_2 flaring. We find clockwise hysteretic loops in the HID_1 of 30 out of 33 Class V observations, suggesting a lag in the aforementioned relation between count rate and soft colour. In the upper panel Figure 4.15 we present an example of one of these loops. In one observation however, we found an anticlockwise loop in the HID_1 (shown in Figure 4.15 lower-left panel). We were unable to ascertain the presence of loops in the remaining 2 orbits; for the sake of completeness, we show one of these in the lower-right panel of Figure 4.15.

⁷In HID s with multiple lobes, the loop direction we assign to the observation corresponds to the direction of the largest lobe.

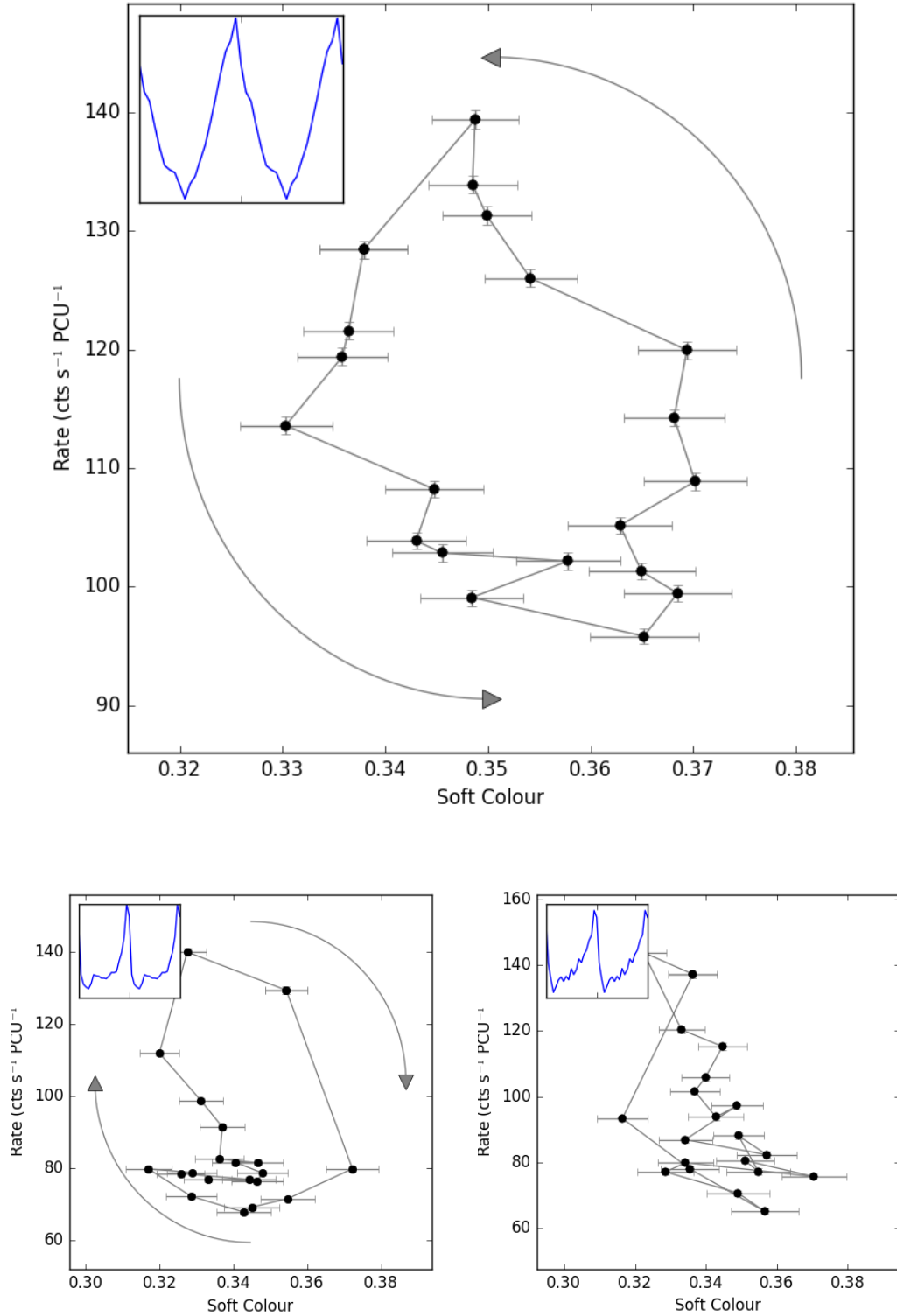


Figure 4.11: *Top:* The hardness-intensity diagram (HID₁) of the Class IV observation 96420-01-05-00, orbit 0 showing an anticlockwise loop. The data have been folded over a variable period found with the algorithm described in Section 3.3.1. Inset is the folded lightcurve of the same data. *Bottom Left:* The hardness-intensity diagram of Class IV observations 96420-01-24-02 orbit 0, an example of a clockwise loop. *Bottom Right:* The hardness-intensity diagram of Class IV observation 96420-01-06-00 orbit 0, in which we were unable to ascertain the presence of a loop.

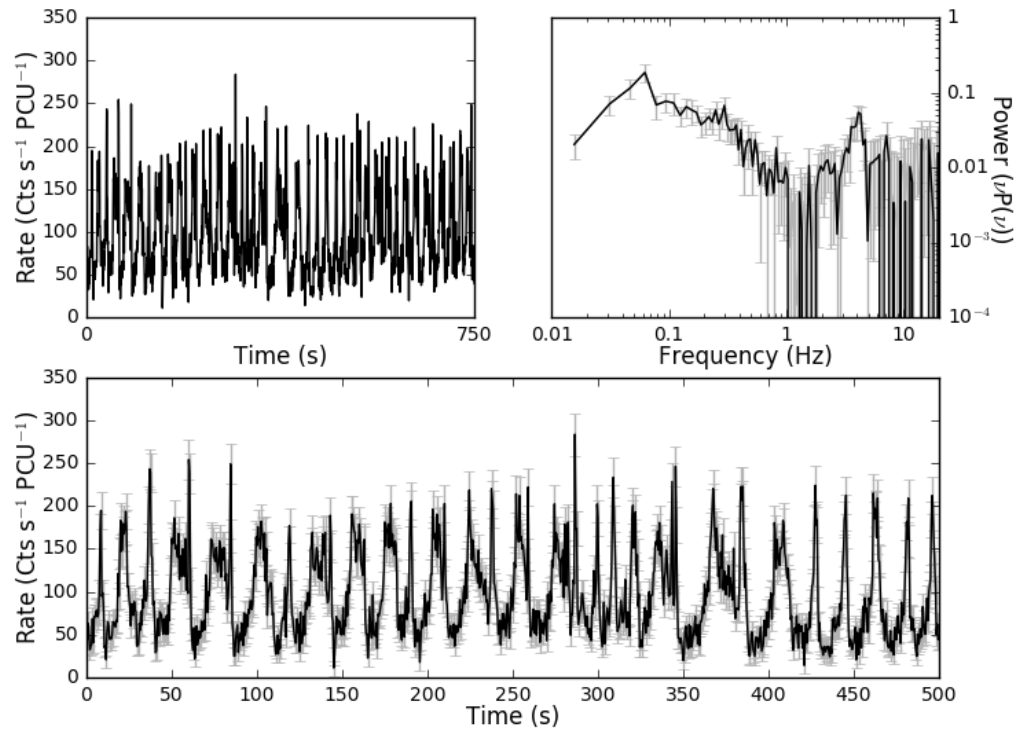


Figure 4.12: Plots of the Class V observation 96420-01-06-03, orbit 0. *Top-left:* 750 s lightcurve binned on 2 seconds to show lightcurve evolution. *Top-right:* Fourier Power Density Spectrum. *Bottom:* Lightcurve binned on 0.5 seconds.

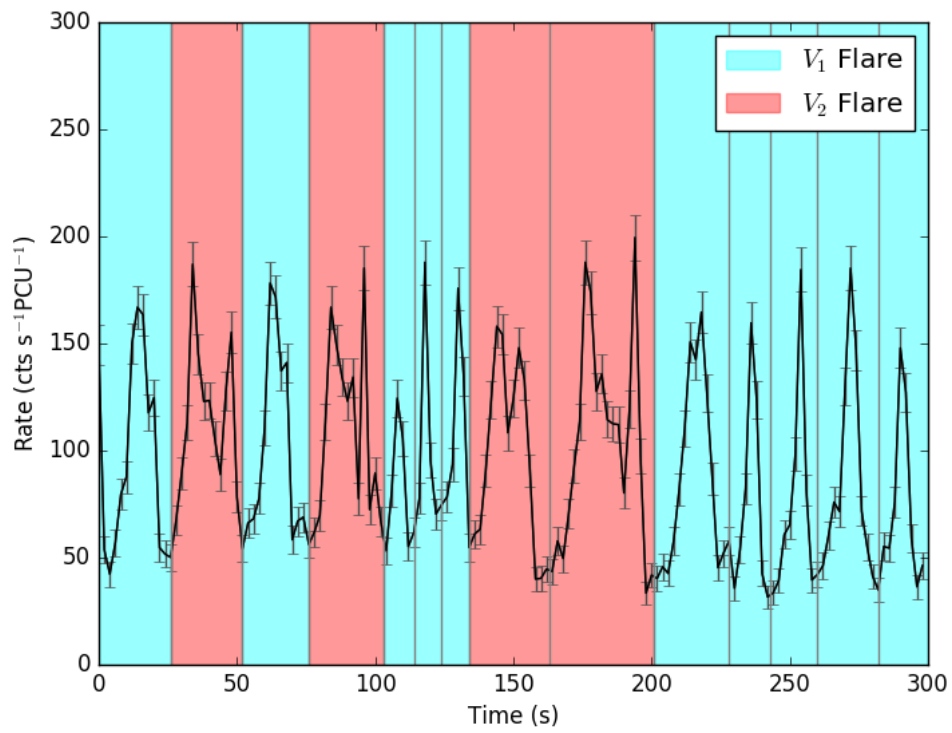


Figure 4.13: A portion of the lightcurve of observation 96420-01-06-03, orbit 0, showing Type V_1 flares (highlighted in cyan) and Type V_2 flares (highlighted in red).

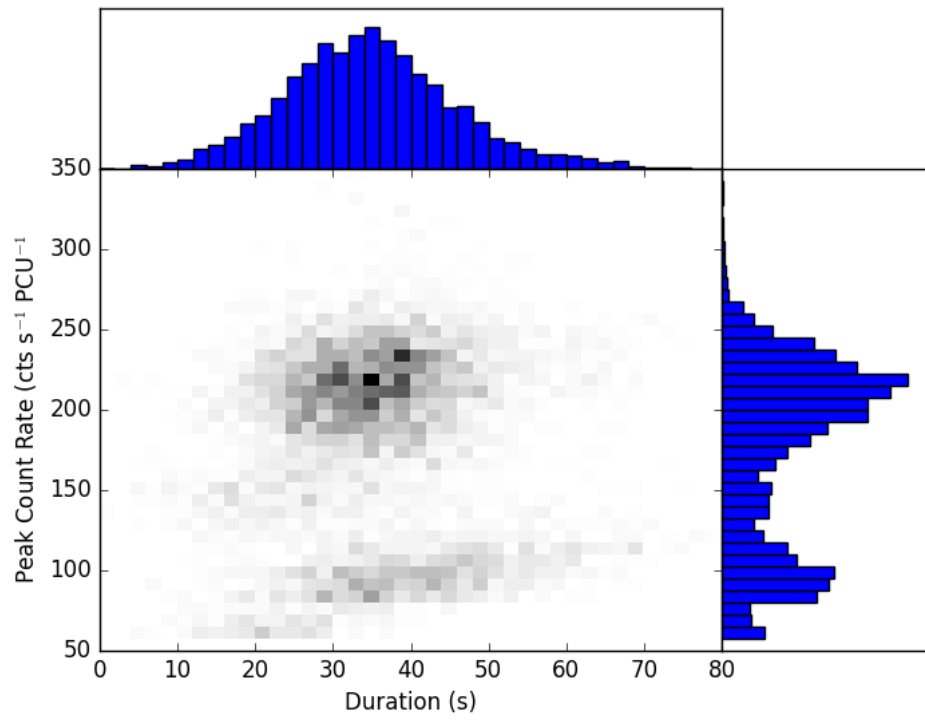


Figure 4.14: Every flare in all observations identified as Class V, plotted in a two-dimensional histogram of flare peak count rate against flare duration to show the two-population nature of these events.

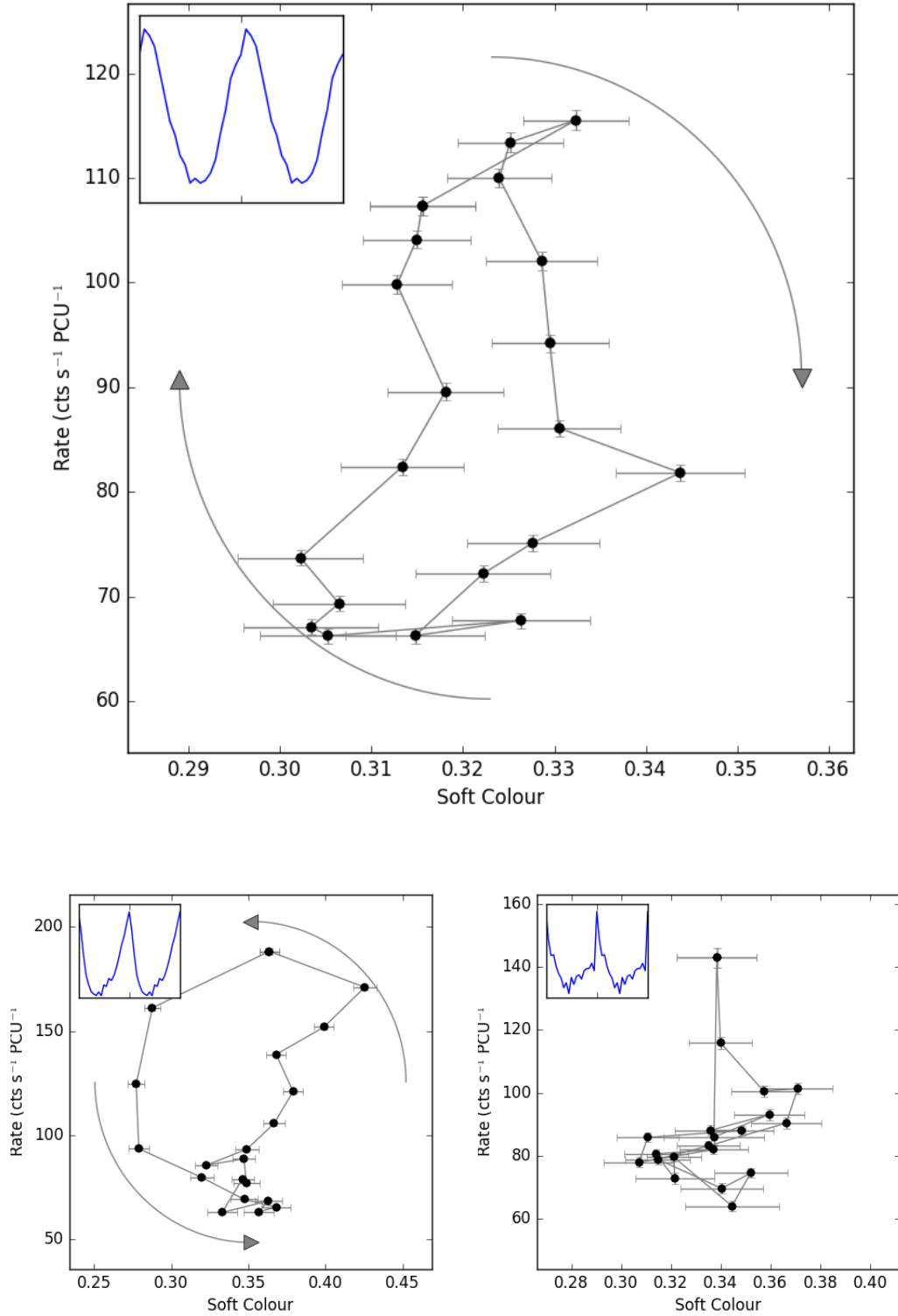


Figure 4.15: *Top:* The hardness-intensity diagram (HID₁) of a type V₁ flaring region in Class V observation 96420-01-07-00, orbit 0 showing a clockwise loop. The data have been folded over a variable period found with the algorithm described in Section 3.3.1. Inset is the folded lightcurve of the same data. *Bottom Left:* The hardness-intensity diagram of Class V observation 96420-01-25-05 orbit 0, an example of an anticlockwise loop. *Bottom Right:* The hardness-intensity diagram of Class V observation 96420-01-25-06 orbit 0, in which we were unable to ascertain the presence of a loop.

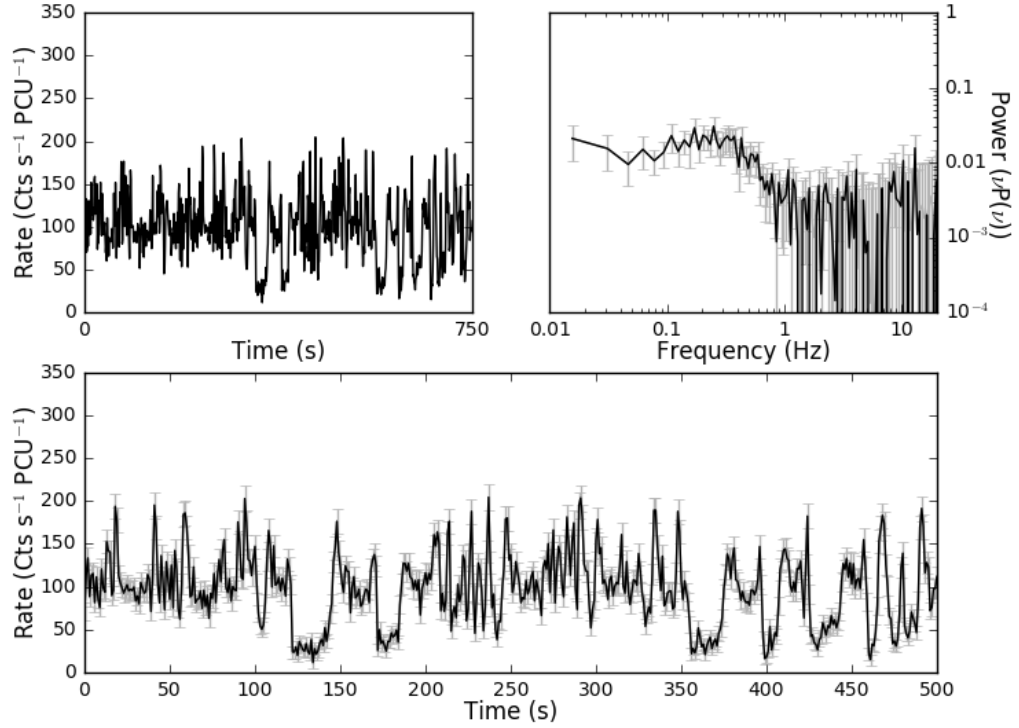


Figure 4.16: Plots of the Class VI observation 96420-01-09-00, orbit 0. *Top-left:* 750 s lightcurve binned on 2 seconds to show lightcurve evolution. *Top-right:* Fourier Power Density Spectrum. *Bottom:* Lightcurve binned on 1 second.

Class VI – Figure 4.16

The lightcurves of observations of this class show large dips in count rate; this can be seen in Figure 4.16 at, for example, $t \approx 125\text{--}150\text{ s}$. These dips vary widely in duration, from ~ 5 to ~ 50 seconds, and the count rate in both L_A and L_B fall to a level consistent with background. The dips' rise and fall times are fast, both lasting no longer than a second. They do not appear to occur with any regular periodicity.

Aside from the dips, Class VI observations show other structures in their lightcurves. Large fluctuations in count rate, by factors of $\lesssim 3$, occur on timescales of $\sim 1\text{--}5\text{ s}$; no periodicity in these oscillations could be found. This behaviour is reflected in the PDS, which shows high-amplitude broad band noise below $\sim 0.5\text{ Hz}$ with RMS-normalized power (Belloni and Hasinger, 1990) of up to $\sim 1.1\text{ Hz}^{-1}$. As can be seen in Figure 4.16, this feature takes the form of a broad shoulder of noise which shows a either weak peak or no clear peak at all. The $\sim 5\text{ Hz}$ QPO seen in the PDS of other classes is not present in Class VI observations.

We attempted to fold all individual Class VI lightcurves, ignoring the sections of data corresponding to the large count rate dips described above. In general, folding lightcurves belonging to this class is difficult; many orbits showed low-amplitude oscillations which were difficult to fold using our flare-finding algorithm (see Section 3.3.1), while many

others only showed oscillatory behaviour for a small number of periods between each pair of dips. As such, we only successfully folded 23 of the 40 Class VI orbits. Of these, 19 showed clockwise loops in the HID_1 (top panel, Figure 4.17), 3 showed anticlockwise loops (bottom-left panel, Figure 4.17). In the remaining 1 observation, the data did not allow us to ascertain the presence of loops (bottom-right panel, Figure 4.17).

Like in Class VI, we note that the clockwise loops in Class VI appear more complex than clockwise loops. Again, the clockwise loop shown in Figure 4.17 appears to have a 2-lobe structure; this is repeated in all clockwise loops found in this class.

Class VII – Figure 4.18

Class VII shows high-amplitude flaring behaviour with a peak-to-peak recurrence time of 6–12 s. In Figure 4.19 we show a dynamical Lomb-Scargle spectrogram of a Class VII observation, showing that the fast flaring behaviour has a frequency which moves substantially over time. This in turn accounts for the large spread in the value of the flare peak-to-peak recurrence time.

In Figure 4.19 we show that the peak frequency of the QPO also varies in a structured way. We also suggest that the variability of the frequency is itself a QPO with a period of ~ 150 .

At higher frequencies, the PDS shows a weak QPOs centred at ~ 8 Hz, with a q -values of ~ 2 .

We used our flare-finding algorithm (see Section 3.3.1) to perform variable-frequency folding of Class VII orbits. We find clockwise loops in 9 out of 11 Class VII orbits. In the remaining two observations, the oscillations were extremely fast. As a result, the errors in the HID_1 of these two observations were too large to successfully select peaks, and we are unable to confirm or reject the presence of loops.

Class VIII – Figure 4.20

The lightcurve of this variability class shows the dipping behaviour seen in Class VI, as can be seen in Figure 4.20 at $t \approx 125$ –150 s. The dips are less frequent than in Class VI. The behaviour outside of the dips is dominated by highly structured high-amplitude oscillations consisting of flares with a peak to peak separation of 3.4 ± 1.0 s. The PDS shows this behaviour as a very significant (q -value > 20) QPO; two harmonics of this QPO are also visible. The PDS also shows a strong (q -value = 4.7) QPO at ~ 9 Hz.

We attempted to fold Class VIII lightcurves, ignoring the portions of data corresponding to dips, using our flare-finding algorithm. The high frequency of the dominant oscillation in Class VIII resulted in large errors in the peak times of individual flares, which translated to large errors in all HID_1 s; however, we were able to ascertain the presence in loops in 8 out of 16 orbits. All 8 of these loops are clockwise.

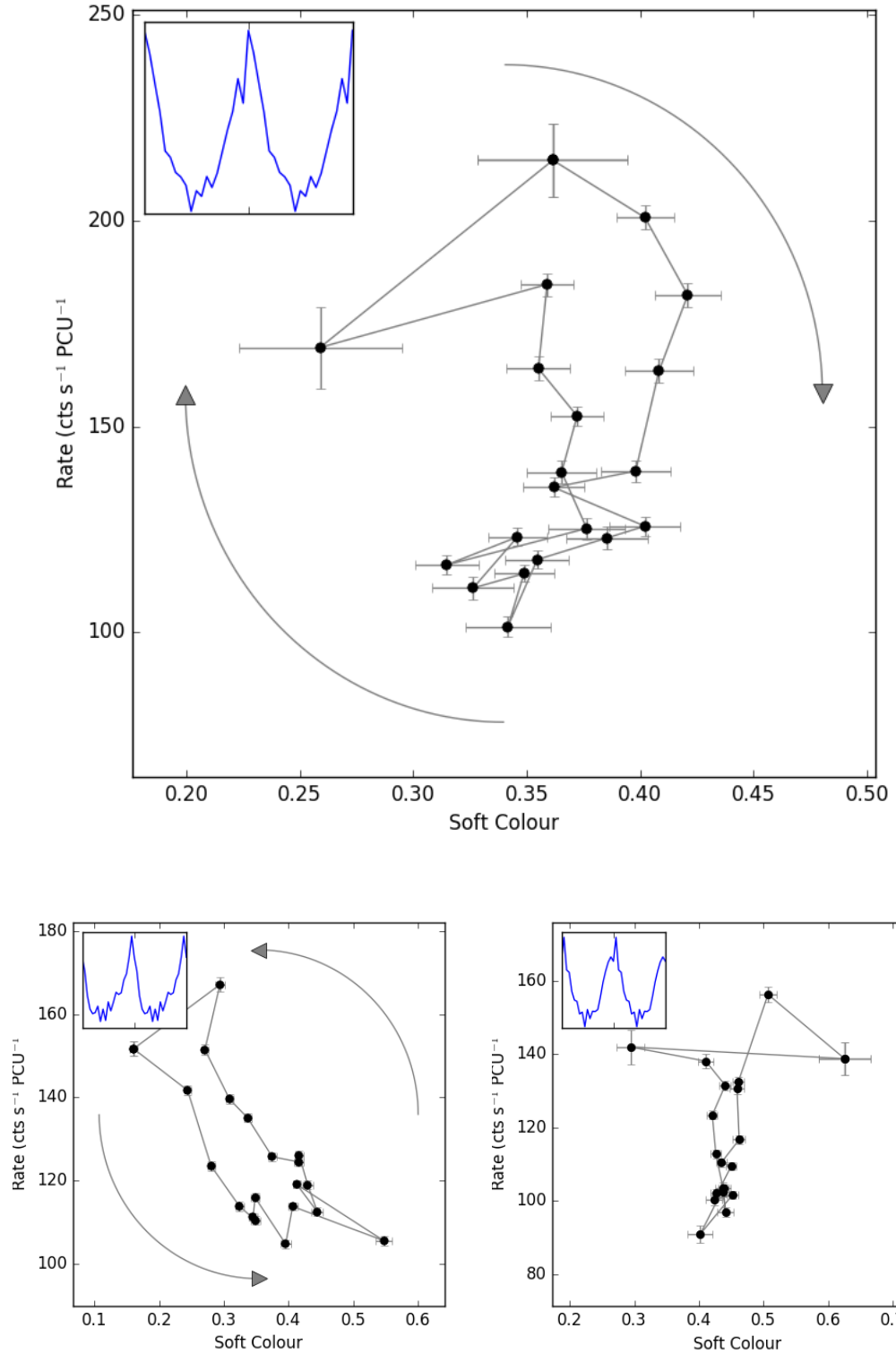


Figure 4.17: *Top:* The hardness-intensity diagram (HID₁) of the Class VI observation 96420-01-30-03, orbit 0 showing a clockwise loop. The data have been folded over a variable period found with the algorithm described in Section 3.3.1. Inset is the folded lightcurve of the same data. *Bottom Left:* The hardness-intensity diagram of Class VI observation 96420-01-30-04 orbit 0, an example of an anticlockwise loop. *Bottom Right:* The hardness-intensity diagram of Class VI observation 96420-01-09-03 orbit 0, in which we were unable to ascertain the presence of a loop.

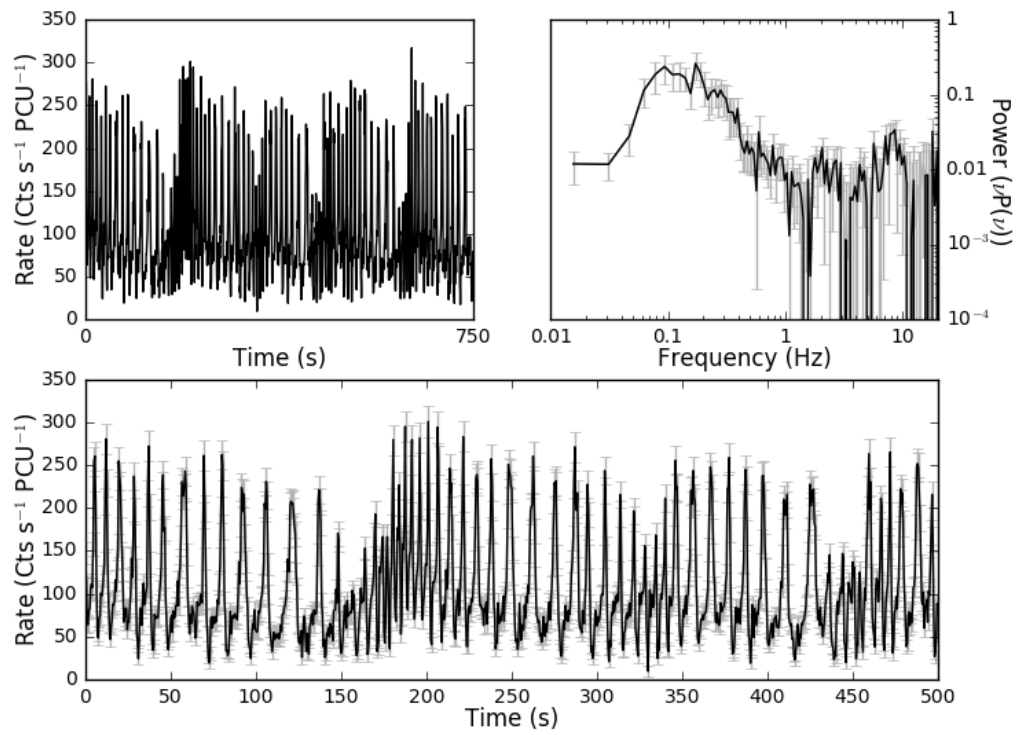


Figure 4.18: Plots of the Class VII observation 96420-01-18-05, orbit 0. *Top-left:* 750 s lightcurve binned on 2 seconds to show lightcurve evolution. *Top-right:* Fourier Power Density Spectrum. *Bottom:* Lightcurve binned on 0.5 seconds.

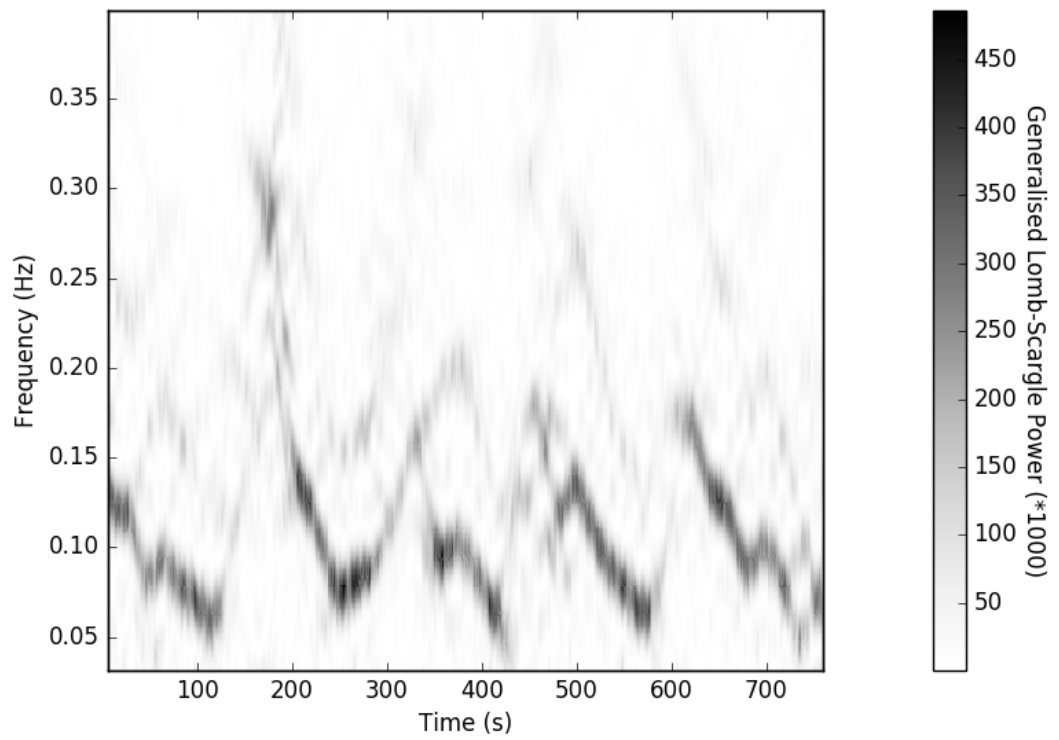


Figure 4.19: A sliding window Lomb-Scargle spectrogram of Class VII observation 96420-01-18-05, showing power density spectra from an overlapping 32 s window moved 1 s at a time. The peak frequency of this low frequency QPO itself appears to oscillate with a frequency of ~ 5 mHz.

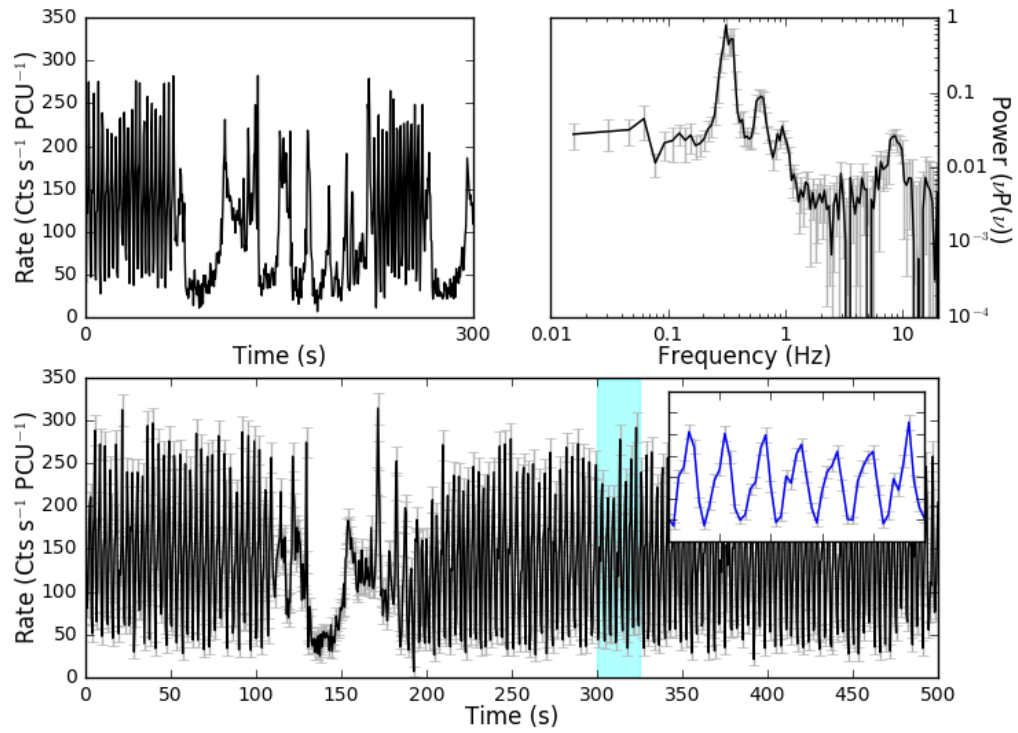


Figure 4.20: Plots of the Class VIII observation 96420-01-19-03, orbit 0. *Top-left:* 300 s lightcurve binned on 2 seconds to show lightcurve evolution. *Top-right:* Fourier Power Density Spectrum. *Bottom:* Lightcurve binned on 0.5 seconds. Inset is a zoom of the 25 s portion of the lightcurve highlighted in cyan, to show the second-scale structure in the lightcurve.

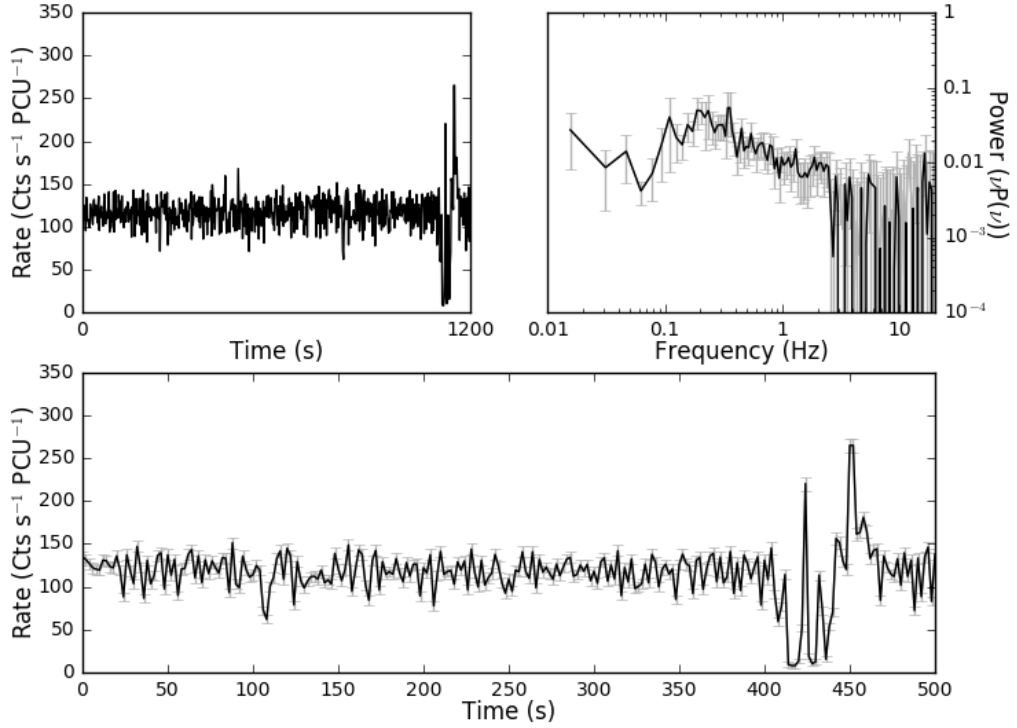


Figure 4.21: Plots of the Class IX observation 96420-01-35-02, orbit 1. *Top-left:* 1200 s lightcurve binned on 2 seconds to show lightcurve evolution. *Top-right:* Fourier Power Density Spectrum. *Bottom:* Lightcurve binned on 2 seconds.

Class IX – Figure 4.21

The 1 s lightcurve of a Class IX observation is superficially similar to the lightcurve of a Class I observation, with little obvious structured variability at timescales larger than 2 s; however, large count rate dips like those seen in Classes VI and VIII (e.g. the feature at $t \approx 410$ s in the lightcurve of Figure 4.21) are very occasionally observed. These dips may in turn be coupled to short second-scale flares in which count rate briefly increases by a factor of 2–3.

Outside of these dips and flares, the lightcurve of a Class IX observation is indistinguishable from the lightcurve of a Class I or Class II observation. However, in Figure 4.4, we show that Class IX occupies a very different part of the global H_{A2}/H_{A1} colour-colour diagram. Class IX observations show a significantly larger H_{A2} than Class I and II observations, but a significantly lower H_{A1} .

The PDS reveals significant broad band noise peaked at ~ 0.3 Hz, and the ~ 5 Hz QPO seen in other classes is absent. Altamirano and Belloni (2012) discovered high frequency (~ 66 Hz) QPOs in observations corresponding to this variability class.

Energy (keV)	Intensity (cts/s)	Significance σ	Exposure (ks)	Flux (mCrab)	Flux (10^{-10} ergs s $^{-1}$ cm $^{-2}$)
20–40	12.39 \pm 0.05	247	115	93.5 \pm 0.38	7.08 \pm 0.03
40–100	7.06 \pm 0.05	157	163	83.5 \pm 0.60	7.87 \pm 0.06
100–150	1.05 \pm 0.03	40	173	66.9 \pm 1.91	2.14 \pm 0.06
150–300	0.23 \pm 0.03	7.6	179	46.6 \pm 5.96	2.24 \pm 0.29

Table 4.4: Results from the IBIS/ISGRI analysis of the 2011–2013 Outburst of IGR J17091. The 20–40 keV flux is given in units of mCrab and (10^{-11} ergs s $^{-1}$ cm $^{-2}$). Conversion between counts and mCrab was obtained using an observation of the Crab taken during Revolution 1597 between MJD 57305.334 and 57305.894 and the conversion factors of Bird et al. (2016) and Bazzano et al. (2006).

4.3.3 Swift

Observations with *Swift* took place throughout the 2011–2013 outburst of IGR J17091–3624. Between MJDs 55622 and 55880, 17 *Swift/XRT* were at least partly simultaneous with an *RXTE* observation, corresponding to at least one observation of all 9 classes. In each case, the *Swift* and *RXTE* lightcurves were similar. The remainder of the *Swift/XRT* observations during this time were also consistent with belonging to one of our nine classes. Given that the *RXTE* data have higher count rate and time resolution, we do not further discuss the *Swift* observations taken before MJD 55880. A more detailed comparison of *RXTE* and *Swift* data is beyond the scope of this paper.

Between MJD 55952 and 56445, *Swift* observations showed IGR J17091–3624 decreasing in flux. For all observations longer than 500 s, we rebinned the lightcurves to 10 s and calculated the RMS. We find the lower and upper quartiles of the fractional RMS in these measurements to be 18.3% and 21.7% respectively. *INTEGRAL* observations taken as part of a scan programme of the Galactic Plane (Fiocchi et al., 2012) and reported by Drave et al. (2012) suggest that IGR J17091–3624 returned to the hard state between MJDs 55952 and 55989. Therefore these observations sample IGR J17091–3624 the hard state.

4.3.4 INTEGRAL

The results of the *INTEGRAL*/IBIS analysis are presented in Table 4.4. We see clear detections of IGR J17091–3624 in all energy bands during the hardest period (MJD 55575–55625) of the 2011–2013 outburst. Conversion from detected counts to flux was achieved using an *INTEGRAL*/IBIS observation of the Crab taken between MJD 57305.334 and 57305.894. Conversion from Crab units to standard flux units was obtained by conversion factors listed in Bird et al. (2016) and Bazzano et al. (2006).

Comparing these results with those of Bazzano et al. (2006), we see that IGR J17091 is detected for the first time above 150 keV with a detection significance of 7.6σ , corresponding to a flux of $2.24 \pm 0.29 \times 10^{-10}$ ergs s $^{-1}$ cm $^{-2}$ (Figure 4.22).

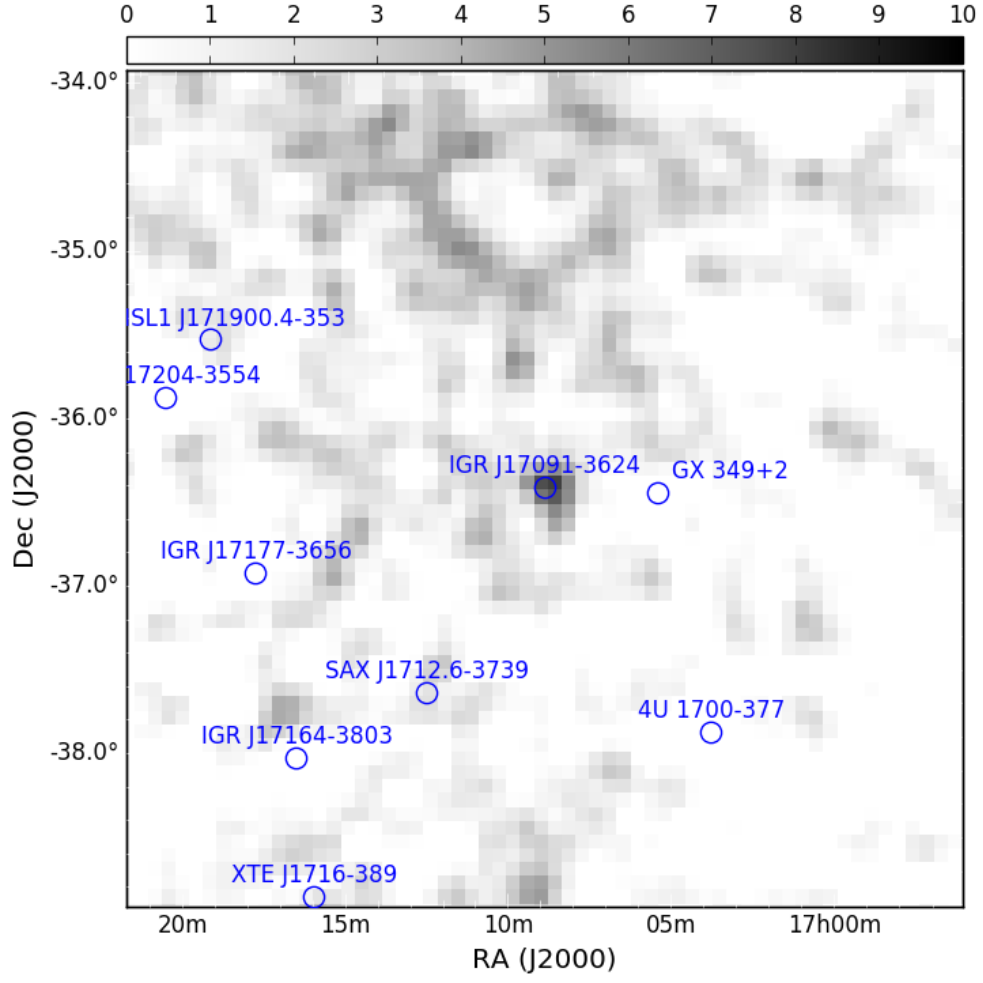


Figure 4.22: *INTEGRAL*/ISGRI 150–300 keV significance map of a 2° region centred on the position of IGR J17091-3624, showing the first significant detection of this source above 150 keV. The detection significance is 7.6σ .

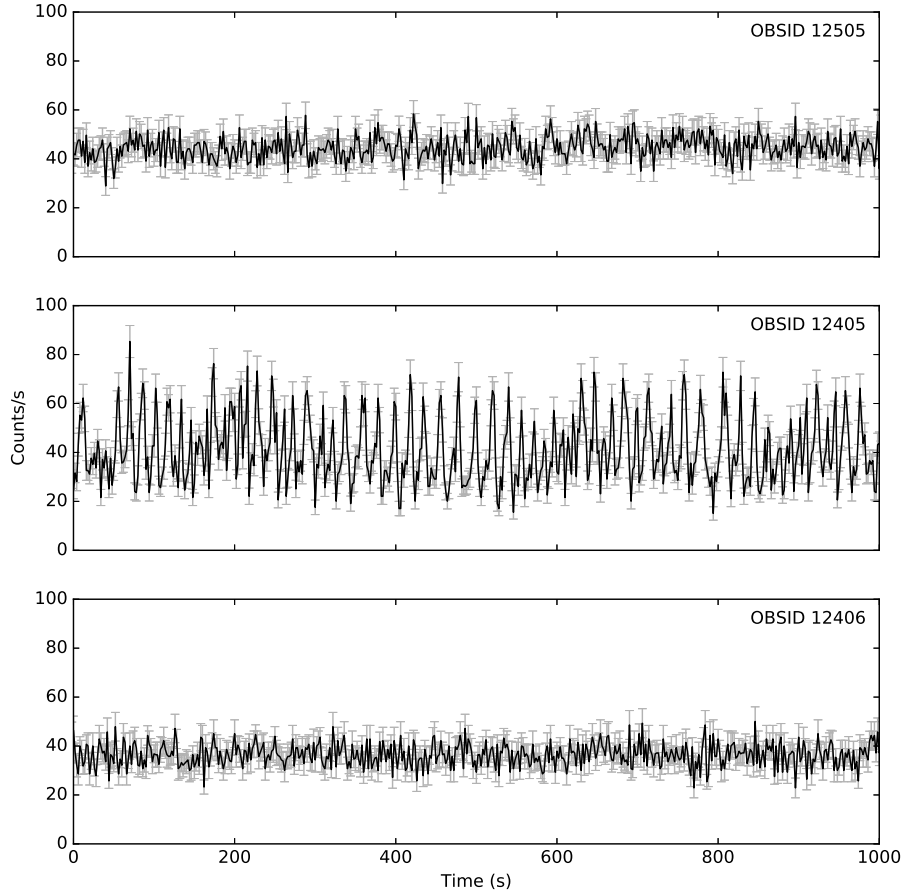


Figure 4.23: 1 ks segments of lightcurves taken from *Chandra* observations 12505, 12405 and 12406, showing Class I, Class VII and Class IX variability respectively. The lightcurve presented for observation 12505 is for the energy range 0.06-10 keV, while the other two lightcurves are for the energy range 0.5-10 keV. All three lightcurves are binned to 0.5 s.

4.3.5 Chandra

In Figure 4.23, we present lightcurves from the three *Chandra* observations considered in this paper (see also Table 4.1 for details of these observations).

Observation 12505 was performed within 24 hours of *RXTE* observation 96420-01-02-01, which showed Class I variability. No structured variability is seen in the lightcurve of OBSID 12505 (Figure 4.23, upper panel), which is consistent with Class I. Note that we consider the energy range 0.06-10 keV for this observation but 0.5-10 keV for observations 12405 and 12406.

Observation 12405 was performed within 24 hours of *RXTE* observation 96420-01-23-03, which showed Class V variability. The two observations were not simultaneous; OBSID 12405 began ~ 8.4 ks after OBSID 96420-01-2303 finished. The lightcurve of *Chandra*

OBSID 12405 (shown in Figure 4.23, middle panel) shows a mean count rate of 41 cts s^{-1} . The lightcurve shows fast flaring behaviour (with a recurrence time on the order of 10s of seconds) in which the frequency changes widely on timescales of $\sim 1000 \text{ s}$. This observation strongly resembles a Class VII lightcurve, but with its characteristic timescales increased by a factor of ~ 4 . This leads to the possibility that the low number of Class VII *RXTE* observations we identify is due to a selection effect; we would not have been able to see this observation's long-term Class VII-like behaviour if the observation had been shorter than $\sim 2 \text{ ks}$.

Observation 12406 was performed within 24 hours of *RXTE* observation 96420-01-32-06, which showed Class IX variability. The lightcurve presented for *Chandra* OBSID 12406 shows a mean count rate (36 cts s^{-1}), which is consistent with IGR J17091 being harder in this observation than in Observation 12505. This, combined with the lack of variability seen in its lightcurve, suggests that Observation 12505 is consistent with Class IX.

4.3.6 XMM-Newton

In Figure 4.24 we show lightcurves from two *XMM-Newton* observations. The lightcurve of *XMM-Newton* observation 0677980201, shown in the upper panel of Figure 4.24, shows the regular flares characteristic of Class IV variability. A simultaneous *RXTE* observation (OBSID 96420-01-05-000) also showed Class IV variability.

XMM-Newton observation 070038130, shown in the lower panel of Figure 4.24, was made after the end of *RXTE* observations IGR J17091-3624. As such it cannot be compared with contemporaneous *RXTE* data. The 5 s binned lightcurve shows no apparent variability, but a Fourier PDS of the observation (shown in Figure 4.25) reveals a QPO centred at around $\sim 0.15 \text{ Hz}$ and a broad band noise component at lower frequencies. Drave et al. (2012) reported that IGR J17091 transited to the hard state in February 2012, seven months before this observation was taken. As such, we find that observation 0677980201 samples the hard state in IGR J17091 and is thus beyond the scope of our set of variability classes.

4.3.7 Suzaku

The two *Suzaku* observations of IGR J17091-3624 considered, OBSIDs 407037010 and 407037020, were performed during the 2nd and 3rd re-flares of the hard state phase of the 2011–2013 outburst. OBSID 407037010 was taken simultaneously with *XMM-Newton* observation 0700381301. The XIS 0 count rates are 7.8 cts s^{-1} and 2.5 cts s^{-1} respectively.

Neither lightcurve shows ‘heartbeats’ or any other type of GRS 1915-like variability. However, we find evidence of a low frequency QPO feature at $\sim 0.15 \text{ Hz}$ in the OBSID 407037010; this QPO is also seen in *XMM-Newton* observation 0700381301 (Figure 4.25). The presence of a QPO below 1 Hz and flat-topped power density spectrum confirm that IGR J17091 was in the hard state at this time.

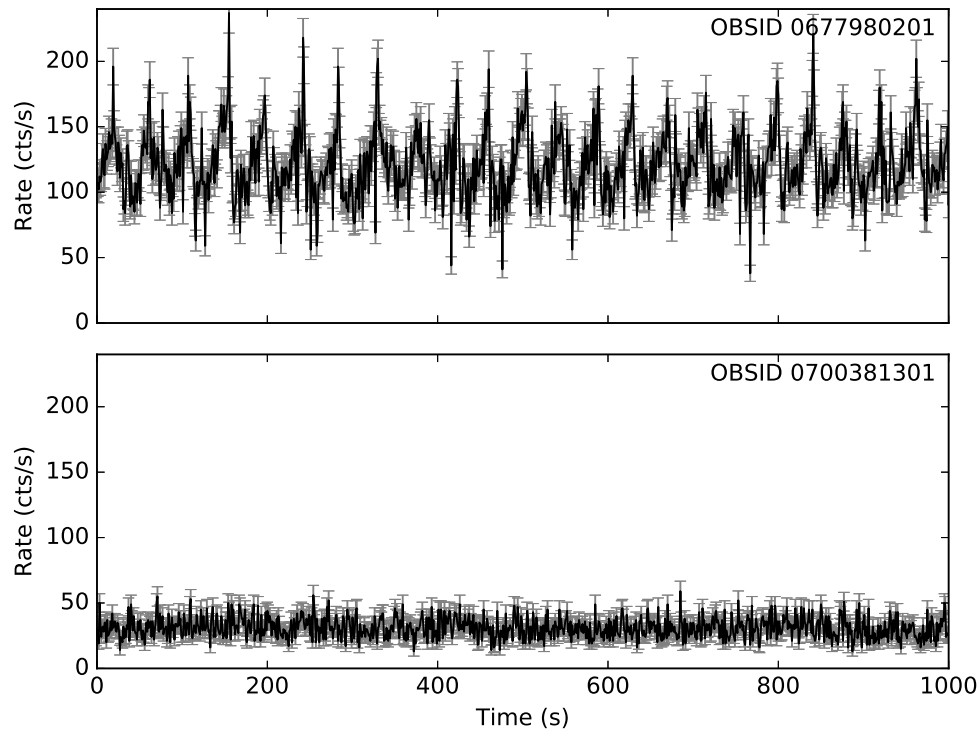


Figure 4.24: Lightcurves of *XMM-Newton* observations 0677980201 and 0700381301, showing Class IV variability and the hard state respectively. Both lightcurves binned to 2 s. Data for observation 0677980201 is taken from *EPIC-MOS2* and data for observation 0700381301 is taken from *EPIC-pn*.

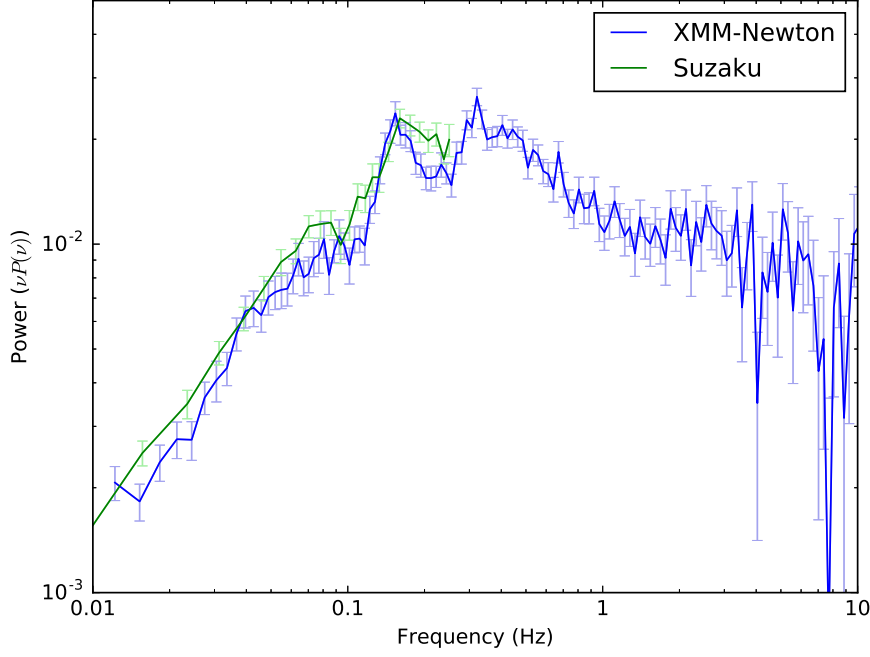


Figure 4.25: $\nu P(\nu)$ -normalised co-added power density spectra of *XMM-Newton* observation 0700381301 and *Suzaku* observation 407037010. Both observations were taken simultaneously on September 29 2012 (MJD 56199). We sample observation 0700381301 up to a frequency of 10 Hz, while the 2 s time resolution of observation 407037010 results in a Nyquist frequency of 0.25 Hz.

4.4 Discussion

Using observations from *XMM-Newton*, *RXTE* and *Chandra*, we describe the complex variability seen in IGR J17091 as a set of nine variability ‘classes’, labelled I to IX. These classes are distinguished from each other by values of upper and lower quartile (i.e. 25th and 75th percentile) count rates, mean RMS, the presence of QPOs in Fourier PDS, the shape of flare and dip features in the lightcurve and the presence of loops in the 6–16/2–6 keV hardness-intensity diagram HID_1 . See Section 4.3 for a full description of these classes.

The classification of some observations is clearer than others. Some orbits were too short to definitively quantify the behaviour of the source, whereas some other orbits contain a transition between two classes. An example lightcurve showing a transition from Class III to Class IV is presented in Figure 4.26.

Our set of classes is analogous to, but not based upon, the set of variability classes defined by Belloni et al. 2000 to describe the behaviour of the similarly complex LMXB GRS 1915. This ensures that our set of classes is not biased by an *a priori* assumption that the two objects are similar. However if we do assume that wide range of variability seen in these two objects are driven by the same physical processes, a direct comparison between the variability classes in the two systems can further our understanding of the physics that drive these exotic objects.

We also use all 2011–2013 IGR J17091–3624 data from *RXTE*, *XMM-Newton*, *Chandra*,

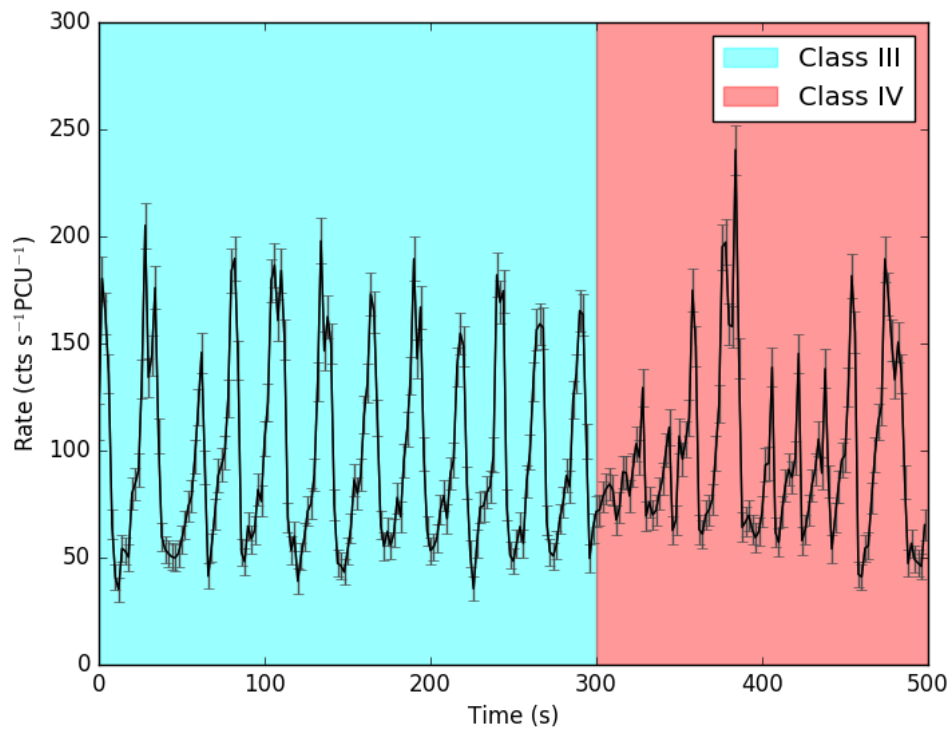


Figure 4.26: A lightcurve of observation 96420-01-06-02, orbit 0, showing a transition in behaviour between Class IV (in cyan, see Section 4.3.2) and Class V (in red, see Section 4.3.2).

Table 4.5: The nine variability classes of IGR J17091-3624, showing the name of the closest corresponding variability class in GRS 1915+105. The names of GRS 1915+105 classes are taken from Belloni et al. (2000), where more detailed descriptions can be found. Eight additional classes of GRS 1915+105 have been described; we do not find analogies to these classes in IGR J17091-3624.

IGR J17091-3624 Class	GRS 1915+105 Class
I	χ
II	ϕ
III	ν
IV	ρ
V	μ
VI	λ
VII	<i>None</i>
VIII	<i>None</i>
IX	γ

Swift, *INTEGRAL* and *Suzaku* to analyse the long-term evolution of the 2011–2013 outburst. This in turn corresponds to all available X-ray data taken during this outburst.

4.4.1 Variability Classes: IGR J17091 vs. GRS 1915

As observations of IGR J17091 and GRS 1915 suffer from different values of interstellar absorption N_H , we cannot directly compare the absolute colours of these two objects. However, we can compare the evolution of colour both over time and as a function of count rate. We therefore use these parameters, along with power spectra and lightcurve morphology, when comparing GRS 1915 with IGR J17091.

For seven of our classes, we were able to assign the closest matching class described by Belloni et al. 2000 for GRS 1915 (see Table 4.5). We are unable to find analogues to our classes VII and VIII in observations of GRS 1915, and we suggest that these classes are unique to IGR J17091.

Below, we evaluate our mapping between GRS 1915 and IGR J17091 classes, and interpret the differences between each matched pair.

Classes I and II – Figures 4.5, 4.6

Classes I and II both show low count rates and little structure in their lightcurves. The two classes in GRS 1915 that also show this lightcurve behaviour are Class χ ⁸ and Class ϕ . Belloni et al. 2000 differentiate between Classes ϕ and χ based on the hard colour (corresponding to C_2), as Class χ has a significantly higher value for this colour than Class ϕ .

⁸Note that, in GRS 1915+105, Class χ is further subdivided into four classes based on hard colour (Belloni et al., 2000; Pahari et al., 2013a). As we cannot obtain hard colour for IGR J17091, we treat χ as a single variability class here.

Data from *RXTE* indicates that the transition from the hard state to the soft intermediate state between MJDs 55612 and 55615 (Drave et al., 2012). This was confirmed by a radio spectrum taken on MJD 55623 which was consistent with an observation of discrete ejecta (Rodriguez et al., 2011a). This observation of discrete ejecta at the transition between the hard state and the intermediate state has been reported in other LMXBS (e.g. XTE J1550-564, Rodriguez et al., 2003), and has also been associated with transitions to the χ Class in GRS 1915 (Rodriguez et al., 2008, see also review by Fender, 2006).

Using Fourier PDS, we conclude that Class I is analogous to Class χ in GRS 1915, while Class II is analogous to Class ϕ . In Class χ observations of GRS 1915, broad band noise between $\sim 1 - 10$ Hz and a QPO at around 5 Hz are seen in the PDS. We find that both of these are present in Class I observations of IGR J17091. On the other hand, we find that Class ϕ observations of GRS 1915 do not show this broad band noise, and show either a weak (q -value $\lesssim 3$) QPO at ~ 5 Hz or no QPO at all. We find that the weak QPO and lack of broad band noise are also seen in the PDS of Class II observations.

Classes III and IV – Figures 4.7, 4.10

Classes III and IV both show highly regular flaring activity in their lightcurves, but they differ in terms of timescale and pulse profile. As can be seen in lightcurves in Figure 4.10, flares in Class IV occur every ~ 32 s and are nearly identical to each other in shape. On the other hand, as can be seen in Figure 4.7, flares in Class III occur every ~ 61 s and may or may not end in a much faster sharp peak which is never seen in Class IV. In Figure 4.27 we show a two-dimensional histogram of flare peak count rate against flare duration, showing all flares in all observations classified as Class III or Class IV. In this figure, we can see that flares tend to group in one of two regions in count rate-duration space; a region between $\sim 90-110$ cts s^{-1} PCU $^{-1}$ and $\sim 35-55$ s, corresponding to flares seen in Class III, and a region between $\sim 150-250$ cts s^{-1} PCU $^{-1}$ and $\sim 20-55$ s, corresponding to flares seen in Class IV. From this plot, we conclude that the flares seen in Class III exist in a different population to the flares seen in Class IV.

The GRS 1915 classes that show behaviour most similar to these are ρ and ν ; both produce similar structures in their lightcurve, but Class ν is differentiated from Class ρ by the presence of a secondary count rate peak which occurs ~ 5 s after the primary (Belloni et al., 2000).

The secondary peak is present in most Class III observations and some Class IV observations (Figure 4.28), suggesting that both classes consist of a mix of ρ -like and ν -like observations. However, the poor statistics sometimes make the presence of this secondary peak difficult to detect. As such, we do not use the presence or absence of this peak as a criterion when assigning classes. Instead we choose to separate Classes III and IV based on the larger-scale structure in their lightcurves (see Section 4.3.2). Due to the aforementioned difference in burst populations between the two classes, we suggest that classes III and IV

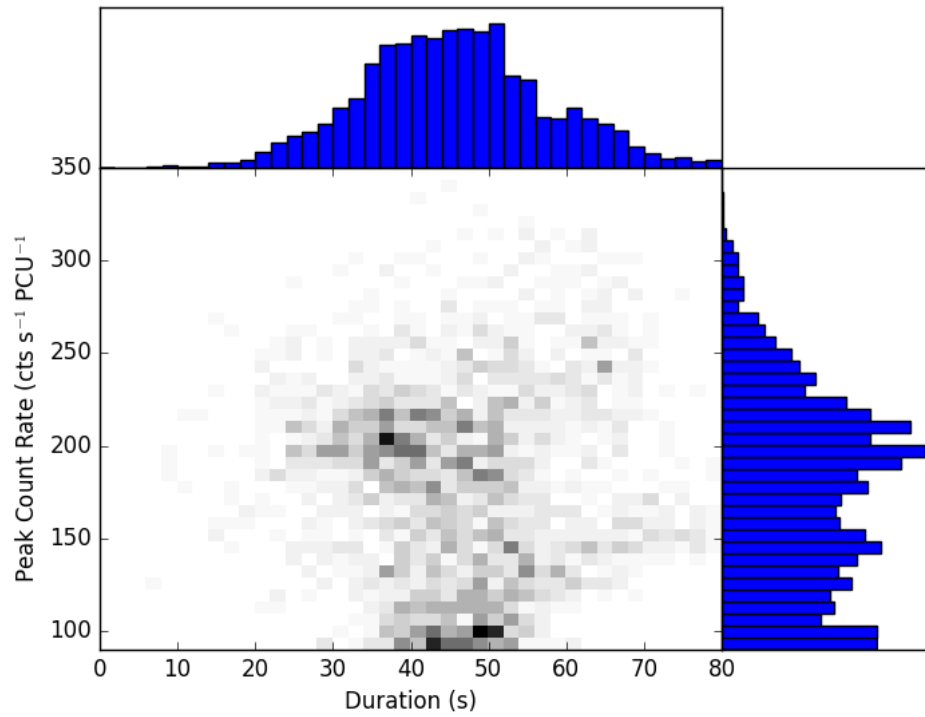


Figure 4.27: Every flare in all observations identified as Class III or Class IV, plotted in a two-dimensional histogram of flare peak count rate against flare duration to show the two-population nature of these events. Flares belonging to Class IV occupy the distribution at higher peak rate and lower duration, whereas flares belonging to Class III occupy the distribution at lower peak rate and higher duration.

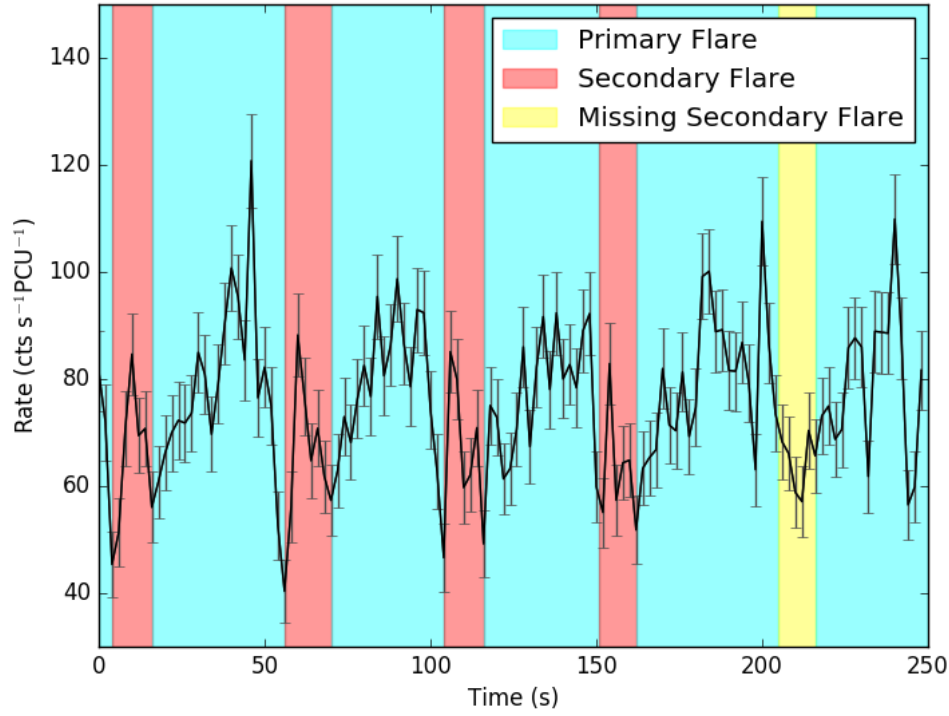


Figure 4.28: Lightcurve from Class III observation 96420-01-10-01 of IGR J17091-3624, with pairs of primary and secondary count rate spikes highlighted in cyan and red respectively. The yellow region highlights a primary count rate spike that did not produce a secondary.

do represent two distinct classes rather than a single class with a period that drifts over time. We suggest that Classes ρ and ν in GRS 1915 could also be re-partitioned in this way.

However, HID_1 loops are found to generally execute in an anticlockwise direction in Classes III and IV (previously noted by e.g. Altamirano et al., 2011b); the opposite direction to the clockwise loops in Classes ρ and ν reported by e.g. Belloni et al., 2000 and repeated by us using the same method we apply to data from IGR J17091-3624 (see Section 4.2). This suggests that Classes III and IV could be generated by a different physical mechanism to Classes ρ and ν . Alternatively, Classes III and IV could be generated by the same mechanism as ρ and ν if some other unknown process was able to alter the spectral evolution of flares in these classes.

Class V – Figure 4.12

The lightcurve of a Class V observation appears similar to that of a Class μ observation of GRS 1915, as both are characterised by rapid ρ -like flares which occur less regularly than in Class ρ . In addition to this, flares in Class μ fall into two clear populations, as do the flares in Class V. However, significant differences exist between Class V and Class μ . Class μ observations are characterised by long (~ 100 s) excursions to plateaus of high count rate,

a behaviour which is not seen in any Class V observation thus far.

We note that the HID_1 in Class V observations displays a loop in the clockwise direction; the opposite direction to the looping seen in Classes III and IV but the same direction seen in Class μ .

Regarding the two-population nature of flares seen in this class (see Section 4.3.2), we suggest that V_2 flares may simply be two V_1 flares that occur close together in time, such that the second flare starts during the decay of the first flare. This would result in an apparent two-peaked flare structure, as we see in type V_2 flares. This interpretation also accounts for the bimodal distribution of flare durations shown in the 2D histogram of Figure 4.14, as this could be caused by the misinterpretation of two-flare V_2 events as a single event. This also accounts for the Gaussian distribution of peak flare intensities seen in Figure 4.14), as the constituents of each V_2 event would be from the same population as V_1 flares.

Class VI – Figure 4.16

Class VI is dominated by long flaring periods which separate periods of low count rate, as can be seen in the lightcurve presented in Figure 4.16. Similar behaviour is seen in the lightcurves of observations of GRS 1915 belonging to Classes λ and ω (Klein-Wolt et al., 2002). However, the long count rate ‘dips’ are far less regular in Class VI than in Classes λ and ω , and we also note long periods of medium count rate during which neither flares nor dips occur. This variability class is noted by Pahari et al. (2012) who suggest that this class is unique to IGR J17091⁹. However, Pahari et al. (2013b) show that, in a plot of burst decay time against burst rise time, Classes VI and λ fall in a straight line, suggesting a similar physical origin for both.

While it is certainly true that Class VI is not a perfect analogue of either Class λ or Class ω , Class VI only differs noticeably from Class λ during the extended low-variability portions of its lightcurves. As such, we associate Class VI with Class λ .

Class VII – Figure 4.18

We are unable to find an analogue of Class VII in observations of GRS 1915. This class, and its apparent uniqueness, have previously been noted by Pahari et al., 2012¹⁰. Pahari et al. found that the C_2 hard colour in this class increases during count rate dips and decreases during count rate peaks. Here we reproduced the results of Pahari et al. and found that the anti-correlation between hard-colour and intensity is not physical, but due to the definition of C_2 : the count rate in band L_C is approximately constant and consistent with background, and therefore $C_2 = L_C/L_A \propto L_A^{-1}$, which will naturally anticorrelate with intensity.

⁹Pahari et al. (2012) refers to Class VI as Class C2.

¹⁰Pahari et al. (2012) refers to Class VII as Class C1.

Although a correlation between QPO frequency and count rate has been noted in the ~ 5 Hz QPO seen in GRS 1915 (e.g. Markwardt et al., 1999; Vignarca et al., 2003), this QPO is also seen in Class VII observations at the same time as the ~ 0.1 Hz QPO. As such, the flux-frequency relationship in the very low frequency (~ 0.1 Hz) QPO in Class VII is apparently unique amongst the classes of both IGR J17091 and GRS 1915.

Class VIII – Figure 4.20

We are unable to find an analogue of Class VIII in observations of GRS 1915. When it is flaring, the lightcurve waveform is similar to that seen in Class ρ , with rapid regular spikes in count rate. The lightcurve also shows irregular dips in count rate similar to those seen in Class VI and in Class λ in GRS 1915.

However, the amplitude of the flares in Class VIII is much larger, and the frequency much higher, than in Classes VI or λ . The amplitude of the flares in Class VIII can approach $\sim 350 \text{ cts s}^{-1} \text{ PCU}^{-1}$, while the flare separation time of 4–5 s makes Class VIII the fastest flaring activity seen in any class of IGR J17091 or GRS 1915. As such, we consider this variability class distinct from both Class VI and Class λ .

Class IX - Figure 4.21

Class IX is defined by long periods of high amplitude but unstructured variability (with a broad peaked noise component in the Fourier spectrum peaked at ~ 0.3 Hz) punctuated with infrequent irregular short-duration ‘spikes’ in which the count rate increases by a factor of ~ 2 –3. A similarity between this Class and Class γ in GRS 1915 has been previously noted by Altamirano and Belloni (2012). However, the irregular spikes seen in some Class IX lightcurves are not reproduced in Class γ lightcurves of GRS 1915.

4.4.2 General Comparison with GRS 1915+105

Overall, variability in IGR J17091 tends to be faster than structurally similar variability in GRS 1915, as can be noted in Classes III and IV compared to Classes ρ and ν (see also Altamirano et al., 2011b). Additionally, IGR J17091 also displays highly structured variability unlike anything yet seen in GRS 1915, with classes VII and VIII in particular showing very fine detail in their lightcurves.

In total we find 2 variability classes which are seen in IGR J17091 but not in GRS 1915, compared with 8 that are seen in GRS 1915 but not in IGR J17091. As relatively little data exists on GRS 1915-like variability in IGR J17091, the presence of classes in GRS 1915 that are not seen in IGR J17091 could simply be an observational effect. It is unknown how long each variability class lasts for and, as such, additional variability classes could have occurred entirely while IGR J17091 was not being observed (however, see Huppenkothen

et al., 2017 for a study on GRS1915 based on more than 16 years of data). However, GRS 1915 has displayed variability classes consistently since its discovery in 1992, implying that the two classes seen only in IGR J17091 are either completely absent in GRS 1915 or that they occur with a much lower probability. In either case, this implies physical differences between methods of generating GRS 1915-like variability in the two objects.

As noted in sections 4.4.1 to 4.4.1, variability classes seen in both IGR J17091 and GRS 1915 show differences in the different objects. In particular, we note the presence of irregular flares in Class IX which are not seen in the analogous Class γ . If these classes are indeed generated by the same processes in both objects, the differences between them must represent physical differences between the objects themselves.

It has previously been noted that, while the hardness ratios in IGR J17091 and GRS 1915 during ρ -like classes are different, the fractional hardening between the dip and peak of each flare is consistent with being the same in both objects (Capitanio et al., 2012). This suggests that the same physical process is behind the ‘heartbeats’ seen in both objects.

We note the presence of hysteretic HID_1 loops in some classes of both objects. Although these loops are always clockwise in GRS 1915, they can be executed in either direction in IGR J17091. Classes in IGR J17091 that show loops all have a preferred loop direction: anticlockwise in Classes III and IV and clockwise in classes V, VI, VII and VIII. In cases where the loop direction was opposite to that expected for a given class, loop detections were generally only marginally significant. In particular, we note that Classes IV and V tend to show loops in opposite directions, despite the similarities between their lightcurves and the ρ , ν and μ classes in GRS 1915. The fact that IGR J17091 can show HID_1 loops in both directions suggests that an increase in soft emission can either precede or lag a correlated increase in hard emission from IGR J17091. Whether soft emission precedes or lags hard emission is in turn is dependent on the variability class.

There are also non-trivial similarities between variability in the two objects. We note the presence of a $\sim 5\text{Hz}$ QPO in many of the classes seen in IGR J17091, and this same 5Hz QPO is seen in lightcurves of GRS 1915. Similarly Altamirano and Belloni (2012) reported the discovery of a 66Hz QPO in IGR J17091; a very similar frequency to the 67Hz QPO observed in GRS 1915 (Morgan et al., 1997). It is not clear why these QPOs would exist at roughly the same frequencies in both objects when other variability in IGR J17091 tend to be faster.

4.4.3 Comparison with the Rapid Burster

In 2015, Bagnoli and in’t Zand (2015) discovered the existence of two GRS 1915-like variability classes in the neutron star binary MXB 1730-335, also known as the ‘Rapid Burster’. Specifically, Bagnoli and in’t Zand (2015) note the presence of variability similar to Classes ρ and θ in GRS 1915.

Table 4.6: The six OBSIDs explicitly classified in Altamirano et al. (2011b). We also present the GRS 1915 class with which we implicitly label each OBSID in this paper.

OBSID	Altamirano <i>et al.</i> Class	Court <i>et al.</i> Class (implied)
96420-01-04-03	α	ρ/ν
96420-01-05-00	ν	ρ/ν
96420-01-06-00	ρ	ρ/ν
96420-01-07-01	ρ	μ
96420-01-08-03	β/λ	λ
96420-01-09-06	μ	λ

Class θ -like variability, seen in *RXTE* observation 92026-01-20-02 of the Rapid Burster, is not closely matched by any of the classes we identify for IGR J17091. However, the lightcurves of a Class θ observation feature large dips in count rate similar to those seen in Classes VI and VIII in IGR J17091.

Conversely, Class ρ -like variability is seen in all three objects. Bagnoli and in’t Zand (2015) note that the variability of the ρ -like flaring is slower in the Rapid Burster than in either GRS 1915 or IGR J17091. It has previously been suggested that the maximum rate of flaring in LMXBs should be inversely proportional to the mass of the central object (e.g. Belloni et al., 1997b; Frank et al., 2002). In this case, the fact that variability is faster in IGR J17091 than in GRS 1915 could simply be due to a lower black hole mass in the former object (Altamirano et al., 2011b). However if variability in the Rapid Burster is assumed to be physically analogous to variability in these two black hole objects, then we note that a correlation between central object mass and variability timescale no longer holds.

4.4.4 Comparison with Altamirano *et al.* 2011

Altamirano et al. (2011b) identify 5 GRS 1915 variability classes in a subset of observations from the 2011-2013 outburst of IGR J17091: six of these observations are presented in Table 4.6 along with the best-fit GRS 1915 class that we assign it in this paper (see also Table 4.5).

We acknowledge differences between the classifications assigned by this paper and by Altamirano et al. (2011b). We ascribe these differences to the different approaches we have used to construct our classes. In particular while we have constructed an independent set of variability classes for IGR J17091 which we have then compared to the Belloni et al. classes for GRS 1915, Altamirano et al. applied the Belloni et al. classes for GRS 1915 directly to IGR J17091.

In general, the variability classes we find to be present in IGR J17091 are broadly the same as those noted by Altamirano et al. (2011b). We do not associate any class with Class α in GRS 1915, but we find examples of all of the other variability classes posited by Altamirano et al. to exist in IGR J17091.

Altamirano et al., 2011b noted the presence of an anticlockwise loop in the HID of ‘heartbeat’-like observations of IGR J17091, opposed to the clockwise loop seen in HID of ρ -class observations of GRS 1915. This is consistent with our finding that hysteretic loops in classes III and IV also tend to execute in an anticlockwise direction. However, we additionally find that hysteretic loops in classes V, VI, VII and VIII tend to execute in a clockwise direction. This is also different from GRS 1915, in which the loop is executed in the same direction in all classes. We also additionally report that clockwise loops tend to be more complex than anticlockwise loops seen in IGR J17091, with many showing a multi-lobed structure not seen in GRS 1915. This apparent inconsistency between the objects strengthens the suggestion in Altamirano et al., 2011b that the heartbeat-like classes in GRS 1915 and IGR J17091 may be generated by physically different mechanisms.

4.4.5 New Constraints on Accretion Rate, Mass & Distance

The constraints that Altamirano et al., 2011b placed on the mass and distance of IGR J17091 assumed that the object emitted at its Eddington luminosity at the peak of the 2011–2013 outburst. They report a peak 2–50 keV flux of 4×10^{-9} ergs s $^{-1}$ cm $^{-2}$ during flares in ‘heartbeat’-like lightcurves during this time. The correction factor $C_{Bol,Peak}$ to convert 2–50 keV flux to bolometric flux is not well constrained, but Altamirano et al., 2011b suggest an order-of-magnitude estimate of $\lesssim 3$, corresponding to a peak bolometric flux of $\lesssim 1.2 \times 10^{-8}$ ergs s $^{-1}$ cm $^{-2}$.

Maccarone, 2003 performed a study of the soft to hard transitions in 10 LMXBs. They found that all but one perform this transition at a luminosity consistent with between 1% and 4% of the Eddington limit. We use *Swift* observation 00031921058 taken on MJD 55965 to create a spectrum of IGR J17091 during the approximate time of its transition from a soft to a hard state (Drave et al., 2012). We fit this spectrum above 2 keV with a power-law, and extrapolate to find a 2–50 keV flux of 8.56×10^{-10} ergs s $^{-1}$ cm $^{-2}$. Assuming that the transition bolometric correction factor $C_{Bol,Tran}$ is also $\lesssim 3$, this corresponds to a bolometric flux of $\lesssim 2.5 \times 10^{-9}$ ergs s $^{-1}$ cm $^{-2}$.

By comparing this with the results of Maccarone, 2003 and Altamirano et al., 2011b, we find that IGR J17091-3624 was likely emitting at no more than ~ 5 –20% of its Eddington Limit at its peak. This number becomes ~ 6 –25% if we instead use $C_{Bol,Tran} = 2.4$, or ~ 8 –33% if $C_{Bol,Tran} = 1.8$. With this new range of values, we are able to re-derive the compact object mass as the function of the distance (Figure 4.29). We find that for a black hole mass of $\sim 10M_{\odot}$, as suggested by Iyer et al., 2015b, IGR J17091 is within the galaxy at a distance of 6–17 kpc. This is consistent with the estimated distance of ~ 11 –17 kpc estimated by Rodriguez et al., 2011a for a compact object mass of $10M_{\odot}$.

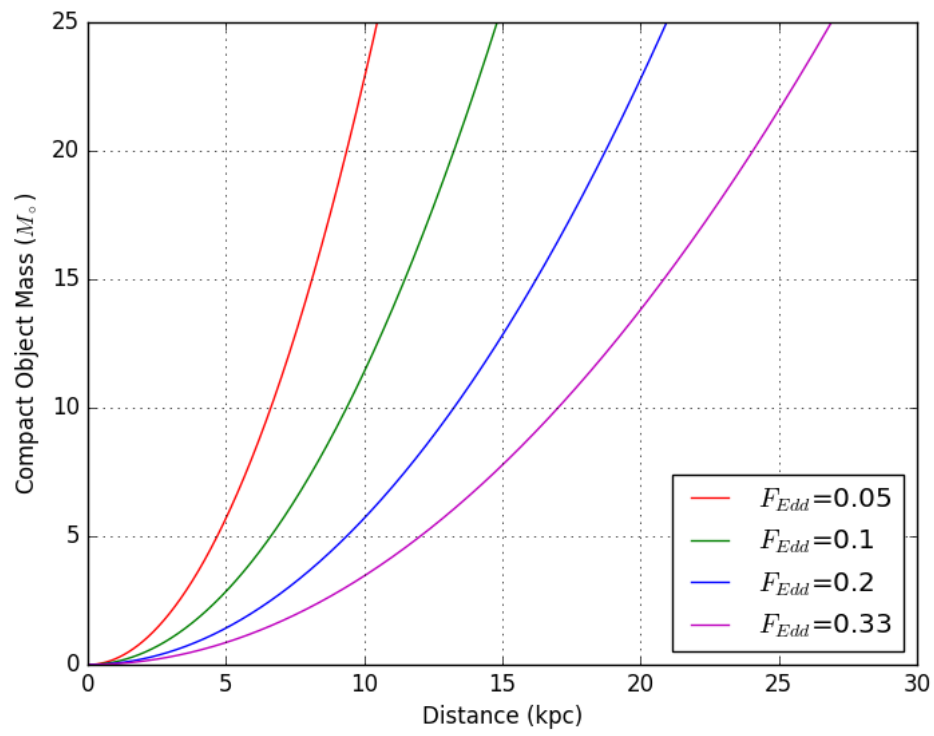


Figure 4.29: Mass of the compact object in IGR J17091-3624 plotted against its distance, for values of peak Eddington fractions of $F_{Edd} = 0.05, 0.1, 0.2$ and 0.33 .

4.4.6 Implications for Models of ‘Heartbeat’ Variability

We have found that hysteretic HID loops can execute in both directions in IGR J17091 (e.g. Section 4.4.4), as well as found a revised estimate that IGR J17091 accretes at $\lesssim 20\%$ Eddington (Section 4.4.5). Both of these findings have implications for physical models of GRS 1915-like variability in this source.

Firstly, we find that Eddington-limited accretion is neither necessary nor sufficient for GRS 1915-like variability. The discovery of GRS 1915-like variability in the sub-Eddington Rapid Burster (Bagnoli and in’t Zand, 2015; Bagnoli et al., 2015) provided the first evidence that Eddington-limited accretion may not be a driving factor in this type of variability. We strengthen this case by finding that IGR J17091-3624 is also likely sub-Eddington. As such, we further rule out any scenario in which Eddington-limited accretion is required for GRS 1915-like variability in black hole LMXBs specifically.

Secondly, by using the direction of hysteretic HID loops, we find that hard photon lag in ‘heartbeat’-like classes of IGR J17091 can be either positive or negative. This could mean that we must rule out the causal connection between soft and hard emission being common to all classes.

In either case, we find that scenarios that require high global accretion rates or predict a consistent hard photon lag (e.g. Neilsen et al., 2011; Janiuk and Czerny, 2005), are not able to explain GRS 1915-like variability in IGR J17091 unless they also feature geometric obscuration in a subset of variability classes. We note that simulations by Nayakshin et al., 2000 require an Eddington fraction of $\gtrsim 0.26$ before GRS 1915-like variability, a value which falls in the range $\sim 0.05\text{--}0.33$ that we find for the peak Eddington fraction of IGR J17091.

In addition to being near its Eddington limit GRS 1915 also has the largest orbit of any known LMXB (e.g. McClintock and Remillard, 2006). Sądowski, 2016 have also shown that thin, radiation dominated regions of disks in LMXBs require a large-scale threaded magnetic field to be stable, and the field strength required to stabilise such a disk in GRS 1915 is higher than for any other LMXB they studied. We suggest that one of these parameters is more likely to be the criterion for GRS 1915-like variability. If better constraints can be placed on the disk size and minimum stabilising field strength in IGR J17091, it will become clear whether either of these parameters can be the unifying factor behind LMXBs that display GRS 1915-like variability.

4.5 Conclusions

We have constructed the first model-independent set of variability classes for the entire portion of the 2011–2013 outburst of IGR J17091 that was observed with *RXTE*. We find that the data are well-described by a set of 9 classes; 7 of these appear to have direct

counterparts in GRS 1915, while two are, so far, unique to IGR J17091. We find that variability in IGR J17091 is generally faster than in the corresponding classes of GRS 1915, and that patterns of quasi-periodic flares and dips form the basis of most variability in both objects. Despite this, we find evidence that ‘heartbeat’-like variability in both objects may be generated by different physical processes. In particular, while hard photons always lag soft in GRS 1915, we find evidence that hard photons can lag or precede soft photons in IGR J17091 depending on the variability class.

We also report on the long-term evolution of the 2011–2013 outburst of IGR J17091, in particular noting the presence of 3 re-flares during the later part of the outburst. Using an empirical relation between hard-soft transition luminosity and Eddington luminosity (Maccarone, 2003), we estimate that IGR J17091 was likely accreting at no greater than $\sim 33\%$ of its Eddington limit at peak luminosity.

We use these result to conclude that any model of GRS 1915-like variability which requires a near-Eddington global accretion rate is insufficient to explain the variability we see in IGR J17091. As such we suggest that an extreme value of some different parameter, such as disk size or minimum stabilising large-scale magnetic field, may be the unifying factor behind all objects which display GRS 1915-like variability. This would explain why sub-Eddington sources such as IGR J17091 and the Rapid Burster do display GRS 1915-like variability, while other Eddington-limited sources such as GX 17+2 and V404 Cyg do not.

Chapter 5

Burst Evolution in GRO J1744-28

Chapter 6

GRO J1744-28: the Transitional Pulsar Link

6.1 Introduction

Millisecond Pulsars are old radio pulsars with spin periods of order ~ 10 ms (Backer et al., 1982). They have long been believed to be the end product of systems containing a neutron star (NS) in a Low Mass X-ray Binary (LMXB). In these systems, matter from a Roche-lobe overflowing star donates angular momentum to a NS, spinning it up to frequencies of several 100 Hz (Alpar et al., 1982). A number of fast-spinning X-ray pulsars (accreting Millisecond Pulsars, or AMXPs) have been found in LMXBs (e.g. Wijnands and van der Klis, 1998; Altamirano et al., 2008a; Patruno et al., 2017; Sanna et al., 2017a), seemingly confirming this physical picture. At the end of this so-called ‘recycling’ process, the system should transition from an accretion-powered pulsar to a rotation-powered pulsar. As such, it has long been expected that such a transition could be observed by finding a system which changes its character from an accreting NS at one time to a radio pulsar at some later time. Subsequently a small family of 6 candidate objects have been discovered or proposed: these are referred to as Transitional Millisecond Pulsars (TMSPs).

The first of these objects, **PSR J1023+0038**, was identified by Archibald et al., 2009. Although this object appeared as a non-accreting radio pulsar at the time of identification in 2009, previous optical studies showed that this system contained an accretion disk in 2002 (Szkody et al., 2003). As such, the pulsar in this system must have switched from an accreting phase to a radio pulsar phase at some point between 2003 and 2009, strongly suggesting the identification of this system as a TMSP. The pulsar in this system has a spin period of 1.69 ms, and the companion is a very low mass star with a mass between $\sim 0.14\text{--}0.42 M_{\odot}$. Archibald et al., 2009 suggested that the low X-ray luminosity of PSR J1023+0038 in its accreting phase was due to accretion taking place in the ‘propeller regime’ (Illarionov and Sunyaev, 1975). In this regime, accreting matter is halted by

magnetic pressure above the co-rotation radius of the NS magnetosphere. This matter is then ejected from the system as a wind. Whether a system is in the propeller regime depends on its spin and its magnetic field strength (Lewin et al., 1988). Additionally, below a certain accretion rate, no stable balance between ram pressure and radiation pressure can form and any disk is ejected from the system (e.g. Campana et al., 1998). Archibald et al., 2009 suggested that the current accretion rate in PSR J1023+0038 is only slightly below this critical value, and that any small increase in accretion rate could cause accretion in this system to resume. They suggested the possibility of TMSP systems which flip back and forth between accreting and radio pulsar phases multiple times.

Papitto et al., 2013a identified **IGR J18245-2452** as the first pulsar to switch from a radio pulsar to an AMXP and back to a radio pulsar. This source was first observed as a radio pulsar (Manchester et al., 2005), before being observed several years later by *XMM-Newton* (Eckert et al., 2013) as an AMXP. Several months after the *XMM-Newton* observation, Papitto et al., 2013b found that the source had reactivated as a radio pulsar during X-ray quiescence. The pulsar in this system has a period of 3.93 ms, and the companion star has a mass of $> 0.17 M_{\odot}$ (Papitto et al., 2013a). During the 2013 outburst of IGR J18245-2452, Ferrigno et al., 2014 reported the presence of high-amplitude variability in the X-ray lightcurve. They interpreted this as being due to the accretion rate \dot{M} being very close to the critical rate at which the propeller effect begins to dominate the flow geometry. In this regime, small fluctuations in \dot{M} cause so-called ‘hiccups’, in which matter alternates between being ejected by the propeller effect and being accreted onto the NS poles. Similar X-ray variability has subsequently been found in lightcurves from outbursts during the accreting phase of PSR J1023+0038 (Bogdanov et al., 2015), suggesting that this variability is somehow intrinsic to TMSPs as a class of objects.

1FGL J1227.9-4852, was first identified in the first *Fermi*/LAT source catalogue (Abdo et al., 2010). Hill et al., 2011 found that the γ -ray spectral characteristics of this source are consistent with known millisecond radio pulsars, although no radio pulsations were found. They also suggested that this object could be associated with the X-ray source XSS J12270-4859. Before 2009, XSS J12270-4859 showed optical emission lines typical of an accretion disk (Pretorius, 2009). Hill et al., 2011 suggested that XSS J12270-4859 may also be a TMSP, which switched from an accreting phase to a radio pulsar millisecond pulsar phase between 2009 and 2011. Subsequent studies have found pulsations in both the radio (Roy et al., 2015) and γ -ray (Johnson et al., 2015) emissions of this source, confirming the system contains a pulsar and establishing its spin period at 1.69 ms.

3FGL J1544.6-1125 was also first identified in *Fermi*/LAT data. Bogdanov and Halpern, 2015 associated this object with the X-Ray source 1RXS J154439.4-112820. Due to the presence of γ -rays, as well as the presence of variability in the X-ray lightcurve similar to IGR J18245-2452, they proposed that this object is a TMSP in the accreting state. However, no pulsations from this system have been detected in the X-ray or the radio, so the pulsar period is not known. Bogdanov and Halpern, 2015 found a strong bimodality in count rate

during the period of X-ray variability, suggesting that this behaviour can be explained as quick transitions between three quasi-stable accretion modes known as ‘low’, ‘high’ and ‘flaring’. This effect has also been seen in variability from the TMSP IGR J18245-2452 (Ferrigno et al., 2014).

Strader et al., 2016 identified the γ -ray source, **3FGL J0427.9-6704**, as a TMSP. They found that this source also displays X-ray variability similar to what is seen from the other known TMSPs. Finally, Rea et al., 2017 have proposed that the X-ray source **XMM J083850.4-282759** may also be a TMSP. Although this source has not been detected in the gamma or the radio, the authors argued that X-ray variability coupled with X-ray flaring seen from this object is reminiscent of similar behaviour seen in other TMSPs during subluminal disk states.

The phenomenology of currently known TMSPs is varied, and different methods have been used to conclude (or propose) that each individual system belongs to this class. The fact that all 6 objects show similar patterns of X-ray variability during outburst suggests that this variability can be used as an indication that a system may be a TMSP. In this letter we present evidence that a 7th object, the so-called ‘Bursting Pulsar’ **GRO J1744-28**, may also be associated with this family of objects.

6.2 GRO J1744-28: The Bursting Pulsar

GRO J1744-28, or the ‘Bursting Pulsar’ (hereafter BP, Paciesas et al., 1996), is an LMXB containing a 2.4 Hz pulsar and a $\gtrsim 0.07 M_{\odot}$ companion star (e.g. Sturmer and Dermer, 1996; Finger et al., 1996b; Degenaar et al., 2014); the orbital period of the systems is 11.8 d (Finger et al., 1996a; Sanna et al., 2017c). Estimates for the NS magnetic field range between 2 and 50×10^{10} G (Finger et al., 1996b; Degenaar et al., 2014; D’Aì et al., 2015; Doroshenko et al., 2015). The BP is one of only two known systems that show ‘Type II’ X-ray bursts: bright, ~ 10 s-long non-thermonuclear X-ray flares. The “Rapid Burster” (i.e. MXB 1730-33; hereafter RB), is the other system (e.g. Lewin et al., 1976; Kouveliotou et al., 1996).

A number of physical models have been proposed to explain Type II bursts, including among others, viscous instabilities and interactions between the disk and the rotating NS magnetosphere (e.g. Taam and Lin, 1984; Spruit and Taam, 1993). None of the proposed models can fully reproduce the observed phenomenology (Lewin et al., 1993), nor explain the significant differences observed between the BP and the RP (e.g. Lewin et al., 1996, Court et al. *in prep*). Most importantly, so far it is not understood what differentiates the RB and the BP from the more than 100 known NS-LMXBs (e.g. Liu et al., 2007) which do not show Type II bursts. De Martino et al., 2013 previously noted similarities between Type II bursting and X-ray variability in the lightcurve of the TMSP 1FGL J1227.9-4852 (Hill et al., 2011). However, the authors note that the energetics are inconsistent with these

phenomena being physically the same.

In Court et al. (*in prep.*), we performed a detailed analysis of all archival X-ray data (including *RXTE*, *Swift*, *Chandra*, *XMM-Newton*, *Suzaku*, *NuStar*, *Fermi* and *INTEGRAL*) and found that the Type II phenomenology in the BP is much richer than previously thought (e.g. Giles et al., 1996): the characteristics of the flaring evolve with time and source luminosity. Near the end of this evolution, we observed periods of highly-structured and complex high-amplitude X-ray variability. We refer to this variability as ‘Structured Bursting’, which is unlike what is seen other LMXBs but very similar to the ‘hiccup’ accretion observed in TMSPs.

6.3 Comparison

In Figure 6.1, we show *RXTE* lightcurves of ‘Structured Bursting’ from the BP alongside lightcurves from periods of ‘hiccup’ variability observed in the confirmed TMSPs PSR J1023+0038 and IGR J18245–2452 respectively. All three sources show similar patterns of X-ray variability: (i) *Plateaus*: periods of approximately constant count rate with high-amplitude flicker noise (all plateaus in a given observation have approximately the same mean rate), (ii) *Dips*: Periods of low count rate ($\lesssim 0.5$ of the rate in plateaus) with significantly less flicker noise, and (iii) *Flares*: Relatively short-lived increases of the count rate to values $\gtrsim 2$ times greater than the rate during plateaus. In TMSPs, these features are interpreted as representing three quasi-stable accretion modes: the ‘high’, ‘low’ and ‘flaring’ modes respectively (e.g. Bogdanov et al., 2015). The most significant difference is that, in general, the variability in the BP occurs on timescales ~ 1 order of magnitude longer than those on the TMSPs.

To further compare the BP with TMSPs, in Figure 6.2 we show histograms of the 1 s-binned count-rate from all *RXTE* observations of Structured Bursting in the 1996 (left) and 1997 (right) outbursts of the BP. As is the case for TMSPs, the histograms can be described with a number of log-Normally distributed populations: 3 populations in the 1996 outburst and 2 in the 1997 outburst. It is unclear why a population would be absent from the 1997 outburst, but some TMSPs have been observed to miss the ‘high’ mode during hiccup accretion (e.g. IGR J18245-2452, Ferrigno et al., 2014).

Detailed works on the low and high modes observed in the light curves of TMSPs show that X-ray pulsations are seen during both modes. Pulsations are fractionally weaker in the low state than the high state (for example varying between $4.0 \pm 0.2\%$ and $16.8 \pm 0.2\%$ in the TMSP IGR J18245-2452, Ferrigno et al., 2014). In the case of the BP, we detect pulsations both during the low and the high modes; much like in TMSPs, the pulsations are weaker in the low mode. For example in *RXTE* OBSID 10401-01-59-00 (in 1996), the pulsations had amplitudes of $3.5 \pm 0.2\%$ and $4.9 \pm 0.2\%$ respectively, while in OBSID 20078-01-23-00 (in 1997), the pulsations had amplitudes of $4.5 \pm 0.1\%$ and $6.0 \pm 0.1\%$ respectively. A

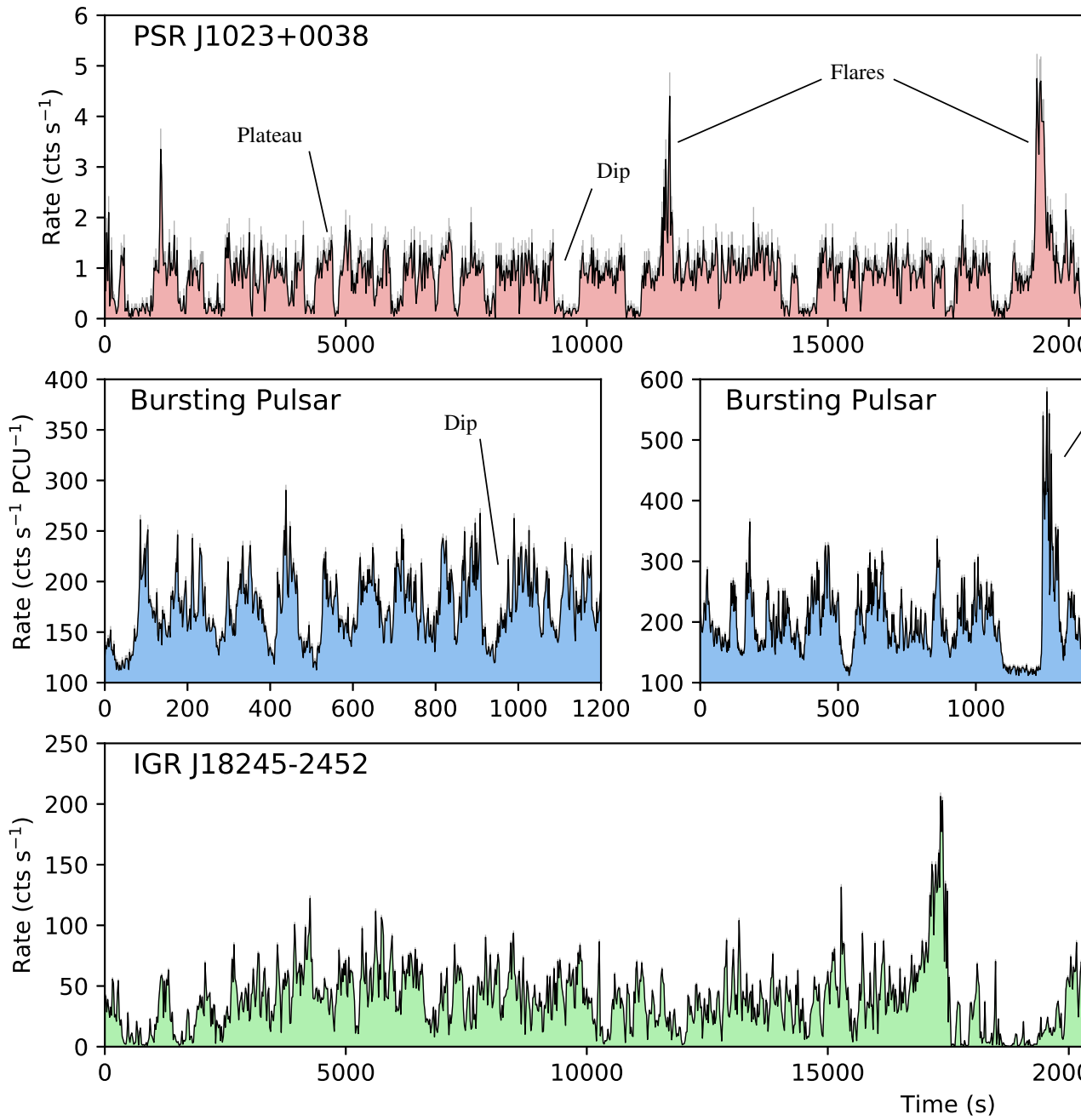


Figure 6.1: **Top:** 2–15 keV *XMM* lightcurve from the TMSP PSR J1023+0038. **Middle:** 2–60 keV *RXTE* lightcurves from the Bursting Pulsar during its 1996 and 1997 outbursts, showing similar variability patterns to those seen in PSR J1023+0038. **Bottom:** 2–15 keV *XMM* lightcurve from the TMSP IGR J18245-2452. *XMM* lightcurves are shown from 2–15 keV so that they can be more directly compared with *RXTE*.

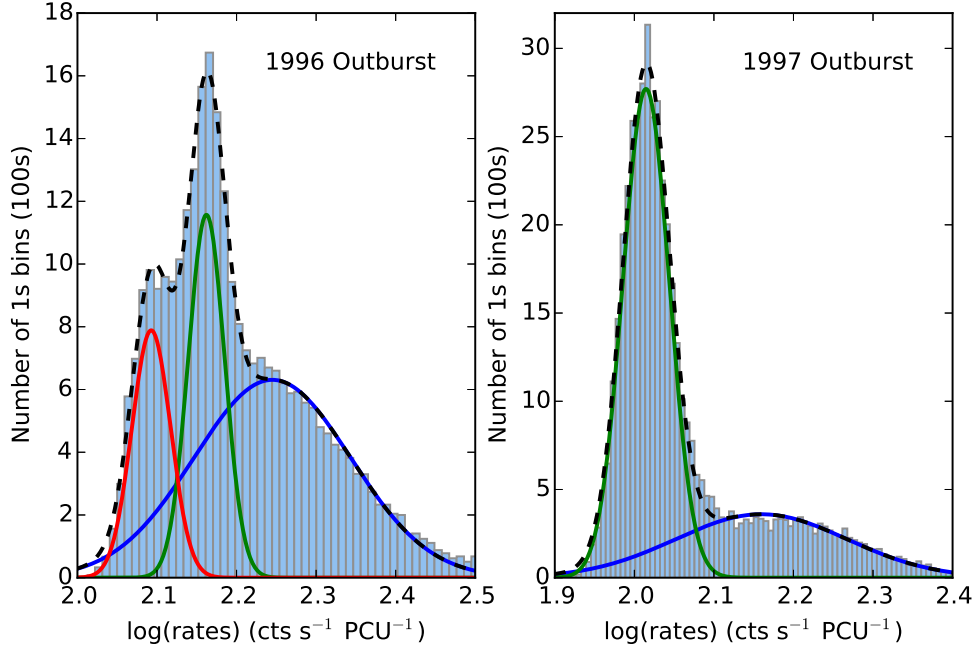


Figure 6.2: Histograms of the 1 s binned count rates from all *RXTE* observations of Structured Bursting in the 1996 (left) and 1997(right) outbursts of the Bursting Pulsar. For the 1996 outburst, we fit the distribution with three Gaussians, while for the 1997 outburst we fit the distribution with 2 Gaussians. The individual Gaussians are plotted in solid lines, while the combined total is plotted in a dashed line.

reduction in pulse fraction in accreting pulsars has been interpreted as a change in accretion geometry due to a sudden decrease in the amount of matter reaching the compact object (e.g. Ibragimov and Poutanen, 2009), and as such this result provides direct evidence that the Structured Bursting in the BP is caused by switches between accretion and propeller-driven outflows.

The spectral evolution of known TMSPs is varied. In PSR J1023+0038, the low, high and flaring modes all present similar spectra (Bogdanov et al., 2015). However in IGR J18245-2452, Ferrigno et al., 2014 have found a strong correlation between spectral hardness and intensity during hiccups, showing that there is spectral evolution over time in this source. In Figure 6.3 we show the hardness-intensity diagram of the Bursting Pulsar during periods of Structured Bursting. We find a significant correlation, similar to what is seen in IGR J18245-2452 (Ferrigno et al., 2014).

TMSPs are amongst the only LMXBs which are also significant γ -ray sources (e.g. Hill et al., 2011). The *Fermi* point source 3FGL J1746.3–2851c is spatially coincident with the BP. While the field is too crowded to unambiguously associate 3FGL J1746.3–2851c with the BP, the existence of a γ -ray point source at this location is consistent with the possibility that the BP and TMSPs show the same phenomenology.

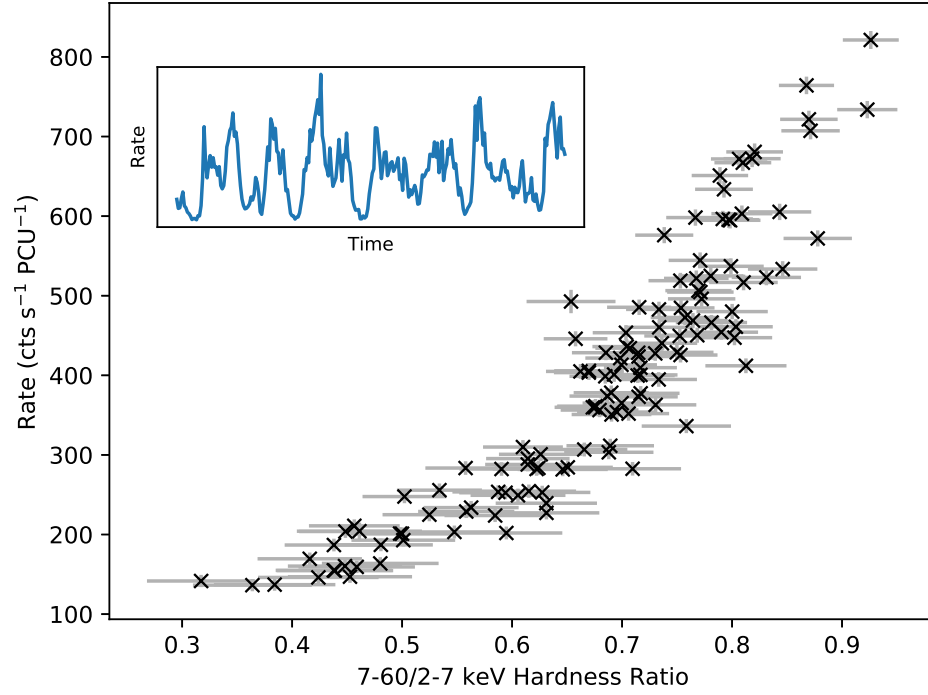


Figure 6.3: A 7–60/2–7 keV hardness-intensity diagram for *RXTE* observation 10401-01-59-00; the lightcurve of this observation is shown in the inset. To correct for the high background of the region, we subtract the median count rate of *RXTE* observation 30075-01-24-00 from each band; at this time, GRO J1744-28 was in quiescence. We find a strong correlation between hardness and count rate, with a Spearman Rank Correlation Coefficient of 0.93. Data for the hardness-intensity diagram are binned to 10 s, while data for the lightcurve are binned to 5 s.

6.4 Discussion

In this letter we compare the lightcurve, spectral and timing properties of the Bursting Pulsar at the end of its 1996 and 1997 outburst with those observed from Transitional Millisecond Pulsars. The data suggest that the BP may have undergone “hiccup” accretion similar to that seen in TMSPs, during which transferred matter alternates between being accreted onto the poles of the NS and being ejected from the system by the ‘propeller’ effect (e.g. Ferrigno et al., 2014). This similarity raises the exciting prospect of studying the physics of TMSPs in a completely different regime.

Very recently Campana et al., 2017 proposed a universal relation between magnetic moment, spin frequency, stellar radius and luminosity at the boundary between accretion and the propeller effect. Any object that exists on one side of this boundary should be able to accrete, whereas objects on the other side should be in the propeller phase or not accreting at all. In Figure 6.4 we reproduce Campana et al., 2017’s results and include our estimates for the BP during the periods of Structured Bursting. We find that the BP is consistent with lying on or near the boundary between propeller-mode and direct accretion, clustering with High Mass X-ray Binaries (as expected due to the BP’s high magnetic field), and supporting the link between “hiccups” and Structured Bursting.

If the “hiccups” in the BP show that the system is transiting to a radio pulsar, then the BP should not lie in the $P-\dot{P}$ ‘graveyard’ region (e.g. van den Heuvel, 1993). To our knowledge, there is no measurement yet of the NS spin down during the BP’s X-ray quiescent state. Under the assumption that the BP becomes a radio pulsar, and that the possible spin down during that period is due to the same mechanism as those of the known radio pulsars, we can position the BP in the $P-\dot{P}$ diagram (the plot of pulsar spin P against spin-down rate \dot{P} , not shown) by using the orbital period and estimates of its magnetic field. At $B \sim 2 \times 10^{11} \text{G}$, the BP falls well outside of the pulsar graveyard. We note that Pandey-Pommier et al. (2014) and Russell et al. (2017) did not detect a significant radio source at the location of the BP during X-ray outburst. To our knowledge, there is no report of Radio detection/non-detection during X-ray quiescence.

In addition to the BP, several additional sub-10 Hz accreting X-ray pulsars have been discovered (e.g. GX 1+4 and 4U 1626-67, Lewin et al., 1971; Rappaport et al., 1977). The reason behind the slow spins of these objects is poorly understood, but a number of these systems have been seen to undergo ‘torque reversal’ events, during which \dot{P} switches sign (e.g. Chakrabarty et al., 1997b,a). In some sources, the magnitude of the spin-down during such an event is of the same order magnitude as the preceding period of spin-up, resulting in little or no net spin change. Torque reversal events occur irregularly, but the recurrence timescale varies drastically between objects; from weeks to decades (e.g. Bildsten et al., 1997).

Given that the BP has a strongly stripped stellar companion (Bildsten and Brown, 1997) and shows significant spin-up during outburst (e.g. Finger et al., 1996b; Sanna et al., 2017c), it

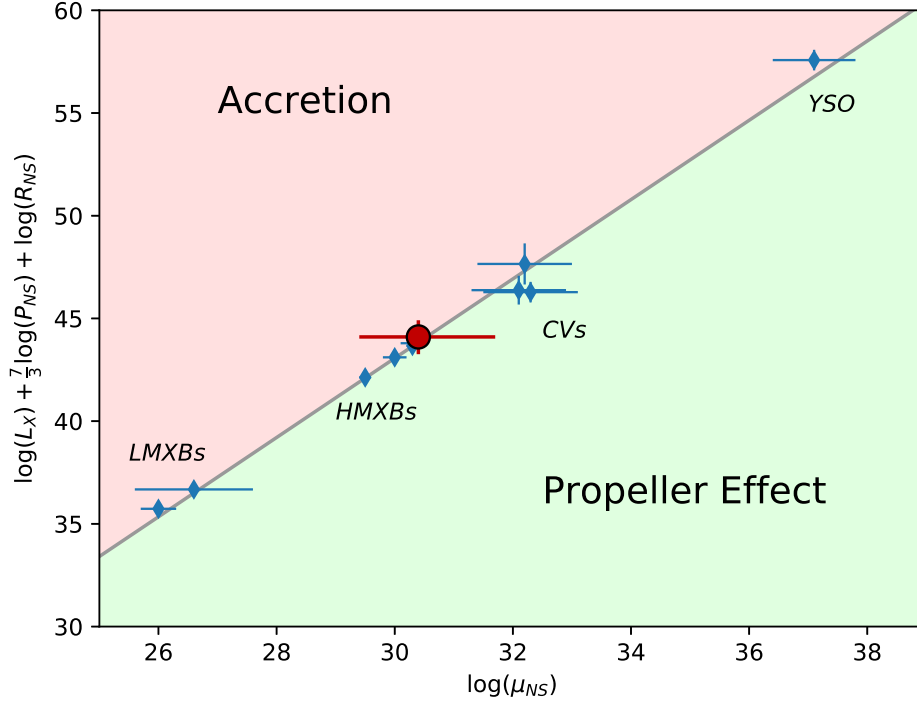


Figure 6.4: A plot of a number of objects ranging in scale from LMXBs and High-Mass X-ray Binaries (HMXBs) to Cataclysmic Variables (CVs) and Young Stellar Objects (YSOs) (blue diamonds). In each case, the object is plotted at the luminosity which defines its transition between propeller-mode accretion and free accretion. Campana et al., 2017 suggest that any object falling above the line of best fit accretes freely, whereas all objects below are inhibited by the propeller effect. The Bursting Pulsar (red circle) is consistent with approaching this line during periods of Structured Bursting. Errorbars on the Bursting pulsar represent the range of the reported magnetic fields (see Section 6.2) as well as a range of stellar radii between 10–20 km. The range in luminosity for the BP is calculated using 1.5–25 keV *RXTE*/PCA flux, assuming a distance of between 4–8 kpc (e.g. Kouveliotou et al., 1996; Gosling et al., 2007; Sanna et al., 2017c) and a bolometric correction factor of 1–3. Data on the other objects taken from Campana et al., 2017. L is the bolometric luminosity of the object in ergs s^{-1} , P is the period in s, R is the radius in cm and μ is the magnetic moment in Gauss cm^3 .

is difficult to explain its low spin by suggesting the system is young or that the angular momentum transfer is inefficient. Torque reversal events in this system (similar to those seen in other slow accreting pulsars, e.g. Bildsten et al., 1997) could explain why the pulsar has failed to reach a spin rate on par with TMSPs. Although no torque reversal event has been reported from the BP, it is feasible that the recurrence timescale of such an event is longer than the ~ 20 years for which the object has been studied (this is consistent with the recurrence timescales seen in other slow accreting pulsars). The discovery of torque reversal in the BP would strongly link it with the other known slow accreting pulsars. Additionally, it would potentially be the first known instance of torque reversal in a TP-like object.

MXB 1730-335 (the “Rapid Burster”) is often compared to the BP due to the presence of regular Type II X-ray bursts in both objects (e.g. Lewin et al., 1996). This system also contains an accreting NS. Iaria et al., 2018 have suggested that the vast majority of matter transferred in this system is ejected, similar to a scenario suggested by Degenaar et al., 2014 to explain high-velocity winds from the BP. However it remains unclear why the RB does not show pulsations or display the ‘hiccup’ behaviour seen in the BP.

The BP has a spin rate ~ 2 orders of magnitude less than previously known TMSPs, and a magnetic field ~ 2 orders of magnitude stronger, but it still shows lightcurve, timing and spectral behaviour which are remarkably similar to TMSPs. This raises the exciting prospect of exploring the physics of TMSPs in a previously unexplored physical regime. If the BP is a TP, then it should emit radio pulsations during X-ray quiescence. Future detections of radio pulsations from this object would unambiguously confirm it as a TP.

Chapter 7

Conclusions

Bibliography

- Abdo, A. A., Ackermann, M., Ajello, M., Allafort, A., Antolini, E., Atwood, W. B., Axelsson, M., Baldini, L., Ballet, J., Barbiellini, G., and et al. (2010). Fermi Large Area Telescope First Source Catalog. *ApJS*, 188:405–436.
- Abramowicz, M. A., Czerny, B., Lasota, J. P., and Szuszkiewicz, E. (1988). Slim accretion disks. *ApJ*, 332:646–658.
- Allen, J. L., Linares, M., Homan, J., and Chakrabarty, D. (2015). Spectral Softening Between Outburst and Quiescence In The Neutron Star Low-Mass X-Ray Binary SAX J1750.8-2900. *ApJ*, 801:10.
- Alpar, M. A., Cheng, A. F., Ruderman, M. A., and Shaham, J. (1982). A new class of radio pulsars. *Nature*, 300:728–730.
- Altamirano, D. and Belloni, T. (2012). Discovery of High-frequency Quasi-periodic Oscillations in the Black Hole Candidate IGR J17091-3624. *ApJ*, 747:L4.
- Altamirano, D., Belloni, T., Krimm, H., Casella, P., Curran, P., Kennea, J., Kalamkar, M., van der Klis, M., Wijnands, R., Linares, M., Motta, S., Munoz-Darias, T., and Stiele, H. (2011a). IGR J17091-3624 undergoes 'heartbeat' oscillations similar to those of GRS 1915+105. *The Astronomer's Telegram*, 3230.
- Altamirano, D., Belloni, T., Linares, M., van der Klis, M., Wijnands, R., Curran, P. A., Kalamkar, M., Stiele, H., Motta, S., Muñoz-Darias, T., Casella, P., and Krimm, H. (2011b). The Faint "Heartbeats" of IGR J17091-3624: An Exceptional Black Hole Candidate. *ApJ*, 742:L17.
- Altamirano, D., Casella, P., Patruno, A., Wijnands, R., and van der Klis, M. (2008a). Intermittent Millisecond X-Ray Pulsations from the Neutron Star X-Ray Transient SAX J1748.9-2021 in the Globular Cluster NGC 6440. *ApJ*, 674:L45.
- Altamirano, D., Linares, M., van der Klis, M., Wijnands, R., Kalamkar, M., Casella, P., Watts, A., Patruno, A., Armas-Padilla, M., Cavecchi, Y., Degenaar, N., Kaur, R., Yang, Y., and Rea, N. (2011c). Discovery of 10 mHz quasi-periodic oscillations likely from IGR J17091-3624. *The Astronomer's Telegram*, 3225.

- Altamirano, D., van der Klis, M., Méndez, M., Jonker, P. G., Klein-Wolt, M., and Lewin, W. H. G. (2008b). X-Ray Time Variability Across the Atoll Source States of 4U 1636-53. *ApJ*, 685:436–450.
- Altamirano, D., Wijnands, R., and Belloni, T. (2013). The black hole candidate IGR J17091-3624 going to quiescence. *The Astronomer’s Telegram*, 5112.
- Altamirano, D., Wijnands, R., Belloni, T., and Motta, S. (2012). The black hole candidate IGR J17091-3624 is still active. *The Astronomer’s Telegram*, 3913.
- Angelini, L., White, N. E., and Stella, L. (1991). The discovery of an X-ray burst and a study of aperiodic variability from SMC X-1. *ApJ*, 371:332–341.
- Aptekar, R. L., Butterworth, P. S., Cline, T. L., Frederiks, D. D., Golenetskii, S. V., Il’inskii, V. N., Mazets, E. P., Stilwell, D. E., and Terekhov, M. M. (1998). Hard X-Ray Bursts from GRO J1744-28. I. Observations by the Konus-Wind and Konus-A Experiments. *ApJ*, 493:404–407.
- Aptekar, R. L., Butterworth, P. S., Golenetskii, S. V., Il’inskii, V. N., Cline, T. L., Mazets, E. P., Stilwell, D. E., Terekhov, M. M., and Frederiks, D. D. (1997). Long-term activity of the bursting x-ray pulsar GRO J1744-28 from Konus-Wind and Konus-A observations. *Astronomy Letters*, 23:147–154.
- Archibald, A. M., Kaspi, V. M., Bogdanov, S., Hessels, J. W. T., Stairs, I. H., Ransom, S. M., and McLaughlin, M. A. (2010). X-ray Variability and Evidence for Pulsations from the Unique Radio Pulsar/X-ray Binary Transition Object FIRST J102347.6+003841. *ApJ*, 722:88–95.
- Archibald, A. M., Stairs, I. H., Ransom, S. M., Kaspi, V. M., Kondratiev, V. I., Lorimer, D. R., McLaughlin, M. A., Boyles, J., Hessels, J. W. T., Lynch, R., van Leeuwen, J., Roberts, M. S. E., Jenet, F., Champion, D. J., Rosen, R., Barlow, B. N., Dunlap, B. H., and Remillard, R. A. (2009). A Radio Pulsar/X-ray Binary Link. *Science*, 324:1411.
- Arnaud, K. A. (1996). XSPEC: The First Ten Years. In Jacoby, G. H. and Barnes, J., editors, *Astronomical Data Analysis Software and Systems V*, volume 101 of *Astronomical Society of the Pacific Conference Series*, page 17.
- Astropy Collaboration, Robitaille, T. P., Tollerud, E. J., Greenfield, P., Droettboom, M., Bray, E., Aldcroft, T., Davis, M., Ginsburg, A., Price-Whelan, A. M., Kerzendorf, W. E., Conley, A., Crighton, N., Barbary, K., Muna, D., Ferguson, H., Grollier, F., Parikh, M. M., Nair, P. H., Unther, H. M., Deil, C., Woillez, J., Conseil, S., Kramer, R., Turner, J. E. H., Singer, L., Fox, R., Weaver, B. A., Zabalza, V., Edwards, Z. I., Azalee Bostroem, K., Burke, D. J., Casey, A. R., Crawford, S. M., Dencheva, N., Ely, J., Jenness, T., Labrie, K., Lim, P. L., Pierfederici, F., Pontzen, A., Ptak, A., Refsdal, B., Servillat, M., and Streicher, O. (2013). Astropy: A community Python package for astronomy. *A&A*, 558:A33.

- Atwood, W. B., Abdo, A. A., Ackermann, M., Althouse, W., Anderson, B., Axelsson, M., Baldini, L., Ballet, J., Band, D. L., Barbiellini, G., and et al. (2009). The Large Area Telescope on the Fermi Gamma-Ray Space Telescope Mission. *ApJ*, 697:1071–1102.
- Backer, D. C., Kulkarni, S. R., Heiles, C., Davis, M. M., and Goss, W. M. (1982). A millisecond pulsar. *Nature*, 300:615–618.
- Bagnoli, T. and in’t Zand, J. J. M. (2015). Discovery of GRS 1915+105 variability patterns in the Rapid Burster. *MNRAS*, 450:L52–L56.
- Bagnoli, T., in’t Zand, J. J. M., D’Angelo, C. R., and Galloway, D. K. (2015). A population study of type II bursts in the Rapid Burster. *MNRAS*, 449:268–287.
- Bagnoli, T., in’t Zand, J. J. M., Galloway, D. K., and Watts, A. L. (2013). Indications for a slow rotator in the Rapid Burster from its thermonuclear bursting behaviour. *MNRAS*, 431:1947–1955.
- Barthelmy, S. D. (2000). Burst Alert Telescope (BAT) on the Swift MIDEX mission. In Flanagan, K. A. and Siegmund, O. H., editors, *X-Ray and Gamma-Ray Instrumentation for Astronomy XI*, volume 4140 of *Proc. SPIE*, pages 50–63.
- Bazzano, A., Bird, A. J., Kuulkers, E., Sidoli, L., Fiocchi, V. S. M., Natalucci, L., Tarana, A., Ubertini, P., Capitanio, F., Del Santo, M., Sabatini, S., Tavani, M., Bassani, L., Malizia, A., Drave, S. P., and Winkler, C. (2011). Announcement of INTEGRAL Galactic Plane monitoring program and detection of 2 new hard X-ray sources. *The Astronomer’s Telegram*, 3361.
- Bazzano, A., Stephen, J. B., Fiocchi, M., Bird, A. J., Bassani, L., Dean, A. J., Malizia, A., Ubertini, P., Lebrun, F., Walter, R., and Winkler, C. (2006). INTEGRAL IBIS Census of the Sky Beyond 100 keV. *ApJ*, 649:L9–L12.
- Belloni, T. and Hasinger, G. (1990). An atlas of aperiodic variability in HMXB. *A&A*, 230:103–119.
- Belloni, T., Klein-Wolt, M., Méndez, M., van der Klis, M., and van Paradijs, J. (2000). A model-independent analysis of the variability of GRS 1915+105. *A&A*, 355:271–290.
- Belloni, T., Méndez, M., King, A. R., van der Klis, M., and van Paradijs, J. (1997a). A Unified Model for the Spectral Variability in GRS 1915+105. *ApJ*, 488:L109–L112.
- Belloni, T., Méndez, M., King, A. R., van der Klis, M., and van Paradijs, J. (1997b). An Unstable Central Disk in the Superluminal Black Hole X-Ray Binary GRS 1915+105. *ApJ*, 479:L145–L148.
- Belloni, T., Psaltis, D., and van der Klis, M. (2002). A Unified Description of the Timing Features of Accreting X-Ray Binaries. *ApJ*, 572:392–406.
- Belloni, T. M. and Motta, S. E. (2016). Transient Black Hole Binaries. *ArXiv e-prints*.

- Bignami, G. F., Villa, G. E., Boella, G., Bonelli, G., Caraveo, P., Chiappetti, L., Quadrini, M. E., Di Cocco, G., Trifoglio, M., and Ubertini, P. (1990). European Photon Imaging Camera (EPIC) for X-ray astronomy. In Siegmund, O. H. W. and Hudson, H. S., editors, *EUV, X-ray, and Gamma-ray instrumentation for astronomy*, volume 1344 of *Proc. SPIE*, pages 144–153.
- Bildsten, L. and Brown, E. F. (1997). Thermonuclear Burning on the Accreting X-Ray Pulsar GRO J1744-28. *ApJ*, 477:897–904.
- Bildsten, L., Chakrabarty, D., Chiu, J., Finger, M. H., Koh, D. T., Nelson, R. W., Prince, T. A., Rubin, B. C., Scott, D. M., Stollberg, M., Vaughan, B. A., Wilson, C. A., and Wilson, R. B. (1997). Observations of Accreting Pulsars. *ApJS*, 113:367–408.
- Bird, A. J., Bazzano, A., Malizia, A., Fiocchi, M., Sguera, V., Bassani, L., Hill, A. B., Ubertini, P., and Winkler, C. (2016). The IBIS Soft Gamma-Ray Sky after 1000 Integral Orbits. *ApJS*, 223:15.
- Blackburn, J. K. (1995). FTOOLS: A FITS Data Processing and Analysis Software Package. In Shaw, R. A., Payne, H. E., and Hayes, J. J. E., editors, *Astronomical Data Analysis Software and Systems IV*, volume 77 of *Astronomical Society of the Pacific Conference Series*, page 367.
- Bogdanov, S., Archibald, A. M., Bassa, C., Deller, A. T., Halpern, J. P., Heald, G., Hessels, J. W. T., Janssen, G. H., Lyne, A. G., Moldón, J., Paragi, Z., Patruno, A., Perera, B. B. P., Stappers, B. W., Tendulkar, S. P., D’Angelo, C. R., and Wijnands, R. (2015). Coordinated X-Ray, Ultraviolet, Optical, and Radio Observations of the PSR J1023+0038 System in a Low-mass X-Ray Binary State. *ApJ*, 806:148.
- Bogdanov, S. and Halpern, J. P. (2015). Identification of the High-energy Gamma-Ray Source 3FGL J1544.6-1125 as a Transitional Millisecond Pulsar Binary in an Accreting State. *ApJ*, 803:L27.
- Boldt, E. (1987). The cosmic X-ray background. In Hewitt, A., Burbidge, G., and Fang, L. Z., editors, *Observational Cosmology*, volume 124 of *IAU Symposium*, pages 611–615.
- Bradt, H. V., Rothschild, R. E., and Swank, J. H. (1993). X-ray timing explorer mission. *A&AS*, 97:355–360.
- Bradt, H. V., Swank, J. H., and Rothschild, R. E. (1990). The X-ray Timing Explorer. *Advances in Space Research*, 10:297–310.
- Burrows, D. N., Hill, J. E., Nousek, J. A., Wells, A. A., Short, A. T., Ambrosi, R. M., Chincarini, G., Citterio, O., and Tagliaferri, G. (2003). Swift x-ray telescope (XRT). In Truemper, J. E. and Tananbaum, H. D., editors, *X-Ray and Gamma-Ray Telescopes and Instruments for Astronomy*, volume 4851 of *Proc. SPIE*, pages 1320–1325.

- Campana, S., Colpi, M., Mereghetti, S., Stella, L., and Tavani, M. (1998). The neutron stars of Soft X-ray Transients. *A&A Rev.*, 8:279–316.
- Campana, S., Stella, L., Mereghetti, S., and de Martino, D. (2017). A universal relation for the propeller mechanisms in magnetic rotating stars at different scales. *ArXiv e-prints*.
- Capitanio, F., Del Santo, M., Bozzo, E., Ferrigno, C., De Cesare, G., and Paizis, A. (2012). The peculiar 2011 outburst of the black hole candidate IGR J17091-3624, a GRS 1915+105-like source? *MNRAS*, 422:3130–3141.
- Castro-Tirado, A. J., Brandt, S., and Lund, N. (1992). GRS 1915+105. *IAU Circ.*, 5590.
- Chakrabarty, D., Bildsten, L., Finger, M. H., Grunsfeld, J. M., Koh, D. T., Nelson, R. W., Prince, T. A., Vaughan, B. A., and Wilson, R. B. (1997a). On the Correlation of Torque and Luminosity in GX 1+4. *ApJ*, 481:L101–L105.
- Chakrabarty, D., Bildsten, L., Grunsfeld, J. M., Koh, D. T., Prince, T. A., Vaughan, B. A., Finger, M. H., Scott, D. M., and Wilson, R. B. (1997b). Torque Reversal and Spin-down of the Accretion-powered Pulsar 4U 1626-67. *ApJ*, 474:414–425.
- Chakrabarty, D., Jonker, P. G., and Markwardt, C. B. (2014). Chandra Localization and Detection of a Burst and Pulsations from GRO J1744-28. *The Astronomer’s Telegram*, 5895.
- Chen, X., Swank, J. H., and Taam, R. E. (1996). The Pattern of Correlated X-ray Timing and Spectral Behavior in GRS 1915+105. In *American Astronomical Society Meeting Abstracts*, volume 28 of *Bulletin of the American Astronomical Society*, page 1315.
- Cole, D. M., Vanden Berk, D. E., Sevenson, S. A., Miller, M. C., Quashnock, J. M., Nichol, R. C., Lamb, D. Q., Hurley, K., Blanco, P., Lidman, C., and Glazebrook, K. (1997). Optical/Near-Infrared Observations of GRO J1744-28. *ApJ*, 480:377–382.
- Court, J. (2017). jmcourt/pantheon: Zenodo release.
- Court, J. M. C., Altamirano, D., Pereyra, M., Boon, C. M., Yamaoka, K., Belloni, T., Wijnands, R., and Pahari, M. (2017). An atlas of exotic variability in IGR J17091-3624: a comparison with GRS 1915+105. *MNRAS*, 468:4748–4771.
- Courvoisier, T. J.-L., Walter, R., Beckmann, V., Dean, A. J., Dubath, P., Hudec, R., Kretschmar, P., Mereghetti, S., Montmerle, T., Mowlavi, N., Paltani, S., Preite Martinez, A., Produit, N., Staubert, R., Strong, A. W., Swings, J.-P., Westergaard, N. J., White, N., Winkler, C., and Zdziarski, A. A. (2003). The INTEGRAL Science Data Centre (ISDC). *A&A*, 411:L53–L57.
- D’Ai, A., Di Salvo, T., Iaria, R., García, J. A., Sanna, A., Pintore, F., Riggio, A., Burderi, L., Bozzo, E., Dauser, T., Matranga, M., Galiano, C. G., and Robba, N. R. (2015). GRO J1744-28: an intermediate B-field pulsar in a low-mass X-ray binary. *MNRAS*, 449:4288–4303.

- Daigne, F., Goldoni, P., Ferrando, P., Goldwurm, A., Decourchelle, A., and Warwick, R. S. (2002). XMM-Newton observation of the bursting pulsar GRO J1744-28 in quiescence. *A&A*, 386:531–534.
- D’Amico, F., Heindl, W. A., Rothschild, R. E., and Gruber, D. E. (2001). High-Energy X-Ray Timing Experiment Detections of Hard X-Ray Tails in Scorpius X-1. *ApJ*, 547:L147–L150.
- De Martino, D., Belloni, T., Falanga, M., Papitto, A., Motta, S., Pellizzoni, A., Evangelista, Y., Piano, G., Masetti, N., Bonnet-Bidaud, J.-M., Mouchet, M., Mukai, K., and Possenti, A. (2013). X-ray follow-ups of XSS J12270-4859: a low-mass X-ray binary with gamma-ray Fermi-LAT association. *A&A*, 550:A89.
- Degenaar, N., Miller, J. M., Harrison, F. A., Kennea, J. A., Kouveliotou, C., and Younes, G. (2014). High-resolution X-Ray Spectroscopy of the Bursting Pulsar GRO J1744-28. *ApJ*, 796:L9.
- Degenaar, N., Wijnands, R., Cackett, E. M., Homan, J., in’t Zand, J. J. M., Kuulkers, E., Maccarone, T. J., and van der Klis, M. (2012). A four-year XMM-Newton/Chandra monitoring campaign of the Galactic centre: analysing the X-ray transients. *A&A*, 545:A49.
- den Herder, J.-W., Aarts, H. J., van den Berg, M. L., Bixler, J. V., den Boggende, A. J., Branduardi-Raymont, G., Brinkman, A. C., Decker, T. A., Dubbeldam, L., Hailey, C. J., Jansen, F. A., Kahn, S. M., de Korte, P. A., Mauche, C. W., Montesanti, R. C., Paerels, F. B., Spruijt, H., Thomsen, K., Verhoeve, P., and Zehnder, A. (1994). Reflection grating spectrometer onboard the ESA x-ray multi-mirror (XMM) mission. In Cerutti-Maori, M. G. and Roussel, P., editors, *Space Optics 1994: Earth Observation and Astronomy*, volume 2209 of *Proc. SPIE*, pages 451–462.
- Di Salvo, T., Robba, N. R., Iaria, R., Stella, L., Burderi, L., and Israel, G. L. (2001a). Detection of a Hard Tail in the X-Ray Spectrum of the Z Source GX 349+2. *ApJ*, 554:49–55.
- Di Salvo, T., Stella, L., Robba, N. R., Burderi, L., and van der Klis, M. (2001b). The discovery of a hard X-ray component in the horizontal branch spectrum of the Z source GX 17+2. In Gimenez, A., Reglero, V., and Winkler, C., editors, *Exploring the Gamma-Ray Universe*, volume 459 of *ESA Special Publication*, pages 341–344.
- Done, C., Wardziński, G., and Gierliński, M. (2004). GRS 1915+105: the brightest Galactic black hole. *MNRAS*, 349:393–403.
- Doroshenko, R., Santangelo, A., Doroshenko, V., Suleimanov, V., and Piraino, S. (2015). BeppoSAX observations of GRO J1744-28: cyclotron line detection and the softening of the burst spectra. *MNRAS*, 452:2490–2499.

- Doxsey, R., Bradt, H., Johnston, M., Gursky, H., Schwartz, D. A., and Schwarz, J. (1978). Position for the rapid burster MXB 1730-335 determined with the scanning modulation collimator on HEAO 1. *ApJ*, 221:L53–L55.
- Drave, S. P., Fiocchi, M., Sguera, V., Bazzano, A., Bird, A. J., Sidoli, L., and Kuulker, E. (2012). A possible state change in the black-hole candidate IGR J17091-3624. *The Astronomer's Telegram*, 3916.
- Eckert, D., Del Santo, M., Bazzano, A., Watanabe, K., Paizis, A., Bozzo, E., Ferrigno, C., Caballero, I., Sidoli, L., and Kuiper, L. (2013). IGR J18245-2452: a new hard X-ray transient discovered by INTEGRAL. *The Astronomer's Telegram*, 4925.
- Evans, P. A., Beardmore, A. P., Page, K. L., Osborne, J. P., O'Brien, P. T., Willingale, R., Starling, R. L. C., Burrows, D. N., Godet, O., Vetere, L., Racusin, J., Goad, M. R., Wiersema, K., Angelini, L., Capalbi, M., Chincarini, G., Gehrels, N., Kennea, J. A., Margutti, R., Morris, D. C., Mountford, C. J., Pagani, C., Perri, M., Romano, P., and Tanvir, N. (2009). Methods and results of an automatic analysis of a complete sample of Swift-XRT observations of GRBs. *MNRAS*, 397:1177–1201.
- Evans, P. A., Beardmore, A. P., Page, K. L., Tyler, L. G., Osborne, J. P., Goad, M. R., O'Brien, P. T., Vetere, L., Racusin, J., Morris, D., Burrows, D. N., Capalbi, M., Perri, M., Gehrels, N., and Romano, P. (2007). An online repository of Swift/XRT light curves of γ -ray bursts. *A&A*, 469:379–385.
- Fender, R. (2006). *Jets from X-ray binaries*, pages 381–419.
- Fender, R. and Belloni, T. (2004). GRS 1915+105 and the Disc-Jet Coupling in Accreting Black Hole Systems. *ARA&A*, 42:317–364.
- Ferrigno, C., Bozzo, E., Papitto, A., Rea, N., Pavan, L., Campana, S., Wieringa, M., Filipović, M., Falanga, M., and Stella, L. (2014). Hiccup accretion in the swinging pulsar IGR J18245-2452. *A&A*, 567:A77.
- Finger, M. H., Koh, D. T., Nelson, R. W., Prince, T. A., Vaughan, B. A., and Wilson, R. B. (1996a). Discovery of hard X-ray pulsations from the transient source GRO J1744 - 28. *Nature*, 381:291–293.
- Finger, M. H., Wilson, R. B., Harmon, B. A., Hagedon, K., and Prince, T. A. (1996b). GRO J1744-28. *IAU Circ.*, 6285.
- Fiocchi, M. T., Natalucci, L., and GPS Team (2012). The INTEGRAL Galactic Plane Scanning. In *Proceedings of "An INTEGRAL view of the high-energy sky (the first 10 years)" - 9th INTEGRAL Workshop and celebration of the 10th anniversary of the launch (INTEGRAL 2012). 15-19 October 2012. Bibliotheque Nationale de France, Paris, France. Published online at <http://pos.sissa.it/cgi-bin/reader/conf.cgi?confid=176>, id.82, page 82.*

- Fishman, G. J., Kouveliotou, C., van Paradijs, J., Harmon, B. A., Paciesas, W. S., Briggs, M. S., Kommers, J., and Lewin, W. H. G. (1995). Galactic Center. *IAU Circ.*, 6272.
- Frank, J., King, A., and Raine, D. J. (2002). *Accretion Power in Astrophysics: Third Edition*.
- Fruscione, A., McDowell, J. C., Allen, G. E., Brickhouse, N. S., Burke, D. J., Davis, J. E., Durham, N., Elvis, M., Galle, E. C., Harris, D. E., Huenemoerder, D. P., Houck, J. C., Ishibashi, B., Karovska, M., Nicastro, F., Noble, M. S., Nowak, M. A., Primini, F. A., Siemiginowska, A., Smith, R. K., and Wise, M. (2006). CIAO: Chandra's data analysis system. In *Society of Photo-Optical Instrumentation Engineers (SPIE) Conference Series*, volume 6270 of *Proc. SPIE*, page 62701V.
- Galloway, D. K. and in't Zand, J. J. M. (2010). Type-II bursts from the new Terzan 5 transient: a GRO J1744-28 analogue? *The Astronomer's Telegram*, 3000.
- Galloway, D. K., Munro, M. P., Hartman, J. M., Psaltis, D., and Chakrabarty, D. (2008). Thermonuclear (Type I) X-Ray Bursts Observed by the Rossi X-Ray Timing Explorer. *ApJS*, 179:360–422.
- Gehrels, N. (2004). The Swift Gamma-Ray Burst Mission. In Schoenfelder, V., Lichti, G., and Winkler, C., editors, *5th INTEGRAL Workshop on the INTEGRAL Universe*, volume 552 of *ESA Special Publication*, page 777.
- Gehrels, N., Chipman, E., and Kniffen, D. (1994). The Compton Gamma Ray Observatory. *ApJS*, 92:351–362.
- Ghosh, A. and Chakrabarti, S. K. (2014). Periods of two enigmatic black hole candidates GRS 1915+105 and IGR J17091-3624. *ArXiv e-prints*.
- Giles, A. B., Swank, J. H., Jahoda, K., Zhang, W., Strohmayer, T., Stark, M. J., and Morgan, E. H. (1996). The Main Characteristics of GRO J1744-28 Observed by the Proportional Counter Array Experiment on the Rossi X-Ray Timing Explorer. *ApJ*, 469:L25.
- Gimenez, A. and Mas-Hesse, J. M. (1998). Optical monitoring camera on board the ESA high-energy mission INTEGRAL. In Doty, F. P. and Hoover, R. B., editors, *Hard X-Ray and Gamma-Ray Detector Physics and Applications*, volume 3446 of *Proc. SPIE*, pages 257–265.
- Giorgini, J. D., Yeomans, D. K., Chamberlin, A. B., Chodas, P. W., Jacobson, R. A., Keesey, M. S., Lieske, J. H., Ostro, S. J., Standish, E. M., and Wimberly, R. N. (1997). JPL's On-Line Solar System Ephemeris and Data Service. In Bietenholz, M. F., Bartel, N., Rupen, M. P., Beasley, A. J., Graham, D. A., Altunin, V. I., Venturi, T., Umana, G., and Conway, J. E., editors, *Bulletin of the American Astronomical Society*, volume 29 of *Bulletin of the American Astronomical Society*, page 1099.

- Gosling, A. J., Bandyopadhyay, R. M., Miller-Jones, J. C. A., and Farrell, S. A. (2007). GRO J1744-28, search for the counterpart: infrared photometry and spectroscopy. *MNRAS*, 380:1511–1520.
- Graessle, D. E., Evans, I. N., Glotfelty, K., He, X. H., Evans, J. D., Rots, A. H., Fabbiano, G., and Brissenden, R. J. (2006). The Chandra X-ray Observatory calibration database (CalDB): building, planning, and improving. In *Society of Photo-Optical Instrumentation Engineers (SPIE) Conference Series*, volume 6270 of *Proc. SPIE*, page 62701X.
- Gruber, D. E., Blanco, P. R., Heindl, W. A., Pelling, M. R., Rothschild, R. E., and Hink, P. L. (1996). The high energy X-ray timing experiment on XTE. *A&AS*, 120:641–644.
- Hannikainen, D. C., Hjalmarsdotter, L., Rodriguez, J., Vilhu, O., Zdziarski, A. A., and Belloni, T. (2007). Identifying a New Class of Variability in GRS 1915+105. In *ESA Special Publication*, volume 622 of *ESA Special Publication*, page 353.
- Hayakawa, S. (1985). X-rays from accreting neutron stars. *Phys. Rep.*, 121:317–406.
- Heidke, P. (1926). Berechnung des erfolges und der gute der windstarkvorhersagen im sturmwarnungsdienst. *Geogr. Ann.*, 8:301349.
- Hill, A. B., Szostek, A., Corbel, S., Camilo, F., Corbet, R. H. D., Dubois, R., Dubus, G., Edwards, P. G., Ferrara, E. C., Kerr, M., Koerding, E., Kozieł, D., and Stawarz, Ł. (2011). The bright unidentified γ -ray source 1FGL J1227.9-4852: can it be associated with a low-mass X-ray binary? *MNRAS*, 415:235–243.
- Hirose, S., Krolik, J. H., and Blaes, O. (2009). Radiation-Dominated Disks are Thermally Stable. *ApJ*, 691:16–31.
- Hoffman, J. A., Marshall, H. L., and Lewin, W. H. G. (1978). Dual character of the rapid burster and a classification of X-ray bursts. *Nature*, 271:630–633.
- Hunter, J. D. (2007). Matplotlib: A 2d graphics environment. *Computing In Science & Engineering*, 9(3):90–95.
- Huppenkothen, D., Heil, L. M., Hogg, D. W., and Mueller, A. (2017). Using machine learning to explore the long-term evolution of GRS 1915+105. *MNRAS*, 466:2364–2377.
- Huppenkothen, D., Younes, G., Ingram, A., Kouveliotou, C., Göğüş, E., Bachetti, M., Sánchez-Fernández, C., Chenevez, J., Motta, S., van der Klis, M., Granot, J., Gehrels, N., Kuulkers, E., Tomsick, J. A., and Walton, D. J. (2016). Detection of Very Low-Frequency Quasi-Periodic Oscillations in the 2015 Outburst of V404 Cygni. *ArXiv e-prints*.
- Iaria, R., Gambino, A. F., Di Salvo, T., Burderi, L., Matranga, M., Riggio, A., Sanna, A., Scarano, F., and D’Ai, A. (2018). A possible solution of the puzzling variation of the orbital period of MXB 1659-298. *MNRAS*, 473:3490–3499.

- Ibarra, A., Calle, I., Gabriel, C., Salgado, J., and Osuna, P. (2009). XMM-Newton Science Analysis Software: How to Bring New Technologies to Long-life Satellite Missions. In Bohlender, D. A., Durand, D., and Dowler, P., editors, *Astronomical Data Analysis Software and Systems XVIII*, volume 411 of *Astronomical Society of the Pacific Conference Series*, page 322.
- Ibragimov, A. and Poutanen, J. (2009). Accreting millisecond pulsar SAX J1808.4-3658 during its 2002 outburst: evidence for a receding disc. *MNRAS*, 400:492–508.
- Icke, V. (1979). Disk accretion in a soft potential well. *A&A*, 78:21–24.
- Illarionov, A. F. and Sunyaev, R. A. (1975). Why the Number of Galactic X-ray Stars Is so Small? *A&A*, 39:185.
- Irwin, A. W., Campbell, B., Morbey, C. L., Walker, G. A. H., and Yang, S. (1989). Long-period radial-velocity variations of Arcturus. *PASP*, 101:147–159.
- Iyer, N., Nandi, A., and Mandal, S. (2015a). Determination of the Mass of IGR J17091-3624 from "Spectro-temporal" Variations during the Onset Phase of the 2011 Outburst. *ApJ*, 807:108.
- Iyer, N., Nandi, A., and Mandal, S. (2015b). Estimating the mass of IGR J17091-3624: statistical challenges and methods. In *Astronomical Society of India Conference Series*, volume 12 of *Astronomical Society of India Conference Series*.
- Jahoda, K., Markwardt, C. B., Radeva, Y., Rots, A. H., Stark, M. J., Swank, J. H., Strohmayer, T. E., and Zhang, W. (2006). Calibration of the Rossi X-Ray Timing Explorer Proportional Counter Array. *ApJS*, 163:401–423.
- Jahoda, K., Swank, J. H., Giles, A. B., Stark, M. J., Strohmayer, T., Zhang, W., and Morgan, E. H. (1996). In-orbit performance and calibration of the Rossi X-ray Timing Explorer (RXTE) Proportional Counter Array (PCA). In Siegmund, O. H. and Gummin, M. A., editors, *EUV, X-Ray, and Gamma-Ray Instrumentation for Astronomy VII*, volume 2808 of *Proc. SPIE*, pages 59–70.
- Janiuk, A. and Czerny, B. (2005). Time-delays between the soft and hard X-ray bands in GRS 1915+105. *MNRAS*, 356:205–216.
- Janiuk, A., Czerny, B., and Siemiginowska, A. (2000). Radiation Pressure Instability as a Variability Mechanism in the Microquasar GRS 1915+105. *ApJ*, 542:L33–L36.
- Jansen, F., Lumb, D., Altieri, B., Clavel, J., Ehle, M., Erd, C., Gabriel, C., Guainazzi, M., Gondoin, P., Much, R., Munoz, R., Santos, M., Schartel, N., Texier, D., and Vacanti, G. (2001). XMM-Newton observatory. I. The spacecraft and operations. *A&A*, 365:L1–L6.
- Johnson, T. J., Ray, P. S., Roy, J., Cheung, C. C., Harding, A. K., Pletsch, H. J., Fort, S., Camilo, F., Deneva, J., Bhattacharyya, B., Stappers, B. W., and Kerr, M. (2015).

Discovery of Gamma-Ray Pulsations from the Transitional Redback PSR J1227-4853. *ApJ*, 806:91.

Jones, E., Oliphant, T., Peterson, P., et al. (2001). SciPy: Open source scientific tools for Python.

Kennea, J. A. and Capitanio, F. (2007). Swift/XRT Observations of IGR J17091-3624 and IGR J17098-3628. *The Astronomer's Telegram*, 1140.

Kennea, J. A., Kouveliotou, C., and Younes, G. (2014). GRO J1744-28: Swift XRT confirmation of outburst. *The Astronomer's Telegram*, 5845.

Kenney, J. (1939). *Mathematics of Statistics*. Number v. 1 in Mathematics of Statistics. D. Van Nostrand Company, Incorporated.

Kenter, A. T., Chappell, J. H., Kraft, R. P., Meehan, G. R., Murray, S. S., Zombeck, M. V., Hole, K. T., Juda, M., Donnelly, R. H., Patnaude, D., Pease, D. O., Wilton, C., Zhao, P., Austin, G. K., Fraser, G. W., Pearson, J. F., Lees, J. E., Brunton, A. N., Barbera, M., Collura, A., and Serio, S. (2000). In-flight performance and calibration of the Chandra high-resolution camera imager (HRC-I). In Truemper, J. E. and Aschenbach, B., editors, *X-Ray Optics, Instruments, and Missions III*, volume 4012 of *Proc. SPIE*, pages 467–492.

King, A. L., Miller, J. M., Raymond, J., Fabian, A. C., Reynolds, C. S., Kallman, T. R., Maitra, D., Cackett, E. M., and Rupen, M. P. (2012). An Extreme X-Ray Disk Wind in the Black Hole Candidate IGR J17091-3624. *ApJ*, 746:L20.

King, A. L., Miller, J. M., Raymond, J., Reynolds, M. T., and Morningstar, W. (2015). High-resolution Chandra HETG Spectroscopy of V404 Cygni in Outburst. *ApJ*, 813:L37.

Klein-Wolt, M., Fender, R. P., Pooley, G. G., Belloni, T., Migliari, F., S., Morgan, E. H., and van der Klis, M. (2002). Hard X-ray states and radio emission in GRS 1915+105. *MNRAS*, 331:745–764.

Kok, C. (2000). *On the Behaviour of a Few Popular Verification Scores in Yes No Forecasting*. Scientific report. Koninklijk Nederlands Meteorologisch Insituut.

Kommers, J. M., Fox, D. W., Lewin, W. H. G., Rutledge, R. E., van Paradijs, J., and Kouveliotou, C. (1997). Postburst Quasi-periodic Oscillations from GRO J1744-28 and from the Rapid Burster. *ApJ*, 482:L53–L56.

Kouveliotou, C., van Paradijs, J., Fishman, G. J., Briggs, M. S., Kommers, J., Harmon, B. A., Meegan, C. A., and Lewin, W. H. G. (1996). A new type of transient high-energy source in the direction of the Galactic Centre. *Nature*, 379:799–801.

Koyama, K., Tsunemi, H., Dotani, T., Bautz, M. W., Hayashida, K., Tsuru, T. G., Matsumoto, H., Ogawara, Y., Ricker, G. R., Doty, J., Kissel, S. E., Foster, R., Nakajima, H., Yamaguchi, H., Mori, H., Sakano, M., Hamaguchi, K., Nishiuchi, M., Miyata, E.,

- Torii, K., Namiki, M., Katsuda, S., Matsuura, D., Miyauchi, T., Anabuki, N., Tawa, N., Ozaki, M., Murakami, H., Maeda, Y., Ichikawa, Y., Prigozhin, G. Y., Boughan, E. A., Lamarr, B., Miller, E. D., Burke, B. E., Gregory, J. A., Pillsbury, A., Bamba, A., Hiraga, J. S., Senda, A., Katayama, H., Kitamoto, S., Tsujimoto, M., Kohmura, T., Tsuboi, Y., and Awaki, H. (2007). X-Ray Imaging Spectrometer (XIS) on Board Suzaku. *PASJ*, 59:23–33.
- Kraft, R. P., Chappell, J. H., Kenter, A. T., Meehan, G. R., Murray, S. S., Zombeck, M. V., Donnelly, R. H., Drake, J. J., Johnson, C. O., Juda, M., Patnaude, D., Pease, D. O., Ratzlaff, P. W., Wargelin, B. J., Zhao, P., Austin, G. K., Fraser, G. W., Pearson, J. F., Lees, J. E., Brunton, A. N., Barbera, M., Collura, A., and Serio, S. (2000). In-flight performance and calibration of the Chandra high-resolution camera spectroscopic readout (HRC-S). In Truemper, J. E. and Aschenbach, B., editors, *X-Ray Optics, Instruments, and Missions III*, volume 4012 of *Proc. SPIE*, pages 493–517.
- Kreykenbohm, I., Wilms, J., Kretschmar, P., Torrejón, J. M., Pottschmidt, K., Hanke, M., Santangelo, A., Ferrigno, C., and Staubert, R. (2008). High variability in Vela X-1: giant flares and off states. *A&A*, 492:511–525.
- Krimm, H. A., Barthelmy, S. D., Baumgartner, W., Cummings, J., Fenimore, E., Gehrels, N., Kennea, J. A., Markwardt, C. B., Palmer, D., Sakamoto, T., Skinner, G., Stamatikos, M., Tueller, J., and Ukwatta, T. (2011). Swift/BAT reports renewed activity from IGR J17091-3624. *The Astronomer’s Telegram*, 3144.
- Krimm, H. A., Holland, S. T., Corbet, R. H. D., Pearlman, A. B., Romano, P., Kennea, J. A., Bloom, J. S., Barthelmy, S. D., Baumgartner, W. H., Cummings, J. R., Gehrels, N., Lien, A. Y., Markwardt, C. B., Palmer, D. M., Sakamoto, T., Stamatikos, M., and Ukwatta, T. N. (2013). The Swift/BAT Hard X-Ray Transient Monitor. *ApJS*, 209:14.
- Krimm, H. A. and Kennea, J. A. (2011). Swift/XRT Observations Confirm that IGR J17091-3624 is in Outburst. *The Astronomer’s Telegram*, 3148:1.
- Krivonos, R., Tsygankov, S., Lutovinov, A., Revnivtsev, M., Churazov, E., and Sunyaev, R. (2015). INTEGRAL 11-year hard X-ray survey above 100 keV. *MNRAS*, 448:3766–3774.
- Kuulkers, E., Homan, J., van der Klis, M., Lewin, W. H. G., and Méndez, M. (2002). X-ray bursts at extreme mass accretion rates from GX 17+2. *A&A*, 382:947–973.
- Kuulkers, E., Lutovinov, A., Parmar, A., Capitanio, F., Mowlavi, N., and Hermsen, W. (2003). Igr J17091-3624. *The Astronomer’s Telegram*, 149.
- Kuulkers, E., Shaw, S., Paizis, A., Mowlavi, N., Courvoisier, T., Ebisawa, K., Kretschmar, P., Markwardt, C., Oosterbroek, T., Orr, A., and Wijnands, R. (2005). Announcement of INTEGRAL Galactic Bulge monitoring program and (re)brightening of GRO J1655-40. *The Astronomer’s Telegram*, 438.

- Kuulkers, E., Shaw, S. E., Paizis, A., Chenevez, J., Brandt, S., Courvoisier, T. J.-L., Domingo, A., Ebisawa, K., Kretschmar, P., Markwardt, C. B., Mowlavi, N., Oosterbroek, T., Orr, A., Rísquez, D., Sanchez-Fernandez, C., and Wijnands, R. (2007). The INTEGRAL Galactic bulge monitoring program: the first 1.5 years. *A&A*, 466:595–618.
- Leahy, D. A., Darbro, W., Elsner, R. F., Weisskopf, M. C., Kahn, S., Sutherland, P. G., and Grindlay, J. E. (1983). On searches for pulsed emission with application to four globular cluster X-ray sources - NGC 1851, 6441, 6624, and 6712. *ApJ*, 266:160–170.
- Lebrun, F., Blondel, C., Fondeur, I., Goldwurm, A., Laurent, P., and Leray, J. P. (1996). ISGRI: a CdTe array imager for INTEGRAL. In Ramsey, B. D. and Parnell, T. A., editors, *Gamma-Ray and Cosmic-Ray Detectors, Techniques, and Missions*, volume 2806 of *Proc. SPIE*, pages 258–268.
- Leiter, D. (1983). Electron-positron processes and spectral evolution in black hole accretion disk dynamo models for AGN sources of the cosmic X-ray and gamma ray backgrounds. In Burns, M. L., Harding, A. K., and Ramaty, R., editors, *Positron-Electron Pairs in Astrophysics*, volume 101 of *American Institute of Physics Conference Series*, pages 337–342.
- Lemiere, A., Terrier, R., Jouvin, L., Marandon, V., and Khelifi, B. (2015). Study of the VHE diffuse emission in the central 200 pc of our Galaxy with H.E.S.S. In *34th International Cosmic Ray Conference (ICRC2015)*, volume 34 of *International Cosmic Ray Conference*, page 838.
- Levine, A. M., Bradt, H., Cui, W., Jernigan, J. G., Morgan, E. H., Remillard, R., Shirey, R. E., and Smith, D. A. (1996). First Results from the All-Sky Monitor on the Rossi X-Ray Timing Explorer. *ApJ*, 469:L33.
- Lewin, W. H. G., Doty, J., Clark, G. W., Rappaport, S. A., Bradt, H. V. D., Doxsey, R., Hearn, D. R., Hoffman, J. A., Jernigan, J. G., Li, F. K., Mayer, W., McClintock, J., Primini, F., and Richardson, J. (1976). The discovery of rapidly repetitive X-ray bursts from a new source in Scorpius. *ApJ*, 207:L95–L99.
- Lewin, W. H. G., Ricker, G. R., and McClintock, J. E. (1971). X-Rays from a New Variable Source GX 1+4. *ApJ*, 169:L17.
- Lewin, W. H. G., Rutledge, R. E., Kommers, J. M., van Paradijs, J., and Kouveliotou, C. (1996). A Comparison between the Rapid Burster and GRO J1744-28. *ApJ*, 462:L39.
- Lewin, W. H. G., van Paradijs, J., and Taam, R. E. (1993). X-Ray Bursts. *Space Sci. Rev.*, 62:223–389.
- Lewin, W. H. G., van Paradijs, J., and van der Klis, M. (1988). A review of quasi-periodic oscillations in low-mass X-ray binaries. *Space Sci. Rev.*, 46:273–378.

- Lightman, A. P. and Eardley, D. M. (1974). Black Holes in Binary Systems: Instability of Disk Accretion. *ApJ*, 187:L1.
- Lin, D., Remillard, R. A., and Homan, J. (2009). Spectral States of XTE J1701 - 462: Link Between Z and Atoll Sources. *ApJ*, 696:1257–1277.
- Linares, M., Kennea, J., Krimm, H., and Kouveliotou, C. (2014). Swift detects bursting activity from GRO J1744-28. *The Astronomer’s Telegram*, 5883.
- Liu, Q. Z., van Paradijs, J., and van den Heuvel, E. P. J. (2007). A catalogue of low-mass X-ray binaries in the Galaxy, LMC, and SMC (Fourth edition). *A&A*, 469:807–810.
- Lomb, N. R. (1976). Least-squares frequency analysis of unequally spaced data. *Ap&SS*, 39:447–462.
- Lubiński, P. (2009). Analysis of extremely low signal-to-noise ratio data from INTEGRAL/PICsIT. *A&A*, 496:557–576.
- Maccarone, T. J. (2003). Do X-ray binary spectral state transition luminosities vary? *A&A*, 409:697–706.
- Madsen, K. K., Forster, K., Grefenstette, B. W., Harrison, F. A., and Stern, D. (2017). Measurement of the Absolute Crab Flux with NuSTAR. *ApJ*, 841:56.
- Makishima, K., Maejima, Y., Mitsuda, K., Bradt, H. V., Remillard, R. A., Tuohy, I. R., Hoshi, R., and Nakagawa, M. (1986). Simultaneous X-ray and optical observations of GX 339-4 in an X-ray high state. *ApJ*, 308:635–643.
- Manchester, R. N., Hobbs, G. B., Teoh, A., and Hobbs, M. (2005). The Australia Telescope National Facility Pulsar Catalogue. *AJ*, 129:1993–2006.
- Markwardt, C. B., Swank, J. H., and Taam, R. E. (1999). Variable-Frequency Quasi-periodic Oscillations from the Galactic Microquasar GRS 1915+105. *ApJ*, 513:L37–L40.
- Marshall, H., Grindlay, J., and Weisskopf, M. (1979). Observations of the Rapid Burster (MXB1730-335) Using the EINSTEIN Observatory. In *Bulletin of the American Astronomical Society*, volume 11 of *Bulletin of the American Astronomical Society*, page 788.
- Masetti, N., D’Avanzo, P., Blagorodnova, N., and Palazzi, E. (2014). The near-infrared counterpart of GRO J1744-28. *The Astronomer’s Telegram*, 5999.
- Mason, K. O., Cropper, M. S., Hunt, R., Horner, S. D., Priedhorsky, W. C., Ho, C., Cordova, F. A., Jamar, C. A., and Antonello, E. (1996). XMM Optical/UV Monitor Telescope. In Siegmund, O. H. and Gummin, M. A., editors, *EUV, X-Ray, and Gamma-Ray Instrumentation for Astronomy VII*, volume 2808 of *Proc. SPIE*, pages 438–447.

- Massa, F., Massaro, E., Mineo, T., D'Ai, A., Feroci, M., Casella, P., and Belloni, T. (2013). The complex behaviour of the microquasar GRS 1915+105 in the ρ class observed with BeppoSAX. III. The hard X-ray delay and limit cycle mapping. *A&A*, 556:A84.
- Massaro, E., Ardito, A., Ricciardi, P., Massa, F., Mineo, T., and D'Ai, A. (2014a). Non-linear oscillator models for the X-ray bursting of the microquasar GRS 1915+105. *Ap&SS*, 352:699–714.
- Massaro, E., Ardito, A., Ricciardi, P., Massa, F., Mineo, T., and D'Ai, A. (2014b). Non-linear oscillator models for the X-ray bursting of the microquasar GRS 1915+105. *Ap&SS*, 352:699–714.
- Massaro, E., Ventura, G., Massa, F., Feroci, M., Mineo, T., Cusumano, G., Casella, P., and Belloni, T. (2010). The complex behaviour of the microquasar GRS 1915+105 in the ρ class observed with BeppoSAX. I. Timing analysis. *A&A*, 513:A21.
- McClintock, J. E. and Rappaport, S. A. (1985). Low-mass X-ray binaries. In Lamb, D. Q. and Patterson, J., editors, *Cataclysmic Variables and Low-Mass X-ray Binaries*, volume 113 of *Astrophysics and Space Science Library*, pages 61–77.
- McClintock, J. E. and Remillard, R. A. (2006). *Black hole binaries*, pages 157–213.
- Merloni, A. and Nayakshin, S. (2006). On the limit-cycle instability in magnetized accretion discs. *MNRAS*, 372:728–734.
- Miller, J. M., Reynolds, M., Kennea, J., King, A. L., and Tomsick, J. (2016). Renewed Activity in the Galactic Black Hole IGR J17091-3624. *The Astronomer's Telegram*, 8742.
- Miller, M. C., Lamb, F. K., and Psaltis, D. (1996). Sonic-Point Model of Kilohertz QPOs in LMXBs. In *American Astronomical Society Meeting Abstracts*, volume 28 of *Bulletin of the American Astronomical Society*, page 1329.
- Mineo, T., Massaro, E., D'Ai, A., Massa, F., Feroci, M., Ventura, G., Casella, P., Ferrigno, C., and Belloni, T. (2012). The complex behaviour of the microquasar GRS 1915+105 in the ρ class observed with BeppoSAX. II. Time-resolved spectral analysis. *A&A*, 537:A18.
- Mir, M. H., Misra, R., Pahari, M., Iqbal, N., and Ahmad, N. (2016). A model for the energy-dependent time-lag and rms of the heartbeat oscillations in GRS 1915+105. *MNRAS*, 457:2999–3005.
- Misner, C. W., Thorne, K. S., and Wheeler, J. A. (1973). *Gravitation*.
- Mitsuda, K., Bautz, M., Inoue, H., Kelley, R. L., Koyama, K., Kunieda, H., Makishima, K., Ogawara, Y., Petre, R., Takahashi, T., Tsunemi, H., White, N. E., Anabuki, N., Angelini, L., Arnaud, K., Awaki, H., Bamba, A., Boyce, K., Brown, G. V., Chan, K.-W., Cottam, J., Dotani, T., Doty, J., Ebisawa, K., Ezoe, Y., Fabian, A. C., Figueroa, E., Fujimoto, R.,

Fukazawa, Y., Furusho, T., Furuzawa, A., Gendreau, K., Griffiths, R. E., Haba, Y., Hamaguchi, K., Harrus, I., Hasinger, G., Hatsukade, I., Hayashida, K., Henry, P. J., Hiraga, J. S., Holt, S. S., Hornschemeier, A., Hughes, J. P., Hwang, U., Ishida, M., Ishisaki, Y., Isobe, N., Itoh, M., Iyomoto, N., Kahn, S. M., Kamae, T., Katagiri, H., Kataoka, J., Katayama, H., Kawai, N., Kilbourne, C., Kinugasa, K., Kissel, S., Kitamoto, S., Kohama, M., Kohmura, T., Kokubun, M., Kotani, T., Kotoku, J., Kubota, A., Madejski, G. M., Maeda, Y., Makino, F., Markowitz, A., Matsumoto, C., Matsumoto, H., Matsuoka, M., Matsushita, K., McCammon, D., Mihara, T., Misaki, K., Miyata, E., Mizuno, T., Mori, K., Mori, H., Morii, M., Moseley, H., Mukai, K., Murakami, H., Murakami, T., Mushotzky, R., Nagase, F., Namiki, M., Negoro, H., Nakazawa, K., Nousek, J. A., Okajima, T., Ogasaka, Y., Ohashi, T., Oshima, T., Ota, N., Ozaki, M., Ozawa, H., Parmar, A. N., Pence, W. D., Porter, F. S., Reeves, J. N., Ricker, G. R., Sakurai, I., Sanders, W. T., Senda, A., Serlemitsos, P., Shibata, R., Soong, Y., Smith, R., Suzuki, M., Szymkowiak, A. E., Takahashi, H., Tamagawa, T., Tamura, K., Tamura, T., Tanaka, Y., Tashiro, M., Tawara, Y., Terada, Y., Terashima, Y., Tomida, H., Torii, K., Tsuboi, Y., Tsujimoto, M., Tsuru, T. G., Turner, M. J. L., Ueda, Y., Ueno, S., Ueno, M., Uno, S., Urata, Y., Watanabe, S., Yamamoto, N., Yamaoka, K., Yamasaki, N. Y., Yamashita, K., Yamauchi, M., Yamauchi, S., Yaqoob, T., Yonetoku, D., and Yoshida, A. (2007). The X-Ray Observatory Suzaku. *PASJ*, 59:1–7.

Morgan, E. H., Remillard, R. A., and Greiner, J. (1997). RXTE Observations of QPOs in the Black Hole Candidate GRS 1915+105. *ApJ*, 482:993–1010.

Murray, S. S., Chappell, J. H., Elvis, M. S., Forman, W. R., and Grindlay, J. E. (1987). The AXAF high resolution camera (HRC) and its use for observations of distant clusters of galaxies. *Astrophysical Letters and Communications*, 26:113–125.

Nayakshin, S., Rappaport, S., and Melia, F. (2000). Time-dependent Disk Models for the Microquasar GRS 1915+105. *ApJ*, 535:798–814.

Negoro, H., Sugizaki, M., Krimm, H. A., Kennea, J. A., Ueno, S., Tomida, H., Nakahira, S., Kimura, M., Ishikawa, M., Nakagawa, Y. E., Mihara, T., Serino, M., Morii, M., Sugimoto, J., Takagi, T., Yoshikawa, A., Matsuoka, M., Kawai, N., Usui, R., Ishikawa, K., Yoshii, T., Tachibana, Y., Yoshida, A., Sakamoto, T., Nakano, Y., Kawakubo, Y., Ohtsuki, H., Tsunemi, H., Sasaki, M., Uchida, D., Nakajima, M., Sakakibara, H., Fukushima, K., Onodera, T., Suzuki, K., Ueda, Y., Shidatsu, M., Kawamuro, T., Hori, T., Tsuboi, Y., Higa, M., Kawagoe, A., Yamauchi, M., Yoshidome, K., Ogawa, Y., Yamada, H., Morooka, Y., and Yamaoka, K. (2014). MAXI/GSC and Swift/BAT detection of enhanced hard X-ray emission from the Galactic center region, renewed activity of GRO J1744-28 ? *The Astronomer’s Telegram*, 5790.

Negri, L. H. and Vestri, C. (2017). lucashn/peakutils: v1.1.0.

Neilsen, J., Remillard, R. A., and Lee, J. C. (2011). The Physics of the ”Heartbeat” State of GRS 1915+105. *ApJ*, 737:69.

- Neilsen, J., Remillard, R. A., and Lee, J. C. (2012). Radiation Pressure and Mass Ejection in ρ -like States of GRS 1915+105. *ApJ*, 750:71.
- Nobili, L. (2003). A Disk-Jet Interaction Model for the X-Ray Variability in Microquasars. *ApJ*, 582:954–958.
- Nousek, J. A., Garmire, G. P., Ricker, G. R., Collins, S. A., and Reigler, G. R. (1987). The AXAF CCD Imaging Spectrometer Experiment (ACIS). *Astrophysical Letters and Communications*, 26:35–41.
- Novikov, I. D. and Thorne, K. S. (1973). Astrophysics of black holes. In Dewitt, C. and Dewitt, B. S., editors, *Black Holes (Les Astres Occlus)*, pages 343–450.
- Paciesas, W. S., Harmon, B. A., Fishman, G. J., Zhang, S. N., and Robinson, C. R. (1996). Galactic Center. *IAU Circ.*, 6284.
- Paczynski, B. (1979). Evolution of binary X-ray systems. In Baity, W. A. and Peterson, L. E., editors, *X-ray Astronomy*, pages 251–255.
- Pahari, M., Bhattacharyya, S., Yadav, J. S., and Pandey, S. K. (2012). Evidence of two unique variability classes from IGR J17091-3624. *MNRAS*, 422:L87.
- Pahari, M., Neilsen, J., Yadav, J. S., Misra, R., and Uttley, P. (2013a). Comparison of Time/Phase Lags in the Hard State and Plateau State of GRS 1915+105. *ApJ*, 778:136.
- Pahari, M. and Pal, S. (2009). Discovery of one new class in the light curve of GRS 1915+105. *ArXiv e-prints*.
- Pahari, M., Yadav, J. S., and Bhattacharyya, S. (2014). X-Ray Spectral State Evolution in IGR J17091-3624 and Comparison of its Heartbeat Oscillation Properties with those of GRS 1915+105. *ApJ*, 783:141.
- Pahari, M., Yadav, J. S., Rodriguez, J., Misra, R., Bhattacharyya, S., and Pandey, S. K. (2013b). Properties of Unique Hard X-Ray Dips Observed from GRS 1915+105 and IGR J17091-3624 and Their Implications. *ApJ*, 778:46.
- Pandey-Pommier, M., Masetti, N., and Durouchoux, P. (2014). GRO J1744-28: search for radio counterpart with the GMRT. *The Astronomer’s Telegram*, 5904.
- Papitto, A. (2017). The discovery of transitional (and optical) millisecond pulsars. La Gomera Accretion Week 2017.
- Papitto, A., Ferrigno, C., Bozzo, E., Rea, N., Pavan, L., Burderi, L., Burgay, M., Campana, S., di Salvo, T., Falanga, M., Filipović, M. D., Freire, P. C. C., Hessels, J. W. T., Possenti, A., Ransom, S. M., Riggio, A., Romano, P., Sarkissian, J. M., Stairs, I. H., Stella, L., Torres, D. F., Wieringa, M. H., and Wong, G. F. (2013a). Swings between rotation and accretion power in a binary millisecond pulsar. *Nature*, 501:517–520.

- Papitto, A., Hessels, J. W. T., Burgay, M., Ransom, S., Rea, N., Possenti, A., Stairs, I., Ferrigno, C., and Bozz, E. (2013b). The transient low-mass X-ray binary IGR J18245-2452 is again active as a radio pulsar. *The Astronomer's Telegram*, 5069.
- Patruno, A., Haskell, B., and Andersson, N. (2017). The Spin Distribution of Fast-spinning Neutron Stars in Low-mass X-Ray Binaries: Evidence for Two Subpopulations. *ApJ*, 850:106.
- Patruno, A., Maitra, D., Curran, P. A., D'Angelo, C., Fridriksson, J. K., Russell, D. M., Middleton, M., and Wijnands, R. (2016). The Reflares and Outburst Evolution in the Accreting Millisecond Pulsar SAX J1808.4-3658: A Disk Truncated Near Co-Rotation? *ApJ*, 817:100.
- Patruno, A., Watts, A., Klein Wolt, M., Wijnands, R., and van der Klis, M. (2009). 1 Hz Flaring in SAX J1808.4-3658: Flow Instabilities near the Propeller Stage. *ApJ*, 707:1296–1309.
- Patruno, A. and Watts, A. L. (2012). Accreting Millisecond X-Ray Pulsars. *ArXiv e-prints*.
- Pedregosa, F., Varoquaux, G., Gramfort, A., Michel, V., Thirion, B., Grisel, O., Blondel, M., Prettenhofer, P., Weiss, R., Dubourg, V., Vanderplas, J., Passos, A., Cournapeau, D., Brucher, M., Perrot, M., and Duchesnay, E. (2011). Scikit-learn: Machine learning in Python. *Journal of Machine Learning Research*, 12:2825–2830.
- Pence, W. D. (1992). FTOOLS - A New Package of Programs to Manipulate and Process FITS Format Files. In *American Astronomical Society Meeting Abstracts #180*, volume 24 of *Bulletin of the American Astronomical Society*, page 750.
- Poisson, S. (1837).
- Poutanen, J. and Svensson, R. (1996). The Two-Phase Pair Corona Model for Active Galactic Nuclei and X-Ray Binaries: How to Obtain Exact Solutions. *ApJ*, 470:249.
- Pretorius, M. L. (2009). Time-resolved optical observations of five cataclysmic variables detected by INTEGRAL. *MNRAS*, 395:386–393.
- Pringle, J. E. (1981). Accretion discs in astrophysics. *ARA&A*, 19:137–162.
- Psaltis, D. (2008). Probes and Tests of Strong-Field Gravity with Observations in the Electromagnetic Spectrum. *Living Reviews in Relativity*, 11:9.
- Rao, A. and Vadawale, S. V. (2012). Why is IGR J17091-3624 So Faint? Constraints on Distance, Mass, and Spin from "Phase-resolved" Spectroscopy of the "Heartbeat" Oscillations. *ApJ*, 757:L12.
- Rappaport, S., Markert, T., Li, F. K., Clark, G. W., Jernigan, J. G., and McClintock, J. E. (1977). Discovery of a 7.68 second X-ray periodicity in 3U 1626-67. *ApJ*, 217:L29–L33.

- Rea, N., Zelati, F. C., Esposito, P., D’Avanzo, P., de Martino, D., Israel, G. L., Torres, D. F., Campana, S., Belloni, T. M., Papitto, A., Masetti, N., Carrasco, L., Possenti, A., Wieringa, M., Wilhelmi, E. D. O., Li, J., Bozzo, E., Ferrigno, C., Linares, M., Tauris, T. M., Hernanz, M., Ribas, I., Monelli, M., Borghese, A., Baglio, M. C., and Casares, J. (2017). Multiband study of RX J0838-2827 and XMM J083850.4-282759: a new asynchronous magnetic cataclysmic variable and a candidate transitional millisecond pulsar. *MNRAS*, 471:2902–2916.
- Rebusco, P., Moskalik, P., Kluźniak, W., and Abramowicz, M. A. (2012). Period doubling and non-linear resonance in the black hole candidate IGR J17091-3624? *A&A*, 540:L4.
- Reid, M. J., McClintock, J. E., Steiner, J. F., Steeghs, D., Remillard, R. A., Dhawan, V., and Narayan, R. (2014). A Parallax Distance to the Microquasar GRS 1915+105 and a Revised Estimate of its Black Hole Mass. *ApJ*, 796:2.
- Remillard, R. A., McClintock, J. E., Sobczak, G. J., Bailyn, C. D., Orosz, J. A., Morgan, E. H., and Levine, A. M. (1999a). X-Ray Nova XTE J1550-564: Discovery of a Quasi-periodic Oscillation near 185 HZ. *ApJ*, 517:L127–L130.
- Remillard, R. A., Morgan, E. H., McClintock, J. E., Bailyn, C. D., and Orosz, J. A. (1999b). RXTE Observations of 0.1-300 HZ Quasi-periodic Oscillations in the Microquasar GRO J1655-40. *ApJ*, 522:397–412.
- Robitaille, T. and Bressert, E. (2012). APLpy: Astronomical Plotting Library in Python. Astrophysics Source Code Library.
- Rodriguez, J., Corbel, S., Caballero, I., Tomsick, J. A., Tzioumis, T., Paizis, A., Cadolle Bel, M., and Kuulkers, E. (2011a). First simultaneous multi-wavelength observations of the black hole candidate IGR J17091-3624. ATCA, INTEGRAL, Swift, and RXTE views of the 2011 outburst. *A&A*, 533:L4.
- Rodriguez, J., Corbel, S., and Tomsick, J. A. (2003). Spectral Evolution of the Microquasar XTE J1550-564 over Its Entire 2000 Outburst. *ApJ*, 595:1032–1038.
- Rodriguez, J., Corbel, S., Tomsick, J. A., Paizis, A., and Kuulkers, E. (2011b). 0.1 Hz QPOs during RXTE observations of IGR J17091-3624. *The Astronomer’s Telegram*, 3168.
- Rodriguez, J., Hannikainen, D. C., Shaw, S. E., Pooley, G., Corbel, S., Tagger, M., Mirabel, I. F., Belloni, T., Cabanac, C., Cadolle Bel, M., Chenevez, J., Kretschmar, P., Lehto, H. J., Paizis, A., Varnière, P., and Vilhu, O. (2008). 2 Years of INTEGRAL Monitoring of GRS 1915+105. I. Multiwavelength Coverage with INTEGRAL, RXTE, and the Ryle Radio Telescope. *ApJ*, 675:1436–1448.
- Roming, P. W. A., Hunsberger, S. D., Nousek, J. A., Ivanushkina, M., Mason, K. O., and Breeveld, A. A. (2004). The Swift Ultra-Violet/Optical Telescope (UVOT). In Fenimore, E. and Galassi, M., editors, *Gamma-Ray Bursts: 30 Years of Discovery*, volume 727 of *American Institute of Physics Conference Series*, pages 651–654.

- Roy, J., Ray, P. S., Bhattacharyya, B., Stappers, B., Chengalur, J. N., Deneva, J., Camilo, F., Johnson, T. J., Wolff, M., Hessels, J. W. T., Bassa, C. G., Keane, E. F., Ferrara, E. C., Harding, A. K., and Wood, K. S. (2015). Discovery of Psr J1227-4853: A Transition from a Low-mass X-Ray Binary to a Redback Millisecond Pulsar. *ApJ*, 800:L12.
- Russell, T., Degenaar, N., Miller-Jones, J., and Tudor, V. (2017). Radio luminosity upper limits of the transient neutron star low-mass X-ray binary GRO J1744-28. *The Astronomer's Telegram*, 10106.
- Sanna, A., Bahramian, A., Bozzo, E., Heinke, C., Altamirano, D., Wijnands, R., Degenaar, N., Maccarone, T., Riggio, A., Di Salvo, T., Iaria, R., Burgay, M., Possenti, A., Ferrigno, C., Papitto, A., Sivakoff, G., D'Amico, N., and Burderi, L. (2017a). Discovery of 105 Hz coherent pulsations in the ultracompact binary IGR J16597-3704. *ArXiv e-prints*.
- Sanna, A., D'Ai, A., Bozzo, E., Riggio, A., Pintore, F., Burderi, L., Di Salvo, T., and Iaria, R. (2017b). Swift-XRT confirms the renewed X-ray activity of the Bursting Pulsar “GRO J1744-28”. *The Astronomer's Telegram*, 10079.
- Sanna, A., Riggio, A., Burderi, L., Pintore, F., Di Salvo, T., D'Ai, A., Bozzo, E., Esposito, P., Segreto, A., Scarano, F., Iaria, R., and Gambino, A. F. (2017c). Study of the accretion torque during the 2014 outburst of the X-ray pulsar GRO J1744-28. *MNRAS*, 469:2–12.
- Sazonov, S. Y., Sunyaev, R. A., and Lund, N. (1997). Super-Eddington x-ray luminosity of the bursting pulsar GRO J1744-28: WATCH/Granat observations. *Astronomy Letters*, 23:286–292.
- Sądowski, A. (2016). Magnetic flux stabilizing thin accretion discs. *MNRAS*, 462:960–965.
- Scargle, J. D. (1982). Studies in astronomical time series analysis. II - Statistical aspects of spectral analysis of unevenly spaced data. *ApJ*, 263:835–853.
- Scaringi, S., Maccarone, T. J., Koerding, E., Knigge, C., Vaughan, S., Marsh, T. R., Aranzana, E., Dhillon, V., and Barros, S. C. C. (2015). Accretion-induced variability links young stellar objects, white dwarfs, and black holes. *ArXiv e-prints*.
- Schnopper, H. W., Budtz-Joergensen, C. C., Westergaard, N. J., Hornstrup, A., Kamarainen, V. J., Huovelin, J., Vilhu, O., Costa, E., Piro, L., Frontera, F., Manzo, G., Giarrusso, S., Castro-Tirado, A. J., Reglero, V., Svensson, R., Fabian, A. C., Zdziarski, A., Morawski, M., Jahoda, K., Sunyaev, R., and Pavlinsky, M. P. (1996). Joint European x-ray monitor (JEM-X): x-ray monitor for ESA's INTEGRAL mission. In Ramsey, B. D. and Parnell, T. A., editors, *Gamma-Ray and Cosmic-Ray Detectors, Techniques, and Missions*, volume 2806 of *Proc. SPIE*, pages 297–307.
- Shakura, N. I. and Sunyaev, R. A. (1973). Black holes in binary systems. Observational appearance. *A&A*, 24:337–355.

- Spruit, H. C. and Taam, R. E. (1993). An instability associated with a magnetosphere-disk interaction. *ApJ*, 402:593–604.
- Stappers, B. W., Archibald, A. M., Hessels, J. W. T., Bassa, C. G., Bogdanov, S., Janssen, G. H., Kaspi, V. M., Lyne, A. G., Patruno, A., Tendulkar, S., Hill, A. B., and Glanzman, T. (2014). A State Change in the Missing Link Binary Pulsar System PSR J1023+0038. *ApJ*, 790:39.
- Stefanov, I. Z. (2014). Confronting models for the high-frequency QPOs with Lense-Thirring precession. *MNRAS*, 444:2178–2185.
- Steiner, J. F., Narayan, R., McClintock, J. E., and Ebisawa, K. (2009). A Simple Comptonization Model. *PASP*, 121:1279.
- Strader, J., Li, K.-L., Chomiuk, L., Heinke, C. O., Udalski, A., Peacock, M., Shishkovsky, L., and Tremou, E. (2016). A New γ -Ray Loud, Eclipsing Low-mass X-Ray Binary. *ApJ*, 831:89.
- Strohmayer, T. and Bildsten, L. (2006). *New views of thermonuclear bursts*, pages 113–156.
- Strohmayer, T. E., Jahoda, K., Giles, A. B., and Lee, U. (1997). Millisecond Pulsations from a Low-Mass X-Ray Binary in the Galactic Center Region. *ApJ*, 486:355–362.
- Strüder, L., Briel, U., Dennerl, K., Hartmann, R., Kendziorra, E., Meidinger, N., Pfeffermann, E., Reppin, C., Aschenbach, B., Bornemann, W., Bräuninger, H., Burkert, W., Elender, M., Freyberg, M., Haberl, F., Hartner, G., Heuschmann, F., Hippmann, H., Kastelic, E., Kemmer, S., Kettenring, G., Kink, W., Krause, N., Müller, S., Oppitz, A., Pietsch, W., Popp, M., Predehl, P., Read, A., Stephan, K. H., Stötter, D., Trümper, J., Holl, P., Kemmer, J., Soltau, H., Stötter, R., Weber, U., Weichert, U., von Zanthier, C., Carathanassis, D., Lutz, G., Richter, R. H., Solc, P., Böttcher, H., Kuster, M., Staubert, R., Abbey, A., Holland, A., Turner, M., Balasini, M., Bignami, G. F., La Palombara, N., Villa, G., Buttler, W., Gianini, F., Lainé, R., Lumb, D., and Dhez, P. (2001). The European Photon Imaging Camera on XMM-Newton: The pn-CCD camera. *A&A*, 365:L18–L26.
- Sturner, S. J. and Dermer, C. D. (1996). On the Nature of the Bursting X-Ray Pulsar GRO J1744-28. *ApJ*, 465:L31.
- Svensson, R. and Zdziarski, A. A. (1994). Black hole accretion disks with coronae. *ApJ*, 436:599–606.
- Swank, J. H. (1996). Compact Star Time Scales. In *American Astronomical Society Meeting Abstracts*, volume 28 of *Bulletin of the American Astronomical Society*, page 1342.
- Szkody, P., Fraser, O., Silvestri, N., Henden, A., Anderson, S. F., Frith, J., Lawton, B., Owens, E., Raymond, S., Schmidt, G., Wolfe, M., Bochanski, J., Covey, K., Harris, H., Hawley, S., Knapp, G. R., Margon, B., Voges, W., Walkowicz, L., Brinkmann, J., and

- Lamb, D. Q. (2003). Cataclysmic Variables from the Sloan Digital Sky Survey. II. The Second Year. *AJ*, 126:1499–1514.
- Taam, R. E. and Lin, D. N. C. (1984). The evolution of the inner regions of viscous accretion disks surrounding neutron stars. *ApJ*, 287:761–768.
- Tagger, M., Varnière, P., Rodriguez, J., and Pellat, R. (2004). Magnetic Floods: A Scenario for the Variability of the Microquasar GRS 1915+105. *ApJ*, 607:410–419.
- Takahashi, T., Abe, K., Endo, M., Endo, Y., Ezoe, Y., Fukazawa, Y., Hamaya, M., Hirakuri, S., Hong, S., Horii, M., Inoue, H., Isobe, N., Itoh, T., Iyomoto, N., Kamae, T., Kasama, D., Kataoka, J., Kato, H., Kawaharada, M., Kawano, N., Kawashima, K., Kawasoe, S., Kishishita, T., Kitaguchi, T., Kobayashi, Y., Kokubun, M., Kotoku, J., Kouda, M., Kubota, A., Kuroda, Y., Madejski, G., Makishima, K., Masukawa, K., Matsumoto, Y., Mitani, T., Miyawaki, R., Mizuno, T., Mori, K., Mori, M., Murashima, M., Murakami, T., Nakazawa, K., Niko, H., Nomachi, M., Okada, Y., Ohno, M., Oonuki, K., Ota, N., Ozawa, H., Sato, G., Shinoda, S., Sugiho, M., Suzuki, M., Taguchi, K., Takahashi, H., Takahashi, I., Takeda, S., Tamura, K.-I., Tamura, T., Tanaka, T., Tanihata, C., Tashiro, M., Terada, Y., Tominaga, S., Uchiyama, Y., Watanabe, S., Yamaoka, K., Yanagida, T., and Yonetoku, D. (2007). Hard X-Ray Detector (HXD) on Board Suzaku. *PASJ*, 59:35–51.
- Tomsick, J. A., Kalemci, E., Corbel, S., and Kaaret, P. (2003). X-Ray Flares and Oscillations from the Black Hole Candidate X-Ray Transient XTE J1650-500 at Low Luminosity. *ApJ*, 592:1100–1109.
- Turner, M. J. L., Abbey, A., Arnaud, M., Balasini, M., Barbera, M., Belsole, E., Bennie, P. J., Bernard, J. P., Bignami, G. F., Boer, M., Briel, U., Butler, I., Cara, C., Chabaud, C., Cole, R., Collura, A., Conte, M., Cros, A., Denby, M., Dhez, P., Di Cocco, G., Dowson, J., Ferrando, P., Ghizzardi, S., Gianotti, F., Goodall, C. V., Gretton, L., Griffiths, R. G., Hainaut, O., Hochedez, J. F., Holland, A. D., Jourdain, E., Kendziorra, E., Lagostina, A., Laine, R., La Palombara, N., Lortholary, M., Lumb, D., Marty, P., Molendi, S., Pigot, C., Poindron, E., Pounds, K. A., Reeves, J. N., Reppin, C., Rothenflug, R., Salvatat, P., Sauvageot, J. L., Schmitt, D., Sembay, S., Short, A. D. T., Spragg, J., Stephen, J., Strüder, L., Tiengo, A., Trifoglio, M., Trümper, J., Vercellone, S., Vigroux, L., Villa, G., Ward, M. J., Whitehead, S., and Zonca, E. (2001). The European Photon Imaging Camera on XMM-Newton: The MOS cameras : The MOS cameras. *A&A*, 365:L27–L35.
- Ubertini, P., Lebrun, F., Di Cocco, G., Bazzano, A., Bird, A. J., Broenstad, K., Goldwurm, A., La Rosa, G., Labanti, C., Laurent, P., Mirabel, I. F., Quadrini, E. M., Ramsey, B., Reglero, V., Sabau, L., Sacco, B., Staubert, R., Vigroux, L., Weisskopf, M. C., and Zdziarski, A. A. (2003). IBIS: The Imager on-board INTEGRAL. *A&A*, 411:L131–L139.
- Uchiyama, Y., Maeda, Y., Ebara, M., Fujimoto, R., Ishisaki, Y., Ishida, M., Iizuka, R., Ushio, M., Inoue, H., Okada, S., Mori, H., and Ozaki, M. (2008). Restoring the Suzaku Source Position Accuracy and Point-Spread Function. *PASJ*, 60:S35–S42.

- Ueda, Y., Ishioka, R., Sekiguchi, K., Ribo, M., Rodriguez, J., Chaty, S., Greiner, J., Sala, G., Fuchs, Y., Goldoni, P., Covino, S., Pooley, G. G., Edwards, P., Tzioumis, A., Lehto, H., Gerard, E., Colom, P., Martin, J., Trushkin, S. A., Castro-Tirado, A. J., Hannikainen, D., Sudo, H., Honma, M., Iwamuro, F., Kubota, K., Yamaoka, K., Done, C., Naik, S., Fukazawa, Y., Angelini, L., Awaki, H., Ebisawa, K., Iwasawa, K., Kawai, N., Kinugasa, K., Kokubun, M., Kotani, T., Kubota, A., Murakami, T., Namiki, M., Takahashi, H., Yaqoob, T., Yonetoku, D., and Yoshida, A. (2006). The 2005 October Multiwavelength Campaign of GRS 1915+105. In *VI Microquasar Workshop: Microquasars and Beyond*, page 23.1.
- van den Heuvel, E. P. J. (1993). Formation and evolution of pulsars. In Phillips, J. A., Thorsett, S. E., and Kulkarni, S. R., editors, *Planets Around Pulsars*, volume 36 of *Astronomical Society of the Pacific Conference Series*, pages 123–147.
- van der Klis, M. (1989). Quasi-periodic oscillations and noise in low-mass X-ray binaries. *ARA&A*, 27:517–553.
- van der Klis, M. (1997). Kilohertz Quasi-Periodic Oscillations in Low-Mass X-Ray Binaries. In Maoz, D., Sternberg, A., and Leibowitz, E. M., editors, *Astronomical Time Series*, volume 218 of *Astrophysics and Space Science Library*, page 121.
- Van der Klis, M. (2004). A review of rapid X-ray variability in X-ray binaries. *ArXiv Astrophysics e-prints*.
- Vaughan, S., Edelson, R., Warwick, R. S., and Uttley, P. (2003). On characterizing the variability properties of X-ray light curves from active galaxies. *MNRAS*, 345:1271–1284.
- Vedrenne, G., Roques, J.-P., Schönfelder, V., Mandrou, P., Lichti, G. G., von Kienlin, A., Cordier, B., Schanne, S., Knödlseider, J., Skinner, G., Jean, P., Sanchez, F., Caraveo, P., Teegarden, B., von Ballmoos, P., Bouchet, L., Paul, P., Matteson, J., Boggs, S., Wunderer, C., Leleux, P., Weidenspointner, G., Durouchoux, P., Diehl, R., Strong, A., Cassé, M., Clair, M. A., and André, Y. (2003). SPI: The spectrometer aboard INTEGRAL. *A&A*, 411:L63–L70.
- Vignarca, F., Migliari, S., Belloni, T., Psaltis, D., and van der Klis, M. (2003). Tracing the power-law component in the energy spectrum of black hole candidates as a function of the QPO frequency. *A&A*, 397:729–738.
- Vilhu, O. (1999). Super-Eddington Accretion in GRS 1915+105. In Poutanen, J. and Svensson, R., editors, *High Energy Processes in Accreting Black Holes*, volume 161 of *Astronomical Society of the Pacific Conference Series*, page 82.
- von Mises, R. (1964). *Mathematical Theory of Probability and Statistics*.
- Walker, M. A. (1992). Radiation Dynamics in X-Ray Binaries. II. Type 2 Bursts. *ApJ*, 385:651.

- Walter, R., Rohlfs, R., Meharga, M. T., Binko, P., Morisset, N., Beck, M., Produit, N., Pavan, L., Savchenko, V., Ferrigno, C., Frankowski, A., and Bordas, P. (2010). Integral in Heavens. In *Eighth Integral Workshop. The Restless Gamma-ray Universe (INTEGRAL 2010)*, page 162.
- Weisskopf, M. C. (1999). The Chandra X-Ray Observatory (CXO): An Overview. *ArXiv Astrophysics e-prints*.
- White, N. E. and Zhang, W. (1997). Millisecond X-Ray Pulsars in Low-mass X-Ray Binaries. *ApJ*, 490:L87–L90.
- Wijnands, R., Méndez, M., Markwardt, C., van der Klis, M., Chakrabarty, D., and Morgan, E. (2001). The Erratic Luminosity Behavior of SAX J1808.4-3658 during Its 2000 Outburst. *ApJ*, 560:892–896.
- Wijnands, R. and van der Klis, M. (1998). A millisecond pulsar in an X-ray binary system. *Nature*, 394:344–346.
- Wijnands, R. and Wang, Q. D. (2002). A Chandra Observation of GRO J1744-28: The Bursting Pulsar in Quiescence. *ApJ*, 568:L93–L96.
- Wijnands, R., Yang, Y. J., and Altamirano, D. (2012). The enigmatic black hole candidate and X-ray transient IGR J17091-3624 in its quiescent state as seen with XMM-Newton. *MNRAS*, 422:91–95.
- Wilms, J., Allen, A., and McCray, R. (2000). On the Absorption of X-Rays in the Interstellar Medium. *ApJ*, 542:914–924.
- Winkler, C., Courvoisier, T. J.-L., Di Cocco, G., Gehrels, N., Giménez, A., Grebenev, S., Hermsen, W., Mas-Hesse, J. M., Lebrun, F., Lund, N., Palumbo, G. G. C., Paul, J., Roques, J.-P., Schnopper, H., Schönfelder, V., Sunyaev, R., Teegarden, B., Ubertini, P., Vedrenne, G., and Dean, A. J. (2003). The INTEGRAL mission. *A&A*, 411:L1–L6.
- Woods, P. M., Kouveliotou, C., van Paradijs, J., Briggs, M. S., Wilson, C. A., Deal, K., Harmon, B. A., Fishman, G. J., Lewin, W. H. G., and Kommers, J. (1999). Properties of the Second Outburst of the Bursting Pulsar (GRO J1744-28) as Observed with BATSE. *ApJ*, 517:431–435.
- Woods, P. M., Kouveliotou, C., van Paradijs, J., Koshut, T. M., Finger, M. H., Briggs, M. S., Fishman, G. J., and Lewin, W. H. G. (2000). Detailed Analysis of the Pulsations during and after Bursts from the Bursting Pulsar (GRO J1744-28). *ApJ*, 540:1062–1068.
- Xue, L., Sądowski, A., Abramowicz, M. A., and Lu, J.-F. (2011). Studies of Thermally Unstable Accretion Disks Around Black Holes with Adaptive Pseudospectral Domain Decomposition Method. II. Limit-cycle Behavior in Accretion Disks around Kerr Black Holes. *ApJS*, 195:7.

- Yadav, J. S., Agrawal, P. C., Paul, B., Rao, A. R., Seetha, S., and Kasturirangan, K. (2000). Different Types of X-ray Bursts During High State of the Superluminal Source GRS 1915+105. *Advances in Space Research*, 25:441–444.
- Younes, G., Kouveliotou, C., Grefenstette, B. W., Tomsick, J. A., Tennant, A., Finger, M. H., Fürst, F., Pottschmidt, K., Bhalerao, V., Boggs, S. E., Boirin, L., Chakrabarty, D., Christensen, F. E., Craig, W. W., Degenaar, N., Fabian, A. C., Gandhi, P., Göğüş, E., Hailey, C. J., Harrison, F. A., Kennea, J. A., Miller, J. M., Stern, D., and Zhang, W. W. (2015). Simultaneous NuSTAR/Chandra Observations of the Bursting Pulsar GRO J1744-28 during Its Third Reactivation. *ApJ*, 804:43.
- Zdziarski, A. A., Johnson, W. N., and Magdziarz, P. (1996). Broad-band γ -ray and X-ray spectra of NGC 4151 and their implications for physical processes and geometry. *MNRAS*, 283:193–206.
- Zhang, Z., Qu, J. L., Gao, H. Q., Zhang, S., Bu, Q. C., Ge, M. Y., Chen, L., and Li, Z. B. (2014). The variability classes in IGR J17091-3624 during the 2011 outburst. *A&A*, 569:A33.
- Zheng, S.-M., Yuan, F., Gu, W.-M., and Lu, J.-F. (2011). Revisiting the Thermal Stability of Radiation-dominated Thin Disks. *ApJ*, 732:52.
- Zimmerman, E. R., Narayan, R., McClintock, J. E., and Miller, J. M. (2005). Multitemperature Blackbody Spectra of Thin Accretion Disks with and without a Zero-Torque Inner Boundary Condition. *ApJ*, 618:832–844.
- Zoghbi, A., Miller, J. M., King, A. L., Miller, M. C., Proga, D., Kallman, T., Fabian, A. C., Harrison, F. A., Kaastra, J., Raymond, J., Reynolds, C. S., Boggs, S. E., Christensen, F. E., Craig, W., Hailey, C. J., Stern, D., and Zhang, W. W. (2016). Disk-Wind Connection during the Heartbeats of GRS 1915+105. *ApJ*, 833:165.
- Życki, P. T., Done, C., and Smith, D. A. (1999). The 1989 May outburst of the soft X-ray transient GS 2023+338 (V404 Cyg). *MNRAS*, 309:561–575.

Appendix A

Model-Independent Classification of each Observation of IGR J17091-3624

Observation IDs, and orbit IDs, for every observation and observation segment that was used in our analysis are presented in Table A.1. Note that not all of every observation was used; in many cases, large spikes caused by PCA PCUs switching off or on rendered ~ 100 s unusable. As these often occurred very close to the beginning or end of an observation segment, small sections of data before or after these spikes was also sometimes discarded. Every observation segment is presented along with the variability class assigned to it by this study.

Table A.1: Here is listed the Observation IDs for every *RXTE* observation that was used in this analysis, along with the variability class which has been assigned to it. *Orb.* is the orbit ID (starting at 0) of each observation segment, *Exp.* is the exposure time in seconds and **X** is the prefix 96420-01. This table is continued overleaf in Table A.2.

MJD	OBSID	<i>Orb.</i>	Class	<i>Exp.</i>	MJD	OBSID	<i>Orb.</i>	Class	<i>Exp.</i>	MJD	OBSID
55622	X-01-00	0	I	1840	55676	X-09-06	0	VI	3540	55741	X-18-05
55622	X-01-000	0	I	3480	55677	X-09-01	0	V	1676	55743	X-19-00
55622	X-01-000	1	I	1656	55678	X-09-04	0	V	2090	55744	X-19-01
55622	X-01-000	2	I	3384	55679	X-09-02	0	V	2306	55745	X-19-02
55622	X-01-000	3	I	3400	55680	X-10-02	0	V	952	55747	X-19-03
55622	X-01-000	4	I	3384	55681	X-10-00	0	V	3725	55748	X-19-04
55623	X-01-01	0	I	1240	55682	X-10-03	0	V	1157	55749	X-19-05
55623	X-01-01	1	I	752	55684	X-10-01	0	III	1504	55751	X-20-05
55623	X-01-01	2	I	992	55686	X-10-04	0	III	1127	55752	X-20-01
55623	X-01-01	3	I	1184	55686	X-10-05	0	II	2179	55753	X-20-02
55623	X-01-01	4	I	1056	55687	X-11-00	0	II	3537	55754	X-20-03
55623	X-01-010	0	I	2080	55688	X-11-01	0	II	1153	55756	X-20-04
55623	X-01-010	1	I	1832	55690	X-11-02	0	II	1408	55757	X-21-00
55623	X-01-010	2	I	1648	55691	X-11-03	0	II	886	55758	X-21-01
55623	X-01-010	4	I	1424	55692	X-11-04	0	II	3566	55759	X-21-02
55623	X-01-010	5	I	400	55693	X-11-05	0	II	1817	55761	X-21-04
55623	X-01-02	0	I	3056	55694	X-12-00	0	II	2761	55762	X-21-05
55623	X-01-02	1	I	2792	55695	X-12-01	0	II	1374	55763	X-21-06
55623	X-01-02	2	I	2432	55695	X-12-02	0	II	2041	55764	X-22-00
55623	X-01-020	0	I	3456	55696	X-12-03	0	II	1456	55765	X-22-01
55623	X-01-020	1	I	3464	55698	X-12-04	0	II	1916	55766	X-22-02
55623	X-01-020	2	I	3512	55698	X-12-05	0	II	3139	55767	X-22-03
55623	X-01-020	3	I	3520	55700	X-12-06	0	II	1189	55768	X-22-04
55623	X-01-020	4	I	3512	55701	X-13-00	0	II	1214	55769	X-22-05
55623	X-01-020	5	I	464	55702	X-13-01	0	II	980	55770	X-22-06
55624	X-02-00	0	I	1758	55704	X-13-02	0	II	732	55771	X-23-00
55626	X-02-01	0	I	1380	55705	X-13-03	0	III	1217	55772	X-23-01
55628	X-02-02	0	I	3305	55706	X-13-04	0	III	1161	55773	X-23-02
55630	X-02-03	0	I	1876	55707	X-13-05	0	IV	2763	55774	X-23-03
55632	X-03-00	0	I	1712	55708	X-14-00	0	IV	1188	55775	X-23-04
55634	X-03-01	0	III	3590	55709	X-14-01	0	IV	3342	55776	X-23-05
55639	X-04-00	0	IV	3099	55710	X-14-02	0	IV	1094	55777	X-23-06
55642	X-04-02	0	IV	2972	55712	X-14-03	0	IV	1404	55777	X-23-06
55643	X-04-01	0	III	1190	55713	X-14-04	0	V	871	55778	X-24-00
55644	X-04-03	0	III	2903	55714	X-14-05	0	V	1311	55779	X-24-01
55645	X-05-02	0	I	3578	55715	X-15-00	0	IV	1241	55779	X-24-02
55647	X-05-00	0	IV	2872	55716	X-15-01	0	IV	1262	55782	X-24-03
55647	X-05-000	0	IV	3472	55717	X-15-02	0	III	1557	55782	X-24-04
55647	X-05-000	1	IV	3520	55718	X-15-03	0	III	1334	55784	X-24-05
55647	X-05-000	2	IV	3512	55720	X-15-04	0	IV	1486	55784	X-24-06
55647	X-05-000	3	IV	3520	55721	X-15-05	0	IV	1500	55785	X-25-00
55647	X-05-000	4	IV	3512	55722	X-16-00	0	IV	900	55786	X-25-01
55647	X-05-000	5	IV	648	55723	X-16-01	0	III	1004	55787	X-25-02
55649	X-05-03	0	IV	2409	55724	X-16-02	0	II	1923	55788	X-25-03
55650	X-05-01	0	IV	1473	55725	X-16-03	0	II	1919	55789	X-25-04
55651	X-05-04	0	IV	2954	55726	X-16-04	0	III	1935	55790	X-25-05
55653	X-06-00	0	IV	2723	55727	X-16-05	0	II	730	55791	X-25-06
55654	X-06-01	0	IV	3388	55728	X-16-06	0	II	1953	55792	X-26-00
55656	X-06-02	0	IV	2908	55729	X-17-00	0	II	2735	55794	X-26-01
55657	X-06-03	0	V	1842	55730	X-17-01	0	II	3556	55795	X-26-02
55661	X-07-00	0	V	1754	55731	X-17-02	0	II	3605	55796	X-26-03
55662	X-07-01	0	V	2355	55732	X-17-03	0	II	1647	55798	X-26-04

Table A.2: A continuation of Table A.1. *Orb.* is the orbit ID (starting at 0) of each observation segment, *Exp.* is the exposure time in seconds and **X** is the prefix 96420-01.

MJD	OBSID	<i>Orb.</i>	Class	<i>Exp.</i>	MJD	OBSID	<i>Orb.</i>	Class	<i>Exp.</i>	MJD	OBSID	<i>Orb.</i>	Class
55810	X-28-02	0	VI	1251	55836	X-32-02	0	IX	1591	55857	X-35-01	0	IX
55811	X-28-03	0	VI	2000	55837	X-32-03	0	IX	2155	55859	X-35-02	0	IX
55813	X-29-00	0	VIII	1309	55838	X-32-04	0	IX	2641	55859	X-35-02	1	IX
55819	X-29-04	0	VIII	1686	55838	X-32-05	0	IX	2077	55860	X-35-03	0	IX
55820	X-30-00	0	VI	1488	55840	X-32-06	0	IX	3392	55861	X-35-04	0	IX
55821	X-30-01	0	VI	1503	55840	X-32-06	1	IX	3512	55862	X-36-00	0	IX
55822	X-30-02	0	VI	1417	55840	X-32-06	2	IX	3934	55863	X-36-01	0	IX
55823	X-30-03	0	VI	1290	55840	X-32-06	3	IX	3880	55865	X-36-03	0	IX
55824	X-30-04	0	VI	1489	55840	X-32-06	4	IX	1896	55866	X-36-04	0	IX
55825	X-30-05	0	VI	2581	55841	X-33-00	0	IX	1188	55867	X-36-05	0	IX
55826	X-30-06	0	VI	2747	55842	X-33-01	0	IX	855	55868	X-36-06	0	IX
55827	X-31-00	0	VI	1559	55843	X-33-02	0	IX	1156	55871	X-37-00	0	IX
55828	X-31-01	0	VI	2954	55845	X-33-04	0	IX	1713	55871	X-37-02	0	IX
55829	X-31-02	0	IX	3005	55846	X-33-05	0	IX	934	55872	X-37-03	0	IX
55830	X-31-03	0	IX	1472	55847	X-33-06	0	IX	717	55873	X-37-04	0	IX
55830	X-31-03	1	IX	288	55848	X-34-00	0	IX	1159	55874	X-37-05G	0	IX
55831	X-31-04	0	IX	1586	55849	X-34-01	0	IX	973	55875	X-37-06	0	IX
55832	X-31-05	0	VI	3812	55851	X-34-02	0	IX	2261	55876	X-38-00	0	IX
55833	X-31-06	0	IX	3675	55852	X-34-03	0	IX	1092	55877	X-38-01	0	IX
55834	X-32-00	0	IX	1217	55853	X-34-04	0	IX	741	55878	X-38-02	0	IX
55835	X-32-01	0	IX	1445	55856	X-35-00	0	IX	797	55879	X-38-03	0	IX